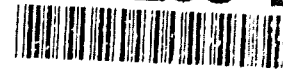


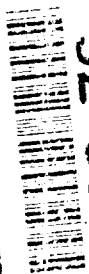
AD-A258 215



12

NONLINEAR ANALYSIS OF CAVITATING PROPELLERS
IN NONUNIFORM FLOW

Neal E. Fine



92-30511

OTIC
ELECTE
DEC 01 1992

DISTRIBUTION STATEMENT

Approved for public release
Distribution Unlimited

Report 92-5

Massachusetts Institute of Technology
Department of Ocean Engineering
Cambridge, MA 02139

MASSACHUSETTS INSTITUTE OF TECHNOLOGY
DEPARTMENT OF OCEAN ENGINEERING
CAMBRIDGE, MA 02139

Report No. 92-5

Nonlinear Analysis of Cavitating Propellers in Nonuniform Flow

Neal E. Fine

October 16, 1992

The preparation of this document was carried out under the
Applied Hydromechanics Research Program
Administered by the Office of Naval Research
ONR Contract No. N00014-90-J-1086
MIT OSP 72930

DEPT. OF NAVAL RESEARCH

Accession For	
NTIS	<input checked="checked" type="checkbox"/>
CRA&I	<input checked="checked" type="checkbox"/>
DTIC	<input type="checkbox"/>
TAB	<input type="checkbox"/>
Unannounced	<input type="checkbox"/>
Justification	
By	
Distribution /	
Availability Codes	
Dist	Avail and/or Special
A-1	

Nonlinear Analysis of Cavitating Propellers in Nonuniform Flow

by

Neal E. Fine

B.S., University of Rochester (1986)

S.M., Massachusetts Institute of Technology (1988)

Submitted to the Department of Ocean Engineering
in partial fulfillment of the requirements for the degree of

Doctor of Philosophy

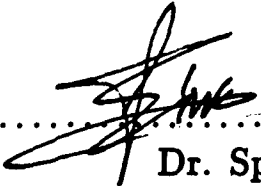
at the

MASSACHUSETTS INSTITUTE OF TECHNOLOGY

October 1992

© Massachusetts Institute of Technology 1992. All rights reserved.

Author *Neal E. Fine*
Department of Ocean Engineering

Certified by 
Dr. Spyros A. Kinnas
Lecturer and Principal Research Engineer
Thesis Supervisor

Accepted by *A. Douglas Carmichael*
Professor A. Douglas Carmichael
Chairman, Departmental Committee on Graduate Students

REPORT DOCUMENTATION PAGE		READ INSTRUCTIONS BEFORE COMPLETING FORM
1. REPORT NUMBER 92-5	2. GOVT ACCESSION NO.	3. RECIPIENT'S CATALOG NUMBER
4. TITLE (and Subtitle) Nonlinear Analysis of Cavitating Propellers in Nonuniform Flow		5. TYPE OF REPORT & PERIOD COVERED Technical Report
7. AUTHOR(s) Neal E. Fine		6. PERFORMING ORG. REPORT NUMBER
9. PERFORMING ORGANIZATION NAME AND ADDRESS Department of Ocean Engineering Massachusetts Institute of Technology 77 Mass. Ave., Cambridge, MA 02139		8. CONTRACT OR GRANT NUMBER(s) N00014-90-J-1086
11. CONTROLLING OFFICE NAME AND ADDRESS Office of Naval Research 800 North Quincy St. Arlington, VA 22217-5660		10. PROGRAM ELEMENT, PROJECT, TASK AREA & WORK UNIT NUMBERS
14. MONITORING AGENCY NAME & ADDRESS (if different from Controlling Office)		12. REPORT DATE October 16, 1992
		13. NUMBER OF PAGES
		15. SECURITY CLASS. (of this report) Unclassified
		15a. DECLASSIFICATION/DOWNGRADING SCHEDULE
16. DISTRIBUTION STATEMENT (of this Report) Approved for public release; distribution unlimited		
17. DISTRIBUTION STATEMENT (of the abstract entered in Block 20, if different from Report)		
18. SUPPLEMENTARY NOTES		
19. KEY WORDS (Continue on reverse side if necessary and identify by block number) Cavitation Unsteady Cavitation Hydrofoils Propellers		
20. ABSTRACT (Continue on reverse side if necessary and identify by block number) The work presented in this thesis represents the latest in an on-going effort within the propeller hydrodynamics community to obtain rational design stage estimation of dynamically varying blade loads and shaft/bearing forces for cavitating propellers. To this end, the unsteady cavitating flow about a marine propeller is treated in nonlinear theory by employing a low order potential based boundary element method. The steady state oscillatory solution is obtained by incremental stepping		

in the time domain. The three dimensional, nonlinear and time dependent boundary conditions are satisfied on an approximate boundary consisting of the propeller surface beneath the cavity and the portion of the blade wake surface overlapped by the cavity. This solution represents the first iteration of a completely nonlinear solution in which the exact boundary conditions are satisfied on the exact flow boundary, including the cavity free-surface. It is then shown that the convergence of such an iterative solution for two-dimensional flows is remarkably fast and that the accuracy of the first iteration solution is sufficient for a wide range of operating conditions. Emphasis is placed on developing an efficient and robust iterative scheme to predict general cavity planforms. The numerical method is shown to be convergent and consistent with fully nonlinear results. Computed results are compared to those from linear theory, linear theory with leading edge corrections, and to published experimental measurements and observations.

Nonlinear Analysis of Cavitating Propellers in Nonuniform Flow

by

Neal E. Fine

Submitted to the Department of Ocean Engineering
on October 16, in partial fulfillment of the
requirements for the degree of
Doctor of Philosophy

Abstract

The work presented in this thesis represents the latest in an on-going effort within the propeller hydrodynamics community to obtain rational design stage estimation of dynamically varying blade loads and shaft/bearing forces for cavitating propellers. To this end, the unsteady cavitating flow about a marine propeller is treated in nonlinear theory by employing a low order potential based boundary element method. The steady state oscillatory solution is obtained by incremental stepping in the time domain. The three dimensional, nonlinear and time dependent boundary conditions are satisfied on an approximate boundary consisting of the propeller surface beneath the cavity and the portion of the blade wake surface overlapped by the cavity. This solution represents the first iteration of a completely nonlinear solution in which the exact boundary conditions are satisfied on the exact flow boundary, including the cavity free-surface. It is then shown that the convergence of such an iterative solution for two-dimensional flows is remarkably fast and that the accuracy of the first iteration solution is sufficient for a wide range of operating conditions. Emphasis is placed on developing an efficient and robust iterative scheme to predict general cavity planforms. The numerical method is shown to be convergent and consistent with fully nonlinear results. Computed results are compared to those from linear theory, linear theory with leading edge corrections, and to published experimental measurements and observations.

Thesis Supervisor: Dr. Spyros A. Kinnas
Title: Lecturer and Principal Research Engineer

ACKNOWLEDGEMENTS

Many people deserve acknowledgement for their support, advice or friendship — all of which I found in plentiful supply — during the course of my studies at MIT. First and foremost is my advisor, Dr. Spyros A. Kinnas; he was always very generous with his time and energy and I often took advantage of that generosity! The same applies to my academic advisor, Professor J.E. Kerwin, whose unselfish and unpretentious style I greatly admire. I will always be grateful to Professor Kerwin and Dr. Kinnas for getting me started in this business and for sticking with me through tough times. Dr. James Uhlman deserves special recognition for having to travel across the state border for each committee meeting. In addition, his technical expertise in fluid dynamics and unselfish donation of his time (which is in short supply) contributed a great deal to this work. I am grateful to Professor Mark Drela for taking part in this study and offering his expert advice.

I never had to work alone at MIT. The cast of “propeller nuts” whose support, advice or friendship I wish to acknowledge include: Mr. Michael Hughes, Dr. Ching-Yeh Hsin, Dr. David Keenan, Dr. William Coney, Dr. Charles Mazel, Mr. Songwoo Pyo, Mr. Randall Villeneuve, Mr. S. Dean Lewis, Mr. Lawrence Leibman, and Mr. Robert Stairs. These are only a few of the people who have passed through my life at MIT. I will remember them all fondly.

I propose that all spouses of MIT graduate students — excluding those that are students themselves — be awarded honorary degrees for having to share in the sacrifice which is required to obtain a doctorate. My wife should be the first recipient. While a “year-and-a-half to two” years stretched to “two-and-a-half to three”, Jennifer stuck with me through all the blood, sweat and tears. She may not believe it, but without her I never would have made it this far. I dedicate this thesis to her.

This work was supported by the Applied Hydromechanics Research Program administered by the Office of Naval Research (Contract No. N00014-90-J-1086). Special thanks to Mr. Randall Villeneuve for making Figures 4-8, 4-9 and 4-14.

PREFACE

Cavitation is the process in which vapor filled cavities form in a moving liquid in response to dynamic-pressure reduction, as often occurs on the back side of propeller blades. Its importance to naval hydrodynamics is paramount, as is perhaps best illustrated by the history of the term "cavitation." The term was coined (by Froude) during an investigation of the failure of a British destroyer to reach its design speed, wherein the investigators postulated that the thrust was limited by cavities which enveloped the ship's propellers [41, 62]. The rest, as they say, is history.

During the past century, the study of cavitation has occupied both engineers and mathematicians, who tend to see the world from somewhat different perspectives. Witness, for example, the views of two men who have made significant contributions to the field: Professors R.T. Knapp of California Institute of Technology and G. Birkhoff of Harvard. Professor Knapp (a civil engineer), in the preface to his book Cavitation [41], referred to it as a "most unpleasant" phenomenon, with harmful effects which "handicap many phases of science and engineering." While he might agree with this, Professor Birkhoff (a mathematician) looked more favorably on the subject, as is evident in the preface to *his* book Jets, Wakes, and Cavities [4] where he wrote of his intent to report systematically on nearly a century of "ingenious research in a fascinating and complex field."

So, is cavitation "unpleasant", or is it "fascinating?" Personally, I believe it is both, and I am glad to have it that way. On the one hand, it is unpleasant enough to warrant a scientific investigation, while on the other hand many of us find enough fascination in the topic to invest our energy, enthusiasm, and wit in obtaining engineering solutions. This happy marriage of the practical and the theoretical is true of many engineering problems in naval hydrodynamics, a fact which continues to attract mathematically inclined engineers to the field.

Contents

1	Introduction	23
1.1	Objectives	26
1.2	Fundamental Assumptions	27
1.3	Previous Research	28
1.3.1	2-D Free Streamline Flows	28
1.3.2	2-D Linear Theory	29
1.3.3	3-D Cavity Flows	29
1.3.4	Nonlinear Solutions	30
1.3.5	Present Method	31
2	Mathematical Formulation	35
2.1	Definition of the Problem	35
2.2	Green's Formula	38
2.3	The Dynamic Boundary Condition	44
2.4	The Kinematic Boundary Condition	48
2.5	The Kutta Condition	53
3	Discrete Formulation	55
3.1	Solution Methodology	55
3.2	Discretized Green's Formula	57
3.3	Discretized Boundary Conditions	61
4	Solution	68
4.1	Solution for Given Cavity Planform	68

4.1.1	Details of the Split-Panel Method	69
4.1.2	System of Equations	77
4.1.3	Cavity Height Computation	79
4.2	Finding the Cavity Planform	79
4.2.1	Multiplicity of Solutions	82
4.2.2	Sensitivity of the Solution to δ Tolerance	86
4.2.3	Nature of the Tip Solution	86
4.2.4	Convergence of the Crossflow Term	90
4.2.5	Nonlinear Effect of Foil Thickness	91
4.3	The Effect of ϕ_0 on the Solution	94
4.4	Time-Marching Scheme	94
4.5	Treatment of the Unsteady Terms	96
5	Numerical Validation	100
5.1	Convergence	100
5.2	Consistency	109
5.2.1	Fully Wetted Consistency Test	109
5.2.2	Pressure Validation	109
5.2.3	Comparison to PUF-3A	111
5.2.4	Effect of the Hub	116
5.2.5	Comparison to Experimental Results	118
6	Conclusions and Recommendations	123
6.1	Conclusions	123
6.2	Recommendations for Future Research	125
A	Green's Formula on the Wake Surface	136
B	Performance of the Method for 2-D Flows	139
B.1	Fixed-length Solution	140
B.1.1	Partial Cavitation	140
B.1.2	Supercavitation	143

B.2	Fixed- σ Solution	145
B.2.1	Partial Cavitation	145
B.2.2	Supercavitation	151
B.2.3	Partial Cavitation Fully Nonlinear Solution	151
B.3	Effect of the detachment point	155
B.4	Conclusions from 2-D Survey	156
C	Termination Models	157
C.1	Partial Cavitation	158
C.1.1	Cavity Height Law	158
C.1.2	Pressure Law	159
C.2	Supercavitation	161
C.2.1	Curved End-Plate Model	161
C.2.2	Pressure Law	167

List of Figures

1-1	A sketch of a typical cavitating propeller, showing the various types of cavitation.	24
1-2	Panel arrangements for the first iteration (left) and subsequent iterations (right).	32
1-3	Convergence with number of iterations of the cavitation number and the cavity volume for a NACA16006 foil at $\alpha = 4^\circ$, $\frac{l}{c} = .5$. Results are shown for the present method (left) and Uhlman's method (right). . .	33
2-1	The propeller and cavity geometry, coordinate systems, and nonuniform inflow. x_S, y_S, z_S represent the ship-fixed coordinate system; x, y, z represent the propeller-fixed coordinate system. The point p is a point on the propeller surface, defined by the vector \vec{x} from the origin of the propeller-fixed system.	37
2-2	Definition of the flow boundaries on which the boundary conditions should be satisfied.	38
2-3	The approximate cavity surface on which the boundary conditions are applied.	40
2-4	Velocity diagram on the wake surface.	47
2-5	Definition of the cavity surface defined with respect to the blade surface.	49
2-6	Definition of the cavity surface defined with respect to the wake surface.	50
2-7	Definition of the cavity camber and height for a supercavitating section of the propeller blade.	52

3-1	NACA16006 hydrofoil at $\alpha = 4^\circ$ and $\sigma = 1.097$ (corresponding to the correct length $l = 0.4$). Left plot shows the predicted cavity shapes for different guesses of l . Right plot shows the resulting behavior of δ vs l .	57
3-2	Discretization of the propeller blade, the cavity, and their trailing wakes; $N=16$, $M=9$.	58
3-3	Indexing system for the discrete equations.	62
3-4	Definition of the arclength on a spanwise strip, used in the trapezoidal integration of $\frac{\partial \phi}{\partial s}$.	64
3-5	Schematic representation of the treatment of ϕ_0 .	65
4-1	Schematic of a cavity planform, showing the split panels.	70
4-2	Sketch defining split panel extrapolations.	71
4-3	Comparison of the source strength computed with a cavity-fit grid to that computed by the split panel method. In the plot on the left, $\frac{\partial \phi}{\partial n}_L$ is defined as a cubic extrapolation of neighboring unknowns. On the right, $\frac{\partial \phi}{\partial n}_L$ is defined as a cubic extrapolation with singular term, as in the text. Computations are for a NACA16006 foil with $\sigma = 1.0$, $\alpha = 3^\circ$, and a guess of the cavity length $\frac{l}{c} = 0.4$.	75
4-4	Investigation of the error due to representing two interior source panels with a single panel. The length of the unsplit panel is 1.0. The panel is split in half to form two sub-panels. The panel configuration and a sketch of the individual influences are shown above a plot of the ratio $\frac{B_L}{B_w}$.	76
4-5	Schematic of cavity height computation.	80

4-6	Spanwise $\delta(y)$ distributions for various cavity planforms on a rectangular hydrofoil which has a NACA65a crosssection. The curves are labeled 1-10 to correlate each cavity planform to its $\delta(y)$ curve. The thickness is $\frac{t}{c} = 0.05$ at the midspan, tapering elliptically to zero thickness at the tip. The angle of attack is $\alpha = 4^\circ$ and the cavitation number is $\sigma = 0.4$. The foil is twisted spanwise, and the angle of twist is given by $\alpha_t = -8y^3 + 12y^2$. The angle of twist is introduced to prevent the foil from cavitating near the tip.	83
4-7	Dependence of the cavity planform on σ , showing the existence of multiple solutions.	85
4-8	Effect of aspect ratio on multiplicity of solutions for a rectangular hydrofoil ($\frac{t}{c} = .05, \alpha = 5^\circ$). The cavity length at the midspan is shown vs $\frac{\sigma}{\sigma_c}$ for three aspect ratios $AR = 2, 5, 10$	87
4-9	Dependence of the cavity planform on δ_{tot} , for a rectangular hydrofoil with a span-chord ratio of 5 at an angle of attack of 5° . (For clarity, the span and chord are not drawn to scale.)	88
4-10	An example of a supercavitating elliptic hydrofoil at $\alpha = 3^\circ$ and $\sigma = .20$. The openness of the cavity at its trailing edge, $\delta(y)$ is shown also, where it can be seen that δ has a larger tolerance near the tip.	89
4-11	Convergence of the cavity planform with updating of the crossflow terms. Same foil and conditions as the previous figure.	90
4-12	Convergence of the cavity planform with updating of the crossflow terms. Rectangular hydrofoil at $\alpha = 3^\circ, \sigma = 0.5, \frac{l_0(y)}{c(y)} = .014$	91
4-13	Convergence of the cavity length with updating of the crossflow terms for a test propeller.	92
4-14	Nonlinear effect of foil thickness on cavity extent and volume. Cavity planforms and shapes at midspan are shown for rectangular hydrofoils, $\alpha = 5^\circ$, Aspect Ratio $AR = 5.0, t/c = .05, .09$ (span and chord are not drawn to scale).	93

4-15	$\delta(y)$ for a rectangular foil at $\alpha = 4^\circ$ and $\sigma = .16$ with a cavity length $\frac{l}{c}(y) = 0.5$ for all y . In this case ϕ_0 is defined as a quadratic extrapolation.	95
4-16	$\delta(y)$ for a rectangular foil at $\alpha = 4^\circ$ and $\sigma = .16$ with a cavity length $\frac{l}{c}(y) = 0.5$ for all y . In this case, ϕ_0 is defined as a cubic extrapolation with specified slope at the cavity leading edge.	95
4-17	Cavity length vs ωt for a NACA16006 2-D section at $\alpha = 4^\circ$ and $\sigma(t) = 1.2 + 0.2 \cos \omega t$. Shown are the quasi-steady and the unsteady solutions.	99
4-18	Cavity shapes from several time steps of the unsteady solution shown in the previous figure.	99
5-1	Convergence of spanwise and chordwise cavity thickness distributions with number of panels. The foil and cavity characteristics are described in the text.	102
5-2	Convergence of cavity planform (top plot) and cavity volume (bottom plot) with number of panels.	103
5-3	Convergence of cavity planform and cavity thicknesses with number of panels for the modified N4381 one-bladed propeller in steady flow; $J_S = 0.8$, $\sigma_n = 2.7$. The cavity detaches 2.4% of the local chord length aft of the leading edge at all spanwise locations.	104
5-4	Convergence of cavity planform with number of panels for the one-bladed AO-177 propeller in steady flow; $J_S = 0.6$, $\sigma_n = 2.5$. Shown also is the discretized blade for $(N, M) = (100, 20)$	107
5-5	Convergence, with revolutions and with time step size, of cavity volume history for the one-bladed test propeller operating in a nonuniform axial inflow. The axial inflow is shown at the top of the figure.	108
5-6	Results of a fully wetted consistency test. Circulation distributions from the fully wetted solution and the cavity solution. The two distributions should match because the potential on the cavity panels is set equal to the fully wetted potential.	110

5-7	Adapted grid fit to the shape of the cavity, used to compute the fully wetted flow on the modified foil/cavity boundary for the pressure validation shown in the next figure.	112
5-8	Pressure validation for a rectangular hydrofoil at $\alpha = 3^\circ$ and $\frac{\sigma}{\rho} = .105$. The cavity detaches at .4% of the chord length aft of the leading edge at all spanwise strips.	113
5-9	Pressure validation for a rectangular hydrofoil at $\alpha = 5^\circ$ and $\frac{\sigma}{\rho} = .105$. The cavity detaches at .4% of the chord length aft of the leading edge at all spanwise strips.	114
5-10	Pressure validation for a supercavitating elliptic hydrofoil at $\alpha = 3^\circ$ and $\frac{\sigma}{\rho} = .33$	115
5-11	Pressure validation for the test propeller at $J_S = 0.8$ and $\sigma = 2.7$. . .	116
5-12	Cavity planforms predicted by PUF-3A (with and without the leading edge correction) and the present method (implemented in the code PROPCAV) on the modified N4381 test propeller at $J_S = 0.8$ and $\sigma = 2.7$ in uniform flow.	117
5-13	Cavity volume histories predicted by PUF-3A (with and without the leading edge correction) and the present method on the test propeller at $J_S = 0.8$ and $\sigma = 2.7$ in nonuniform flow.	117
5-14	Cavity planform with and without inclusion of the hub for the test propeller at $J_S = 0.8$ and $\sigma = 2.7$ in steady flow.	119
5-15	Qualitative comparison between numerical results and experimental observation for an elliptic hydrofoil which is 12% thick with aspect ratio $AR = 3$ at $\alpha = 10^\circ$ and $\sigma = 0.6$. Photograph taken from Kato, et al (1992).	120
5-16	A reproduction of a photograph of a partially cavitating 3-D pitching hydrofoil. The cavitation number was $\sigma = .97$ and the reduced frequency of the pitching motion was $k = 1.0$. The picture was taken by Van Houten and found in MIT Marine Hydrodynamics Lab archives.	121

5-17	A comparison of experimental (measurements by Kinnas and Mazel) and numerical (computations by Fine) velocity profiles on a supercavitating 2-D hydrofoil in a water tunnel. Taken from Kinnas and Mazel (1992).	122
A-1	Hydrofoil and wake, showing the branch cut on the wake surface. . .	136
A-2	A blow-up of the field point p , showing the small patch of the surface replaced by a hemisphere of radius R	137
B-1	Convergence history of a fully nonlinear partial cavitation fixed-length solution. NACA16006 foil at $\alpha = 3^\circ$, $\frac{l}{c} = 0.4$ and $\frac{l_a}{c} = 0.0$. The termination model parameters are $\lambda = 0.1$, $A = 0.5$, and $\nu = 1.0$; the number of panels is $N = 100$. The cavitation number and cavity volume shown in the plot on the right are normalized on their converged values.	141
B-2	Pressure validation test for the first (top) and last (bottom) iterations of the nonlinear solution presented in the previous figure. Shown to the left of each pressure distribution is the corresponding panel arrangement for the fully wetted solution.	142
B-3	Convergence of cavity shapes, cavitation number, and cavity volume with number of iterations for a supercavitating NACA16006 foil at $\alpha = 3^\circ$, $\frac{l}{c} = 1.5$, $\frac{l_a}{c} = 0.05$, $\frac{\lambda_a}{c} = 0.05$, $\frac{\lambda_t}{c} = 0.05$. The number of panels is $N = 100$	144
B-4	Pressure validation of a supercavitating NACA16006 foil. Same foil and conditions as in Figure B-3.	145
B-5	Convergence of cavity shapes with number of iterations for the same foil and conditions as the previous figure, except that $\frac{l_a}{c} = 0.0$. In the blow up of the leading edge, it is clear that the nonlinear solutions cut the foil, while the linear solution does not.	146

B-6	Partially cavitating NACA16006 foil at $\alpha = 3^\circ$, $\lambda = 0.1$, $\nu = 1.0$, $A = 0.5$, $\sigma = .731$. The top plot shows the first and last iterations in the nonlinear fixed- σ solution. The last iteration corresponds to a σ -tolerance of 1%. Also shown is the converged nonlinear fixed- l solution. The bottom plot shows pressure validation for the first iteration and the fully nonlinear solutions.	148
B-7	Comparison of cavity shapes predicted from different methods for a NACA16 foil at $\alpha = 4^\circ$ (top), 6° (middle), and 8° (bottom), and $\frac{l}{c} = .06$ (left) and $.09$ (right). The ratio $\frac{a}{c}$ is kept fixed at $.055$. The cavity detaches at the leading edge in all cases.	150
B-8	Comparison of supercavity shapes predicted from linear theory, the present method, and nonlinear theory for a NACA16004 foil at $\alpha = 4^\circ$ (top), $\alpha = 6^\circ$ (middle), and $\alpha = 8^\circ$ (bottom). The ratio $\frac{a}{c}$ is kept fixed at 0.440 . In each case, the cavity detaches at the leading edge.	153
B-9	An example of the original method for finding the nonlinear fixed- σ solution. The convergence is seen here to be very slow.	154
B-10	The effect of detachment point on the partial cavitation solution. Shown are four solutions corresponding to detachment points $\frac{l_a}{c} = 0, .004, .016$ and $.035$. The foil is NACA16006 at $\alpha = 3^\circ$ and $\sigma = 0.7$. The termination model parameter λ is zero.	156
C-1	A depiction of the cavity height law for partial cavitation.	158
C-2	An example of a partial cavity solution using the height law termination model. Shown are the cavity shape and pressure distribution for a NACA16006 foil at $\alpha = 4^\circ$ with a cavity length of $\frac{l}{c} = 0.4$. The length of the transition zone is $\frac{\lambda}{c} = 0.15$	160
C-3	A depiction of the pressure law for partial cavitation.	161
C-4	Cavity shapes, cavitation numbers and cavity volumes for different values of the parameters λ and ν	162

C-5	Cavity shapes for different values of the parameter A . NACA16006 foil with $\alpha = 4^\circ$ and $\frac{l}{c} = 0.5$	162
C-6	A sketch of the end-parabola model for supercavitation.	163
C-7	Results of linear theory and nonlinear theory using the end parabola model. NACA16006 foil at $\alpha = 10^\circ$ and $\alpha = 18^\circ$. The cavity length is $\frac{l}{c} = 2.0$; the cavity detaches at the leading edge. The length of the transition zone is $\lambda = .05$	165
C-8	A sketch of the curved end-plate model for supercavitation.	166
C-9	A blow-up of the transition zone, showing how the cavity is updated between iterations with the curved end plate termination model. . . .	167
C-10	Cavity shapes (from linear theory and nonlinear theory) and pressure distributions (from nonlinear theory) for a flat plate hydrofoil at $\alpha =$ 30° . The slope continuity of the pressure distribution is shown to depend on the parameters λ_l and λ_u	168
C-11	A depiction of the pressure law for supercavitation.	169

List of Tables

4.1	Test propeller geometry, identical to the AO-177 propeller, except the skew is zero.	92
5.1	The DTMB propeller N4381, with modified pitch distribution to unload the tip (referred to in the text as the "test propeller").	105
5.2	The AO-177 propeller geometry.	106
5.3	Harmonic coefficients A_n for the nonuniform axial inflow velocity. . .	106
B.1	Convergence with number of panels for a partially cavitating NACA16006 symmetric foil at $\alpha = 3^\circ$, $\frac{l}{c} = 0.5$ and $\frac{l_a}{c} = 0.048$. The termination model parameters are: $\frac{\lambda}{T} = 0.1$, $A = 0.3$ and $\nu = 1.0$ (for the definition of these parameters, see Appendix C).	140
B.2	Convergence with number of panels of the fixed-length solution for a supercavitating NACA16004 symmetric foil at $\alpha = 5^\circ$, $\frac{l}{c} = 2.0$ and $\frac{l_a}{c} = 0.024$. The termination model parameters are: $\frac{\lambda^*}{T} = 0.07$, $\frac{\lambda}{T} = 0.07$ (for the definition of these parameters, see Appendix C). The number of panels is $N = 100$	143
B.3	Convergence with number of panels of the partial cavitation fixed- σ solution for a NACA16006 symmetric foil at $\alpha = 4^\circ$, $\sigma = 0.7$ and $\frac{l_a}{c} = 0.024$. The termination model parameters are: $\frac{\lambda}{T} = 0.1$, $A = 0.3$, and $\nu = 1.0$. The panels are arranged with cosine spacing, as shown above for $N=60$	147

B.4	Varying the initial guess for the same foil and conditions as in the Table A.3. The number of panels is $N=80$, and the panel arrangement is shown above.	149
B.5	Convergence with number of panels for a NACA16006 symmetric foil at $\alpha = 6^\circ$, $\sigma = 0.2$ and $\frac{l_a}{c} = 0.0$	152
C.1	The effect of parameters on the cavity solution using the pressure law termination model. Computations are for a NACA16005 thickness form with a NACAa.8 camber profile with a maximum camber of .03. $\alpha = 4^\circ$, $\frac{l}{c} = 1.5$, $\frac{l_a}{c} = 0.01$ and $A = 0.1$	169
C.2	The difference between the curved end plate model and the pressure law model for the same flow geometry as in the previous table. The pressure law termination model parameters are: $\lambda_1 = 0.1$, $\lambda_2 = 0.3$, $\delta^* = 0.1$, and $A = 0.1$. The end plate termination model parameters are: $\lambda_l = 0.11$ and $\lambda_u = 0.15$	170

NOMENCLATURE

$A_n(r), B_n(r)$	harmonic coefficients of the effective wake inflow
A	a termination model parameter for the pressure law, defined in Appendix C
AR	aspect ratio
A_{inm}^k	the potential induced at the i^{th} control point on the key blade by a unit strength dipole at the n^{th} panel on the m^{th} strip of the k^{th} blade
B_{inm}^k	the potential induced at the i^{th} control point on the key blade by a unit strength source at the n^{th} panel on the m^{th} strip of the k^{th} blade
C_{inm}^k	the potential induced at the i^{th} panel on the key blade due to a unit strength source at the n^{th} panel on the m^{th} strip of the wake of the k^{th} blade
C	the cavity camber in the wake
c	2-D hydrofoil chord length
$c(r), c(y), c_m$	propeller blade or 3-D hydrofoil sectional chord length, at the spanwise location (r for propellers, y for hydrofoils, m for the discrete geometry)
D	propeller diameter
D_{inm}^k	the potential induced at the i^{th} wake control point by a unit strength dipole at the n^{th} panel of the m^{th} strip of the k^{th} blade
E_{inm}^k	the potential induced at the i^{th} wake control point by a unit strength source at the n^{th} panel of the m^{th} strip of the k^{th} blade
f	algebraic pressure recovery function
F_{inm}^k	the potential induced at the i^{th} wake control point due to a unit strength source at the n^{th} wake panel on the m^{th} wake strip of the k^{th} blade

$G(p; q)$	Green's function; $G(p; q) = 1/R(p; q)$, where $R(p; q)$ is the distance between points p and q
g	gravitational acceleration
h	the cavity thickness over the blade surface
h_w	the cavity thickness over the wake surface
J_s	advance coefficient based on ship speed $J_s = \frac{V_s}{nD}$
k	blade index
k	reduced frequency
l	cavity length, defined as a fraction of the nose-tail line
$l(r)$	cavity length on the propeller blade at radius r , defined as the arclength of the projection of the cavity on the nose-tail helix
l_0	chordwise distance between the blade (or foil) leading edge and the cavity leading edge
M	number of spanwise panels
m	spanwise panel index
N	number of chordwise panels
N_B	number of blades
N_{WS}	number of wetted panels on the blade surface
N_{CB}	number of cavitating panels on the blade surface
N_{CW}	number of cavitating panels on the wake surface
N_{LE}	number of suction side panels on each blade strip $\frac{N}{2}$ plus the number of wetted panels in front of the cavity on the pressure side
N_{C_m}	number of cavitating panels on the m^{th} strip of the wake surface
N_{sp}	number of panels on the blade surface which are "split" by the trailing edge of the cavity
N_W	number of dipole panels arrayed on each strip of the wake

n	propeller revolutions per unit time
n	chordwise panel index
n_{sp_m}	the chordwise index of the split panel on the m^{th} strip of the blade
\bar{n}	time step index
\hat{n}	unit normal to blade or wake surface
p	pressure
p_0	pressure far upstream of the propeller disk in the shaft axis
p_c	pressure inside and on the cavity
q	total velocity vector
q_t	total velocity on the cavity surface
q_w	wake source strength; $q_w = \frac{\partial \phi^+}{\partial n} - \frac{\partial \phi^-}{\partial n}$, where $\frac{\partial \phi^+}{\partial n}$ and $\frac{\partial \phi^-}{\partial n}$ are the normal velocities on the upper and lower wake surfaces
r	radial coordinate
S_C	the exact cavity surface
S_{CB}	the blade surface
S_{CW}	the part of the wake surface which is overlapped by a supercavity
S_W	the wake surface
S_{WS}	the wetted blade surface
s	arclength beneath the cavity on the foil surface
s	streamwise coordinate on the surface of the blade or wake
\hat{s}	unit normal in the s direction
s_{TE}	the value of arclength s at the cavity trailing edge
s_T, s_L	the value of arclength s at the beginning and end of the transition zone, respectively; used in termination models
U_W	the effective wake inflow velocity

U_{in}	the relative inflow; sum of effective wake and rotational velocity
U_s, U_v, U_n	s, v , and n components of the relative inflow U_{in}
u	spanwise coordinate normal to both s and n and forming a right-hand coordinate system
v	spanwise coordinate, <i>not</i> orthogonal to s , on the surface of the blade (formed by normalizing the vector between the midpoints of the two opposite sides (facing spanwise) of each panel)
\hat{v}	unit normal in the v direction
V_x, V_r, V_t	axial, radial and tangential components of U_w
V_S	ship speed
W_{iml}^k	the potential induced at the i^{th} control point on the key blade by a unit strength dipole at the l^{th} panel of the m^{th} strip of the wake of the k^{th} blade
W_{iml}^{*k}	the potential induced at the i^{th} wake panel by a unit strength dipole lying on the m^{th} strip of the wake of the k^{th} blade
x, y, z	propeller-fixed coordinate system
x_S, y_S, z_S	ship-fixed coordinate system
α	hydrofoil angle of attack
δ	the openness of the cavity at its trailing edge, defined as the value of h or h_w at the cavity trailing edge (normalized on local chord length, c_m)
δ_{tol}	the tolerance set on δ corresponding to a converged planform
ϕ_p, ϕ_q	perturbation potential at a field point and an integration point, respectively
ϕ_0	perturbation potential at the cavity leading edge

- Φ total potential, defined as the sum of the inflow potential and the perturbation potential for 2-D flows
- $\Gamma(r, t)$ the circulation around the blade at radius r and time t
- θ the circumferential propeller coordinate
- θ the local angle between s and v ; $\hat{s} \cdot \hat{v} = \cos \theta$
- ρ fluid density
- σ cavitation number based on U_∞ ; $\sigma = \frac{p - p_c}{\frac{1}{2} \rho U_\infty^2}$
- σ_n cavitation number based on propeller rotation; $\sigma = \frac{p - p_c}{\frac{1}{2} \rho n^2 D^2}$
- ω propeller rotational speed

Chapter 1

Introduction

A typical marine propeller operates in a flow field which is circumferentially nonuniform. The variation in the inflow is due primarily to the proximity of the ship's boundary layer, but may also be effected by shaft inclination, ship maneuvers, and the presence of upstream appendages. This nonuniformity often causes intermittent blade cavitation, which in turn is responsible for a host of undesirable effects. The most conspicuous of these are: excessive vibratory shaft forces, unsteady radiated pressures (which occasionally result in structural failure of nearby hull plating), blade surface erosion, and inboard airborne noise levels in excess of regulatory standards. All of these detrimental effects are associated with the growth and collapse of vapor-filled cavities and the attendant radiated pressure field.

With recent increases in the demand for heavily loaded efficient propellers, cavitation has become less and less avoidable. As a result, it has become the task of the hydrodynamicist to predict the cavitation characteristics of a particular geometry at the design stage, with the expectation that analytical methods can be used to avoid excessive cavitation within an appropriate range of ship speed. Computational tools for the reliable prediction of propeller cavitation are therefore in high demand.

Cavitation on marine propellers and hydrofoils is a complex phenomenon. It may be characterized by any combination of the three forms (as delineated by Tulin [66]): sheet, travelling bubble, or cloud cavitation (see Figure 1-1). A sheet cavity appears as a single vapor bubble with a smooth, glossy surface attached to the blade near

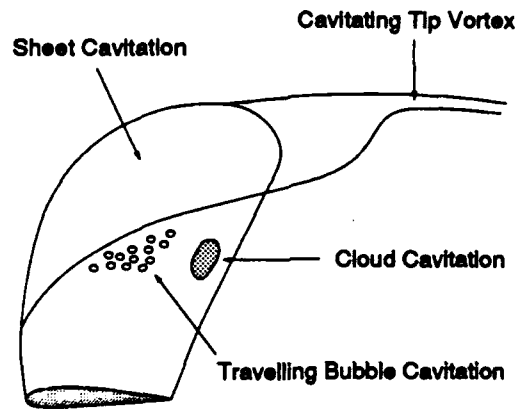


Figure 1-1: A sketch of a typical cavitating propeller, showing the various types of cavitation.

its leading edge and extending downstream to a region of collapse. The pressure inside and on the sheet cavity is usually assumed to be constant and equal to the vapor pressure. Although a sheet cavity can be transient, it is often assumed that the mechanism of unsteadiness is the variations in the inflow or in the hydrostatic pressure. In reality, the sheet cavity is not a smooth, constant pressure surface. Even in a uniform flow field, the sheet cavity is inherently unsteady due to the occasional (sometimes periodic) breakoff of the cavity trailing edge and the entrainment of travelling bubbles in the cavity wake. Transience is also introduced at the cavity surface, which in general is a bubbly, frothy region of continuous vaporization and condensation. Wade and Acosta observed the sheet cavity on a plano-convex hydrofoil to be a rough, boiling surface without definite structure [74]. As noted by Tulin, however, it is plausible that the exterior flow sees mainly the effect of a coherent cavity surface on which the pressure is constant [66]. This observation is central to justifying the application of sheet cavity theory, as is done in this thesis.

In travelling bubble cavitation, distinct vapor bubbles grow and collapse over the surface of the blade as they travel from regions of low pressure to regions of high pressure. The coalescence of clusters of travelling bubbles seems to play an important role in the formation of a sheet cavity in some circumstances. However, this process is not well understood. Modelling bubble cavitation is also problematic. While the

growth and collapse of a single spherical bubble is treated by Rayleigh-Plesset theory [41], no adequate theory exists to treat clusters of individual bubbles in the presence of solid boundaries. Nonetheless, some progress has been made in recent years in applying analytical and numerical methods to model the behavior of multiple bubble clusters [6, 8, 19]. An example is the work of Chahine, who has used a boundary-value approach and applied a surface panel method to multiple collapsing bubbles [6].

Downstream of a collapsing sheet cavity is often observed a wake-entrained cluster, or cloud, of very small bubbles. The collapse of the cavitation cloud — usually near the trailing edge of a propeller blade where the cloud is subject to a positive pressure gradient— is known to cause severe surface erosion. The phenomenon has thus far defied mathematical modelling.

Associated with cavitating propellers are hub and tip vortices which may have vapor-filled cores. The cavitating tip vortex often exceeds in volume the sheet cavity and has a marked effect on the local flow at the tip. The process of cavitation inception is not well understood, nor are the roles of viscosity or nucleation. Propeller sheet cavities in nonuniform flow are sometimes observed to collapse inward from the leading edge and to disintegrate into a cloud cavity. The effect of viscosity on the cavity flow, which has been observed mainly to be a determinant of the point of detachment [2, 13], has yet to be included in any propeller analysis tool.

At the present time, there are essentially two distinct avenues for modelling cavitation. One is to treat the cavity strictly as a constant pressure sheet, while the other is to consider the cavity to be a cluster of bubbles. An example of the latter approach is the work of Kubota et al [43], who solve the compressible Navier-Stokes equations while treating the two-phase flow as a single-phase compressible fluid with drastically varying density. They allow a bubble cluster to grow and collapse according to Rayleigh's pressure/volume relationship for noninteracting spherical bubbles. Initial results compare qualitatively well with experiments. However, the method is hampered by a bubble model which does not capture the effects of bubble-bubble interaction or those of bubble non-axisymmetry. It has been shown that these effects are very important to the prediction of bubble collapse and the resulting high

impact point loads and generation of acoustic noise [6]. Nonetheless, with inevitable improvements, this method may lead the way to a more complete understanding of the phenomenon.

The approach taken in this work is to treat propeller cavitation strictly as sheet cavitation. The advantage of this approach lies in its relative mathematical simplicity. For example, if the flow is assumed to be potential in nature (irrotational and incompressible flow of an inviscid fluid), then the governing equation in steady flow is a *linear* elliptic partial differential equation for a single scalar. The use of surface singularities and the now classic application of Green's 3rd identity are well suited for such a problem. The disadvantages of this approach are the neglect of viscosity, vortex cavitation, bubble cavitation, and cloud cavitation. However, there are two additional rationales for taking the potential flow avenue. First, it is believed that the first-order contributor to dynamically varying blade loads and radiated pressures is the transient sheet cavity [66]. Second, many or all of the neglected phenomena may be included as refinements to the potential flow solution. For example, a viscous-inviscid boundary layer interaction could be used to model the effects of viscosity. As another example, a local tip solution, including a cavitating tip vortex, could be matched to the outer sheet cavity solution. The potential of such a model to capture most of the physics at reasonable computational expense is the motivation for obtaining an *accurate, efficient, and robust* potential flow solution. This is the goal of this thesis.

1.1 Objectives

The objective is to develop a robust and computationally efficient *nonlinear* method of predicting unsteady propeller sheet cavitation and its resulting free-space potential field. The approach is to use a low order potential based boundary element method to obtain the steady state oscillatory sheet cavity solution, including an accurate prediction of the cavity history. Emphasis is placed on obtaining accurate prediction of cavity planforms and shapes. It is expected that such a solution will improve the

accuracy of the prediction of cavitation-induced unsteady blade load distributions and hull vibratory excitations. This in turn will improve the identification of unacceptable propeller or hull designs early in the design process, resulting in a more cost-effective design.

1.2 Fundamental Assumptions

The propeller blades are assumed to be rigid bodies arranged symmetrically around a common axis and rotating with constant angular velocity in an unbounded fluid. The presence of other solid boundaries, such as the hull, duct or struts, is ignored. The hub, however, may be included in the analysis. The inflow is known and represents the wake field of the ship. It is assumed to be the *effective* wake which includes the interactions between the vorticity of the inflow in the absence of the propeller (the *nominal* wake) and the vorticity due to the propeller [29, 27]. The inflow is assumed to be constant over the axial extent of the propeller.

The fluid is assumed to be inviscid and free of impurities and the resulting flow to be incompressible and irrotational. The cavity is assumed to be a constant-pressure surface which grows on the suction side of a blade when the local pressure falls below the vapor pressure and collapses when it rises above it. The pressure side of the blade is assumed to be cavity-free. The cavity is assumed to be a sheet cavity; neither travelling bubble nor cloud cavitation is included in the model. Cavitating tip and hub vortices are also excluded from the analysis. The detachment line of the sheet cavity (the locus of all spanwise points where the cavity begins) is assumed to be known.

Despite the drastic simplification, the problem at hand remains a daunting one. The main difficulty in the analysis of sheet cavitation arises from the need to determine the free streamline (the cavity surface) on which the pressure is prescribed. The fact that the location of a portion of the flow boundary is unknown makes the problem strongly nonlinear. The inherent complexity of three dimensional flows adds to the difficulty in the analysis. Variation in cavity extent is often nonlinear in time,

since a typical propeller blade operating in a ship wake goes from fully wetted to supercavitating and back to fully wetted within a fraction of a revolution.

Perhaps it was these compounded complexities which prompted Batchelor to state the following:

If the shape of the permanent cavity under different conditions could be predicted, the propeller could be designed to allow for the existence of the cavity, but this is not possible in general.

G.K. Batchelor, in An Introduction to Fluid Dynamics [3]

Batchelor was only partly correct in this statement. Propeller *design* is still done with only approximate account taken of the effects of cavitation. However, advances in high speed computing have allowed for the *analysis* of three dimensional sheet cavities on given geometries. Prediction of propeller sheet cavitation may now be included in the overall design process.

1.3 Previous Research

1.3.1 2-D Free Streamline Flows

The solution of the 2-D free streamline problem began with Helmholtz and Kirchoff, who solved for the flow around flat plate or polygonal bodies at zero cavitation number. These were exact solutions which made use of the hodograph technique, which was introduced by Helmholtz more than a century ago [4]. The method was later extended to treat curved bodies at zero cavitation number by Levi-Civita [4]. The theory was applied by Wu and Wang [76] and later by Furuya [14] for the analysis of supercavitating hydrofoils in the presence of a free surface.

The extension to non-zero cavitation number resulted in a diversity of termination models. Among these, the most popular are the Riabouchinsky model [58, 60, 61], the re-entrant jet model [9, 42], the open wake model [10], and the spiral vortex models [65]. Among researchers, there has been no consensus regarding which model is best suited to represent cavity flows. A comprehensive review of termination models may

be found in [75] and [63]. A description of termination models developed in this thesis is included in Appendix C.

Despite producing exact solutions, the hodograph method with the various termination models were never widely used due to the inherent difficulty in treating general shaped bodies and the restriction to planar flows. These deficiencies led to the introduction of linear theory.

1.3.2 2-D Linear Theory

The solution of two-dimensional cavity flows for general geometries became more accessible with the development of linear theory, as introduced by Tulin for general shape supercavitating hydrofoils at zero cavitation number [63], and later at non-zero cavitation number [64]. Linear theory was first applied to partially cavitating hydrofoils by Acosta [1] and Geurst and Timman [16], independently. The linear cavity theory, which closely resembles the classical thin-wing theory, assumes thin cavity and foil thickness relative to the foil chord length and, as a result, simplifies the dynamic boundary condition from the requirement of constant total velocity to that of constant horizontal perturbation velocity. This boundary condition is applied, together with the linearized wetted surface kinematic boundary condition, on a projection of the hydrofoil surface on the free stream axis. Linear cavity theory has been applied by several researchers for the analysis of partial and supercavitating flows around special and general shape 2-D hydrofoil geometries. A list of references which address the application of linear cavity theory may be found in [67] or [33].

1.3.3 3-D Cavity Flows

The flow around cavitating finite span hydrofoils¹ was first treated in a stripwise sense with the three dimensional flow effects introduced by matching the inner solution (from either linear or nonlinear theory) with the solution from lifting line theory in the outer domain. This approach was used to study supercavitating hydrofoils by

¹ Also called 3-D hydrofoils in this work.

Nishiyama [56], Leehey [48] and Furuya [15] and partially cavitating hydrofoils by Uhlman [68]. However, this method is valid only for high aspect ratio hydrofoils and its accuracy deteriorates near the hydrofoil tips. The complete three dimensional flow effects, in the context of linear cavity theory, were included in the analysis of supercavitating 3-D hydrofoils by Widnall [59], who employed a numerical pressure doublet and source lifting surface technique. Jiang and Leehey instead applied a discrete vortex and source lattice lifting surface technique [25], and also introduced an iterative scheme to determine a cavity planform corresponding to a uniform cavitation number spanwise. The use of the vortex/source lattice led to the treatment of fully wetted propellers in unsteady flow by Kerwin and Lee [32], which was then extended to the analysis of unsteady sheet cavitation by C-S. Lee [45] and Breslin et al [5]. These researchers also introduced the ability to treat mixed cavity patterns in partial and supercavitation.

1.3.4 Nonlinear Solutions

Due to the success of thin wing theory in the analysis of fully wetted flows, one might assume that linear cavity theory would be appropriate for analyzing hydrofoil or propeller sheet cavitation. However, a serious defect of the linear theory arises in the case of partially cavitating flows around hydrofoils with rounded leading edges. In particular, linear theory predicts that the cavity extent and volume should increase with increasing thickness provided that the flow conditions remain the same. On the contrary, the short cavity theory of Tulin and Hsu [67] and the numerical nonlinear surface vorticity method developed by Uhlman [70], predict that the cavity size should *decrease* with increasing thickness. In addition, it is known from experimental evidence that increasing the leading edge radius delays or reduces leading edge cavitation. This defect in the linear cavity theory was recently addressed by Kinnas [33], who introduced the nonlinear *leading edge correction* to account for the breakdown of the linear cavity solution in the vicinity of a round leading edge. The nonlinear blade thickness effects have also been included in the linearized method for the analysis of unsteady propeller cavitation [45] by implementing the leading edge correction locally

at planes normal to the blade leading edge [31, 34].

Numerical nonlinear solutions have evolved because of the defect in the linear theory. Various velocity-based boundary element methods (BEM's) have been applied for the analysis of the flow around 2-D and 3-D partially and supercavitating hydrofoils. These include methods by Pellone and Rowe [57], for supercavitating 2-D and 3-D hydrofoils; by Uhlman [70, 71], for partially and supercavitating 2-D hydrofoils; and by Lemonnier and Rowe [20], for partially cavitating 2-D hydrofoils. In each of these BEM's, the exact cavity boundary is determined by an iterative process in which the dynamic boundary condition is satisfied on an approximate cavity surface and the kinematic boundary condition is used to update the surface. The iterations terminate when both the kinematic *and* the dynamic boundary conditions are satisfied on the computed cavity surface. In order to solve the problem, all of these techniques assume that the cavity extent is known; the cavitation number is part of the solution.

Each of the numerical nonlinear methods requires modest computer effort to solve the 2-D problem, but their extension to 3-D was limited due to slow rates of convergence to the fully nonlinear solution. If a numerical nonlinear method was to be applied to 3-D geometries, a better tool was needed.

1.3.5 Present Method

In the present method, a potential based boundary element method (*i.e.*, one based on Green's third identity for the perturbation potential) is applied to the propeller sheet cavity problem in unsteady flow. The method was first applied to find the fully nonlinear fixed-length solution² for partially and supercavitating 2-D hydrofoils in steady flow, as reported in [35]. An iterative method was employed to find the exact cavity shape, similar to the one described in the previous section for the velocity-based methods. In the first iteration, the panels representing the cavity were placed on the foil surface. In subsequent iterations, the cavity surface was updated and the

²In the fixed-length solution, the length is specified and the cavitation number is unknown.

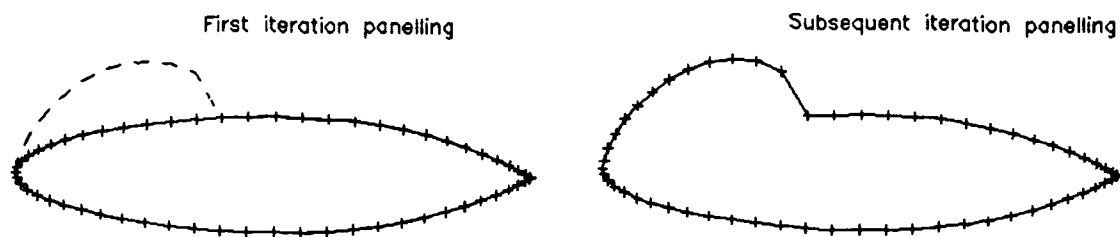


Figure 1-2: Panel arrangements for the first iteration (left) and subsequent iterations (right).

panels moved to the updated surface (see Figure 1-2). At that time, the method was characterized by very rapid convergence to the fully nonlinear solution and the remarkable accuracy of the first iteration. The convergence of the cavitation number and cavity volume with iterations is much faster for the potential based method than for the velocity based methods. This contrast is shown in Figure 1-3, which shows the results of the present potential based method and the results of Uhlman's velocity based method [71] for a NACA16006 hydrofoil at angle of attack $\alpha = 4^\circ$ and cavity length-to-chord ratio $\frac{l}{c} = 0.5$.

In a similar method developed at the same time by Lee et al [47], similar behavior of the solution with iterations was found. However, in that work a termination model was not applied. The importance of applying a termination model in the nonlinear solution is discussed in Appendix C.

In addition to the quick convergence, the first iteration cavity area differed from the converged nonlinear area by no more than 2% (see Appendix B) for partially cavitating hydrofoils at a wide range of angles of attack. It was recognized then that such accuracy could represent substantial savings and render a fully three dimensional nonlinear solution computationally feasible if a single iteration toward the nonlinear solution is sufficient.

The method was then extended to treat 2-D and 3-D partially cavitating hydrofoils

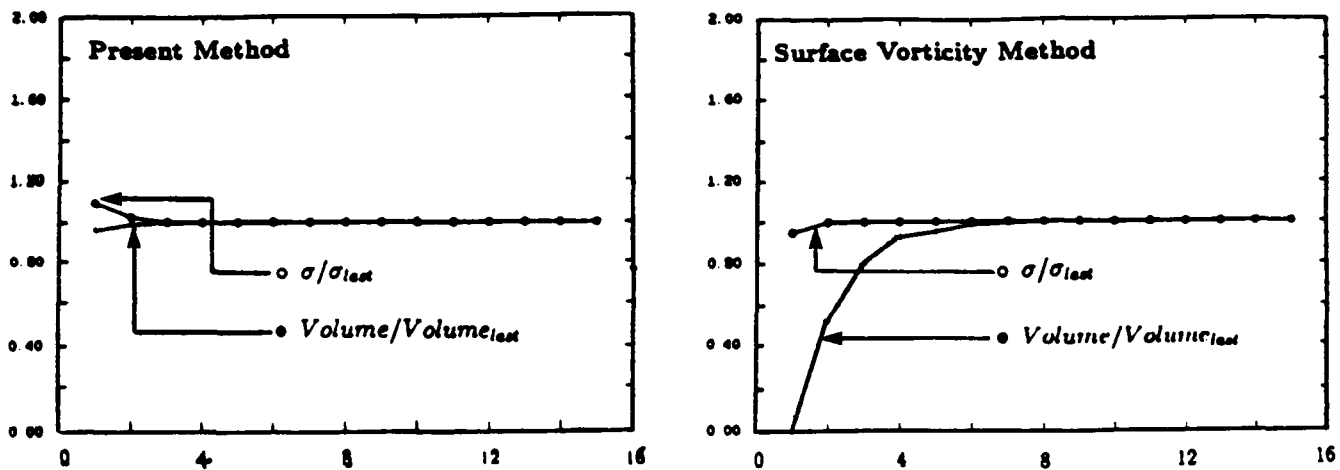


Figure 1-3: Convergence with number of iterations of the cavitation number and the cavity volume for a NACA16006 foil at $\alpha = 4^\circ$, $\frac{l}{c} = .5$. Results are shown for the present method (left) and Uhlman's method (right).

for the more realistic case where the cavitation number is known and the cavity extent must be determined [37]. In the 3-D extension, the fully three dimensional, nonlinear and time dependent boundary conditions were applied. The development of an efficient and robust iterative algorithm to find the cavity extent was central to this work. Next, the model was extended to treat supercavitation, along with the more difficult problem of treating mixed partial/supercavity patterns. The emphasis at this stage was to develop a *uniform* analytical approach, one that made use of a single algorithm to compute general shape planforms including partial and supercavitation. The method was tested extensively for convergence and consistency. The results of this part of the research were reported in [13].

In the 3-D hydrofoil nonlinear solution, only the first iteration is performed. Based on the accuracy of the 2-D first iteration solution, it was deemed unnecessary to continue iterating. Obviously, this decision was also motivated by the extensive computer effort necessary in solving 3-D flows. Despite the approximation, the nonlinear character of the solution has been preserved, and the solution is found with moderate CPU expense. In the remainder of this thesis, the solution will be called *nonlinear* in order to differentiate it from the *linear* solution. The converged nonlinear solution

will be referred to as *fully nonlinear*.

The latest extension of the method involved the treatment of cavitating propellers, in either uniform or nonuniform inflow. The details of the method will be described in this thesis mainly in the context of propellers in nonuniform flow.

Chapter 2

Mathematical Formulation

In this chapter, a precise definition of the problem is written down. Green's formula is applied on an approximate flow boundary, which includes a portion of the zero-thickness wake sheet, and this necessitates special treatment of the boundary integral equation in order to extract the correct local contributions. Following this, detailed derivations of the fully three-dimensional nonlinear boundary conditions are provided.

2.1 Definition of the Problem

Consider a cavitating propeller subject to a nonuniform inflow $U_W(x_S, r_S, \theta_S)$, with the subscript S denoting the ship-fixed coordinate system in which the wake is defined. As mentioned, U_W is assumed to be the *effective* wake. Some details of the geometry are shown in Figure 2-1. The solution is found in the (x, y, z) coordinate system, which rotates with the propeller. The propeller is assumed (without loss of generality) to be right-handed and to rotate at a constant angular velocity ω . The inflow relative to the propeller is

$$U_{in}(x, y, z, t) = U_W(x, r, \theta - \omega t) + \omega \times \mathbf{x} \quad (2.1)$$

where $r = \sqrt{y^2 + z^2}$, $\theta = \arctan(\frac{z}{y})$, and $\mathbf{x} = (x, y, z)$. The inflow velocity U_W is expressed in terms of its axial, radial and tangential components (labeled V_a , V_r , and V_t , respectively). The components are defined in terms of harmonic coefficients as

follows

$$\begin{aligned}
\frac{V_x(r, \theta)}{V_s} &= A_1^x(r) + \sum_{n=2}^{NHARMA} A_n^x(r) \cos n\theta + \sum_{n=2}^{NHARMA} B_n^x(r) \sin n\theta \\
\frac{V_r(r, \theta)}{V_s} &= A_1^r(r) + \sum_{n=2}^{NHARMR} A_n^r(r) \cos n\theta + \sum_{n=2}^{NHARMR} B_n^r(r) \sin n\theta \\
\frac{V_t(r, \theta)}{V_s} &= A_1^t(r) + \sum_{n=2}^{NHARMT} A_n^t(r) \cos n\theta + \sum_{n=2}^{NHARMT} B_n^t(r) \sin n\theta \quad (2.2)
\end{aligned}$$

where A_n and B_n are the harmonic coefficients and the superscripts x, r and t denote axial, radial and tangential components [28]. The leading coefficient A_1 is the mean value. The angular coordinate θ is positive in the clockwise direction looking downstream (see Figure 2-1). $NHARMA$, $NHARMR$ and $NHARMT$ are the number of harmonics which are used to describe a given inflow. The inflow velocity components vary only radially and circumferentially; they are assumed to be constant over the axial extent of the propeller.

For the moment, assume that the propeller has a developed sheet cavity whose time-dependent surface is denoted by $S_C(t)$, as shown in Figure 2-1. The fluid is assumed to be inviscid and the resulting flow to be incompressible and irrotational. In this case, the time-dependent total flow velocity $q(x, y, z, t)$, can be written in terms of the perturbation potential, $\phi(x, y, z, t)$, as follows:

$$q(x, y, z, t) = U_{in}(x, y, z, t) + \nabla \phi(x, y, z, t). \quad (2.3)$$

The goal is to determine the potential field $\phi(x, y, z, t)$, as well as the cavity surface $S_C(t)$. Once ϕ is known, the pressure distribution may be computed by numerically differentiating the potentials and applying Bernoulli's equation. The unsteady blade load distribution may then be determined by integrating the pressure. Knowing $S_C(t)$, the cavity volume history may be computed. In the following sections, the equations and boundary conditions necessary for the solution will be derived.

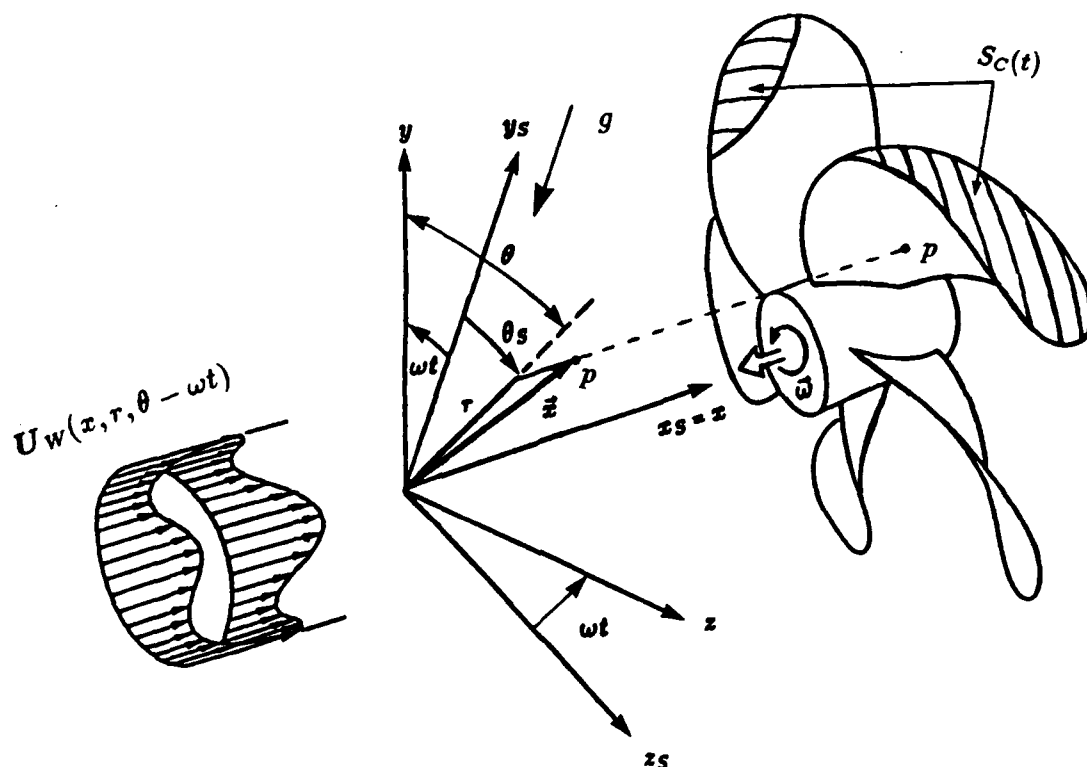


Figure 2-1: The propeller and cavity geometry, coordinate systems, and nonuniform inflow. x_S, y_S, z_S represent the ship-fixed coordinate system; x, y, z represent the propeller-fixed coordinate system. The point p is a point on the propeller surface, defined by the vector \vec{x} from the origin of the propeller-fixed system.

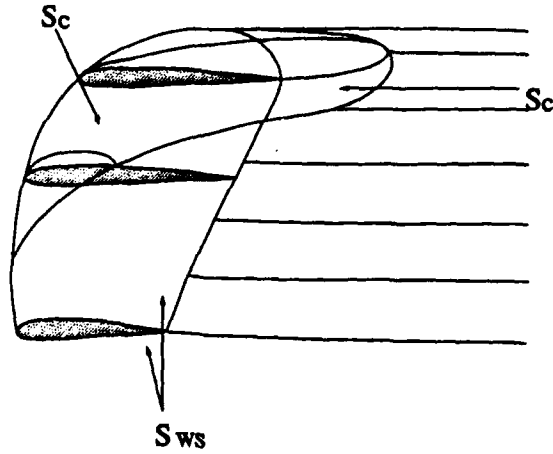


Figure 2-2: Definition of the flow boundaries on which the boundary conditions should be satisfied.

2.2 Green's Formula

The perturbation potential $\phi_p(x, y, z, t)$ at any point p which lies either on the wetted blade (or hub) surface¹, $S_{ws}(t)$, or on the cavity surface, $S_c(t)$, (both surfaces are shown in Figure 2-2) must satisfy Green's third identity:

$$\begin{aligned}
 2\pi\phi_p(t) = & \int_{S_{ws}(t) \cup S_c(t)} \left[\phi_q(t) \frac{\partial G(p; q)}{\partial n_q(t)} - G(p; q) \frac{\partial \phi_q(t)}{\partial n_q} \right] dS + \\
 & + \int_{S_w(t)} \Delta \phi_w(r_q, \theta_q, t) \frac{\partial G(p; q)}{\partial n_q(t)} dS; \quad p \in (S_{ws} \cup S_c) \quad (2.4)
 \end{aligned}$$

The subscript q corresponds to the variable point in the integrations. $\hat{n}_q(t)$ is the unit vector normal to the surface of the propeller, the cavity, or the wake. The unit normal points *into* the fluid (on the wake surface, $\hat{n}_q(t)$ is oriented such that it points in the same general direction as the normal on the *suction* side of the blade). $\Delta \phi_w(r, \theta, t)$ is the potential jump across the wake sheet, $S_w(t)$, and $G(p; q) = 1/R(p; q)$ is Green's function, where $R(p; q)$ is the distance from the field point p to the variable point q .

Equation (2.4) expresses the perturbation potential on the surface formed by the

¹The wetted blade surface is that part of the blade which is not cavitating.

union of the cavity and blade surfaces, $S_{WS}(t) \cup S_C(t)$, as a superposition of the potentials induced by a continuous source distribution, G , and a continuous dipole distribution, $\frac{\partial G}{\partial n}$, on $S_{WS}(t) \cup S_C(t)$, and a continuous dipole distribution on the trailing wake surface, $S_W(t)$. The application of Green's 3rd identity to problems in potential flow is classic [44, 50, 54], while applications to propeller and rotor flows are more recent [49, 51, 21, 22, 30, 38].

Ultimately, the exact nonlinear potential flow solution will be found when the kinematic and dynamic boundary conditions (which may be applied simultaneously with Green's formula (2.4)) are satisfied on the *exact* flow boundary. However, we face the usual problem that the position of the cavity surface is unknown. As a first iteration towards the fully nonlinear solution, we may apply the boundary conditions on an *approximate* flow boundary. A natural choice of an approximate boundary is defined as follows:

- it coincides with the blade surface (including the part of the blade beneath the cavity). This surface will be referred to as S_{CB} .
- if the blade is supercavitating, the upper and lower sides of the supercavity downstream of the blade trailing edge are collapsed to a single surface. The two sides of the collapsed cavity surface coincide with the two sides of the zero-thickness trailing wake sheet (see discussion below). This surface will be referred to as $S_{CW}(t)$.

A sketch of the approximate boundary is shown in Figure 2-3. The geometry of the wake, $S_W(t)$ is assumed to be invariant in time and is taken to be the same as the steady-flow relaxed wake corresponding to the circumferentially averaged inflow [18]. The approximate flow boundary therefore coincides with that of the fully wetted solution, as described by Hsin [22].

As a result of the linearization of the part of the supercavity downstream of the blade trailing edge, the surface $S_{CW}(t)$ may be considered to be a force-free surface. The pressure across the collapsed cavity surface must therefore be continuous and equal to the cavity pressure p_c . The pressure across the blade wake surface must also

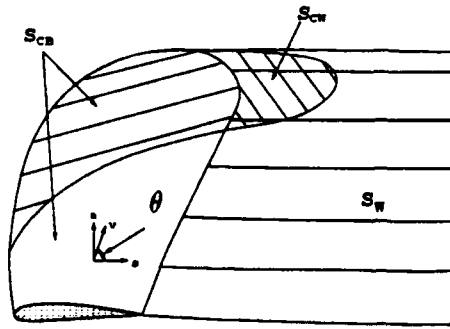


Figure 2-3: The approximate cavity surface on which the boundary conditions are applied.

be continuous. Therefore, it is possible to consider these two surfaces to coincide, with the condition of pressure continuity being

$$\begin{aligned} p^+ &= p^- = p_c \quad \text{on } S_{cw}(t) \\ p^+ &= p^- = p \quad \text{on } S_w(t). \end{aligned} \quad (2.5)$$

As mentioned in Chapter 1, satisfying the boundary conditions on the approximate boundary serves as the first iteration in a fully nonlinear solution. In the fully nonlinear solution, subsequent iterations are found by satisfying the dynamic boundary condition on an updated cavity surface (the kinematic boundary condition is used to update the surface, as described in section 2.4). The solution is then considered converged when the cavity surface does not change (to within a tolerance) between two consecutive iterations. It was also mentioned in Chapter 1 that, using the present potential based panel method, the first iteration solution (where Green's formula is satisfied on the approximate boundary) is *extremely close to the converged nonlinear solution* for a wide range of operating conditions. As a result, it is deemed unnecessary to go beyond the first iteration towards the fully nonlinear solution. In view of the high computational cost involved in regriding and re-computing influence coefficients, the importance of this conclusion cannot be overstated.

There is a simple recurring theme throughout this thesis: *avoid recomputing influence coefficients*. In fact, the struggle to avoid computing additional influence coefficients is the driving force behind many of the numerical techniques to be introduced in this thesis. In the fully wetted steady flow solution, the computation of influence coefficients dominates the computation time. The solution of the unsteady cavitating propeller will be found in the time domain, with the fully wetted solution serving as the initial condition. A significant amount of computation is avoided by using the same influence coefficients in both the fully wetted and cavitating solutions. A computationally efficient solution is made feasible by the accuracy of the first iteration.

Green's formula (2.4) holds on the exact flow boundary. It does not, however, apply on the upper surface of the wake, which is part of the approximate boundary. Care must be taken in extracting the correct local contribution when the field point lies on the wake surface.

Considering the approximate boundary, the first integral on the right-hand-side of (2.4) may be decomposed into integrals over the blade surface and the portion of the wake which is overlapped by the cavity (previously denoted S_{CB} and S_{CW} , respectively, in Figure 2-3). The exact form of Green's formula depends on the location of the field point, which will either be on S_{CB} or on S_{CW} . Each case will be considered separately.

Field Point on S_{CB}

If the field point is on the blade surface S_{CB} , the local contribution is extracted from the first integral in (2.4) and Green's formula becomes

$$2\pi\phi(t) = \int_{S_{CB}} \left[\phi_q(t) \frac{\partial G(p; q)}{\partial n_q} - G(p; q) \frac{\partial \phi_q(t)}{\partial n_q} \right] dS - \\ - \int_{S_{CW}(t)} G(p; q) \left(\frac{\partial \phi_q^+}{\partial n_q}(t) - \frac{\partial \phi_q^-}{\partial n_q}(t) \right) dS +$$

$$+ \int_{S_{CW} \cup S_W} (\Delta\phi_w(r, \theta, t)) \frac{\partial G(p; q)}{\partial n_q} dS \quad (2.6)$$

where the superscripts + and - correspond to the upper and lower sides of the wake surface, respectively. Note that the wake surface has been divided into S_{CW} and S_W , as shown in Figure 2-3.

The velocity normal to S_{CW} is discontinuous across the surface. The jump in $\frac{\partial\phi}{\partial n}$ defines a source distribution, of density $q_w(t)$, which represents the cavity thickness:

$$q_w(t) \stackrel{\text{def}}{=} \frac{\partial\phi_q^+}{\partial n_q}(t) - \frac{\partial\phi_q^-}{\partial n_q}(t). \quad (2.7)$$

The potential is also discontinuous across the S_W , where the jump $\Delta\phi_w(r, \theta, t)$ is related to the local circulation history. This is described in section 4.4.

Inserting (2.7) into (2.6) yields:

$$\begin{aligned} 2\pi\phi(t) = & \int_{S_{CB}} \left[\phi_q(t) \frac{\partial G(p; q)}{\partial n_q} - G(p; q) \frac{\partial\phi_q}{\partial n_q}(t) \right] dS - \\ & - \int_{S_{CW}(t)} q_w(t) G(p; q) dS + \int_{S_{CW} \cup S_W} \Delta\phi_w(r, \theta, t) \frac{\partial G(p; q)}{\partial n_q} dS \quad \text{on } S_{CB}. \end{aligned} \quad (2.8)$$

Field Point on S_{CW}

Consider the case where the field point is on the upper side of the collapsed cavity surface in the wake, $S_{CW}(t)$. In this case, local contribution must be extracted from the integral over $S_W(t)$ on the right hand side of (2.4), which reduces to

$$\begin{aligned} 2\pi[\phi^+(t) + \phi^-(t)] = & \int_{S_{CB}} \left[\phi_q(t) \frac{\partial G(p; q)}{\partial n_q} - G(p; q) \frac{\partial\phi_q}{\partial n_q}(t) \right] dS - \\ & - \int_{S_{CW}(t)} q_w(t) G(p; q) dS + \int_{S_{CW} \cup S_W} \Delta\phi_w(r, \theta, t) \frac{\partial G(p; q)}{\partial n_q} dS \quad \text{on } S_{CW}. \end{aligned} \quad (2.9)$$

Derivation of this result is provided in Appendix A.

The left hand side of (2.9) may be written in terms of the potential on one side of the wake sheet and the potential jump across the sheet, $\phi^+(t) + \phi^-(t) = 2\phi^+(t) - \Delta\phi_w(r, \theta, t)$. Inserting this into (2.9) results in an expression for the potential ϕ^+ :

$$4\pi\phi^+(t) = 2\pi\Delta\phi_w(r, \theta, t) + \int_{S_{CB}} \left[\phi_q(t) \frac{\partial G(p; q)}{\partial n_q} - G(p; q) \frac{\partial \phi_q(t)}{\partial n_q} \right] dS -$$

$$- \int_{S_{CW}(t)} q_w(t) G(p; q) dS + \int_{S_{CW} \cup S_W} \Delta\phi_w(r, \theta, t) \frac{\partial G(p; q)}{\partial n_q} dS \quad \text{on } S_{CW}. \quad (2.10)$$

Equations (2.8) and (2.10) define the potential $\phi(t)$ on the blade surface beneath the cavity, S_{CB} , and the potential $\phi^+(t)$ on the wake sheet, $S_{CW}(t)$, in terms of the following distributions of singularities:

- continuous source and normal dipole distributions on S_{CB} of strength $\frac{\partial \phi_q}{\partial n_q}(t)$ and $\phi(t)$, respectively
- a source distribution on $S_{CW}(t)$ of strength $q_w(t)$
- a normal dipole distribution on the entire wake sheet $S_{CW} \cup S_W$ of strength $\Delta\phi_w(r, \theta, t)$.

On the wake sheet $S_{CW} \cup S_W$ the dipole strength $\Delta\phi_w(r, \theta, t)$ is convected along the assumed wake surface with angular speed ω , in order to ensure that the pressure jump in the wake is equal to zero:

$$\Delta\phi_w(r, \theta, t) = \Delta\phi_T \left(r, t - \frac{\theta - \theta_T(r)}{\omega} \right);$$

$$t \geq \frac{\theta - \theta_T(r)}{\omega}$$

$$\Delta\phi_w(r, \theta, t) = \Delta\phi_w^{fw} \left(r, t - \frac{\theta - \theta_T(r)}{\omega} \right); \quad t < \frac{\theta - \theta_T(r)}{\omega} \quad (2.11)$$

where r, θ are the cylindrical coordinates of the wake surface and $\theta_T(r)$ is the θ coordinate of the blade trailing edge at radius r . $\Delta\phi_w^{fw}(r)$ is the unsteady fully wetted flow potential jump in the wake. $\Delta\phi_w^{fw}(r)$ will be considered known; the unsteady fully wetted flow solution will be found before the unsteady cavity solution (see section 4.4).

Note that the wake convection given by (2.11) is identical to the fully wetted convection [39]. This is allowed by the linearization of the supercavity in the wake, where the two force-free surfaces are considered as one (see equation (2.5)).

Everywhere on S_{CB} and $S_{CW}(t)$, either the source distribution is known (a *Neumann* boundary condition) or the dipole distribution is known (a *Dirichlet* boundary condition). Green's formulae (2.8) and (2.10) may then be discretized and rewritten as a linear system of equations by employing the boundary conditions and shifting all of the known quantities to the right-hand-side. This will be described in detail in Chapters 3 and 4, following the derivation of the boundary conditions in sections 2.3 and 2.4.

2.3 The Dynamic Boundary Condition

The dynamic boundary condition (DBC) requires that the pressure everywhere inside and on the cavity be constant and equal to the known cavity pressure, p_c . Bernoulli's equation with respect to the propeller fixed system is

$$\frac{p_o}{\rho} + \frac{1}{2}|U_w|^2 = \frac{\partial\phi}{\partial t} + \frac{p_c}{\rho} + \frac{1}{2}|q_t|^2 - \frac{1}{2}\omega^2 r^2 + g y_s. \quad (2.12)$$

where ρ is the fluid density and r is the distance from the axis of rotation. Here q_t is the total velocity on the cavity surface. p_o is the pressure far upstream on the shaft axis; g is the gravitational constant and y_s is the vertical distance from the horizontal plane through the axis of rotation, as shown in Figure 2-1. y_s is defined as negative in the direction of gravity.

After some manipulation, and using the definition of the cavitation number:

$$\sigma_n \stackrel{\text{def}}{=} \frac{P_o - P_c}{\frac{\rho}{2} n^2 D^2}, \quad (2.13)$$

where $n = \frac{\omega}{2\pi}$ and D are the propeller revolutions per unit time and diameter, respectively, we find that the magnitude of the total cavity velocity satisfies

$$|q_t|^2 = n^2 D^2 \sigma_n [1 - f(s)] + |U_w|^2 + \omega^2 r^2 - 2gy_s - 2\frac{\partial\phi}{\partial t}. \quad (2.14)$$

The function $f(s)$ corresponds to a pressure recovery law at the trailing edge of the cavity along the arc s on the surface of each spanwise blade section. The pressure recovery is given by an algebraic expression over a specified portion of the cavity near its trailing edge. This termination model is described in detail in Appendix C.

Since the cavity boundary consists of two parts — one coinciding with a portion of the blade surface and the other with a portion of the wake surface — the application of the dynamic boundary condition on each will be considered separately.

DBC on the Cavitating Part of the Blade

In addition to the expression (2.14), the cavity velocity q_t may also be expressed in terms of the directional derivatives of the perturbation potential and the components of the inflow along the same curvilinear coordinates [30]. The coordinate system² on the cavity surface consists of s (chordwise) and v (spanwise), as shown in Figure 2-3:

$$q_t = \frac{(\frac{\partial\phi}{\partial s} + U_s)[\hat{s} - (\hat{s} \cdot \hat{v})\hat{v}] + (\frac{\partial\phi}{\partial v} + U_v)[\hat{v} - (\hat{s} \cdot \hat{v})\hat{s}]}{\|\hat{s} \times \hat{v}\|^2} + \left(\frac{\partial\phi}{\partial n} + U_n\right) \hat{n} \quad (2.15)$$

with \hat{s} and \hat{v} being the unit vectors corresponding to the coordinates s and v , respectively, and with \hat{n} being the unit normal vector to the assumed cavity. U_s , U_v , and U_n are the s , v and n components of the relative inflow, U_{in} .

If s , v and n were located on the correct cavity surface, then the normal velocity, $\frac{\partial\phi}{\partial n} + U_n$, would vanish. However, this is not the case since the cavity curvilinear coordinates are approximated with those on the propeller surface. Nevertheless, in

²In general non-orthogonal.

applying the dynamic boundary condition, the normal velocity is assumed to be vanishingly small. In the fully nonlinear scheme, the normal velocity vanishes as the solution converges. As shown in Chapter 5 and in Appendix B (for two dimensional flows), it is found that leaving the normal velocity term out of the dynamic boundary condition has only a small effect on the solution.

Equations (2.14) and (2.15) may then be combined to form an equation which is quadratic in the unknown chordwise perturbation velocity, $\frac{\partial \phi}{\partial s}$. The two solutions to the quadratic equation represent potential gradients which are positive and negative in the direction of *increasing* s . The positive root is chosen to ensure that the cavity velocity points in the direction of increasing s . We can now express $\frac{\partial \phi}{\partial s}$ in terms of the cavitation number, the inflow velocity, and the *unknown* derivatives $\frac{\partial \phi}{\partial v}$ and $\frac{\partial \phi}{\partial t}$:

$$\begin{aligned} \frac{\partial \phi}{\partial s}(s, v, t) = & -U_\infty + \left(\frac{\partial \phi}{\partial v} + U_v \right) \cos \theta + \\ & + \sin \theta \sqrt{n^2 D^2 \sigma_n [1 - f(s)] + |U_W|^2 + \omega^2 r^2 - 2gy_s - 2\frac{\partial \phi}{\partial t} - \left(\frac{\partial \phi}{\partial v} + U_v \right)^2} \end{aligned} \quad (2.16)$$

with θ being the angle between s and v , as shown in Figure 2-3. Equation (2.16) is integrated once to form a Dirichlet boundary condition on ϕ :

$$\begin{aligned} \phi(s, v, t) = & \phi(0, v, t) + \int_0^s \left[-U_\infty + \left(\frac{\partial \phi}{\partial v} + U_v \right) \cos \theta + \right. \\ & + \sin \theta \sqrt{n^2 D^2 \sigma_n [1 - f(s)] + |U_W|^2 + \omega^2 r^2 - 2gy_s - 2\frac{\partial \phi}{\partial t} - \left(\frac{\partial \phi}{\partial v} + U_v \right)^2} \left. \right] ds \end{aligned} \quad (2.17)$$

The integral on the right-hand-side of (2.17) is determined by trapezoidal quadrature, as described in section 3.3. Since (2.17) defines the strength of the dipole distribution on the cavity, it may be directly substituted into Green's formula 2.8.

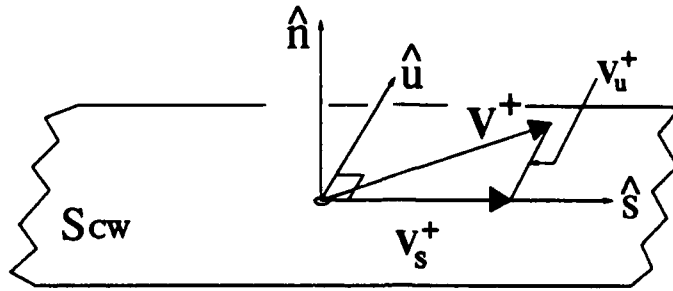


Figure 2-4: Velocity diagram on the wake surface.

According to the dynamic boundary condition (2.17), ϕ depends on both its spanwise and time derivatives. These terms will be treated as knowns and will be updated in a time-stepping scheme which will be discussed later. The influence of the crossflow term $\frac{\partial \phi}{\partial v}$ was studied first for the case of partially cavitating 3-D hydrofoils and it was found that the global dependence of the solution on the crossflow term was small. This result will be shown in section 4.2.4, where it will also be demonstrated for the propeller solution. The convergence of the time-derivative with iterations, as well as its effect on the solution, will be discussed in section 4.4.

DBC on the Cavitating Part of the Wake

The dynamic boundary condition on the cavitating portion of the wake, S_{cw} , may also be written as a Dirichlet condition on ϕ^+ . In this case, consider the orthogonal system (s, u, n) , shown in Figure 2-4. Assuming that s is the direction of the mean velocity, the total velocity on the upper side of the wake sheet may be written

$$\mathbf{V}^+ = V_s^+ \hat{s} + V_u^+ \hat{u} + V_n^+ \hat{n}.$$

The normal velocity V_n^+ will be omitted from the dynamic boundary condition, as it was from (2-4), with the same justification.

Applying Bernoulli's equation, which is used to define the total velocity on the

cavity q_t , we have

$$V_s^+ = \sqrt{|q_t|^2 - (V_u^+)^2}. \quad (2.18)$$

The dynamic boundary condition on S_{CW} may thus be written

$$\frac{\partial \phi^+}{\partial s} = -U_s + \sqrt{n^2 D^2 \sigma_n [1 - f(s)] + |U_W|^2 + \omega^2 r^2 - 2gy_s - 2\frac{\partial \phi}{\partial t} - (V_u^+)^2}. \quad (2.19)$$

where we have substituted the expression for $|q_t|$ given by (2.14). Equation (2.19) may be integrated once to form a Dirichlet boundary condition on the potential on the upper wake surface, ϕ^+ :

$$\phi^+(s, u, t) = \phi(0, v, t) + \int_{s_{TB}}^s \left[-U_s + \sqrt{n^2 D^2 \sigma_n [1 - f(s)] + |U_W|^2 + \omega^2 r^2 - 2gy_s - 2\frac{\partial \phi}{\partial t} - (V_u^+)^2} \right] ds. \quad (2.20)$$

The integral in (2.20) is also computed by trapezoidal quadrature. Equation (2.20) defines the potential ϕ^+ on the upper side of the wake and may be directly substituted into Green's formula (2.10).

As with the dynamic boundary condition on the cavitating part of the blade, the influence of the crossflow term, V_u^+ , was found to be small. This will be demonstrated in section 4.2.4.

2.4 The Kinematic Boundary Condition

The kinematic boundary condition, which is used to determine the position of the actual cavity surface once the singularity strengths are known, is derived in this section. As in the previous section, the cavity boundary will be divided into two zones which will be considered separately.

KBC on the Cavitating Part of the Blade

The kinematic boundary condition on the cavity is the requirement that the sub-

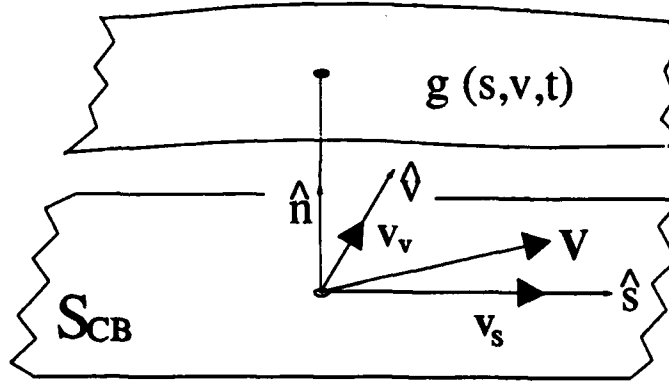


Figure 2-5: Definition of the cavity surface defined with respect to the blade surface.

stantial derivative of the cavity surface vanishes.

$$\frac{D}{Dt} [n - h(s, v, t)] = \left(\frac{\partial}{\partial t} + \mathbf{q}_t \cdot \nabla \right) [n - h(s, v, t)] = 0 \quad (2.21)$$

where n is the coordinate normal to the blade surface (with unit vector \hat{n}) and $h(s, v, t)$ is the thickness of the cavity normal to the blade at the point (s, v) at time t . Expressing the gradient in terms of the local directional derivatives

$$\nabla = \frac{[\hat{s} - (\hat{s} \cdot \hat{v})\hat{v}] \frac{\partial}{\partial s} + [\hat{v} - (\hat{s} \cdot \hat{v})\hat{s}] \frac{\partial}{\partial v}}{\|\hat{s} \times \hat{v}\|^2} + \hat{n} \frac{\partial}{\partial n}, \quad (2.22)$$

performing the dot product with \mathbf{q}_t (as defined in (2.15)) and substituting the result in (2.21) yields the following partial differential equation for the cavity thickness:

$$\frac{\partial h}{\partial s} [V_s - \cos \theta V_v] + \frac{\partial h}{\partial v} [V_v - \cos \theta V_s] = \sin^2 \theta (V_n - \frac{\partial h}{\partial t}) \quad (2.23)$$

where

$$V_s \stackrel{\text{def}}{=} \frac{\partial \phi}{\partial s} + U_s, \quad V_v \stackrel{\text{def}}{=} \frac{\partial \phi}{\partial v} + U_v, \quad V_n \stackrel{\text{def}}{=} \frac{\partial \phi}{\partial n} + U_n.$$

KBC on the Cavitating Part of the Wake

The kinematic boundary condition on the cavity surface in the wake may be derived in a similar fashion, except that now both surfaces of the supercavity must

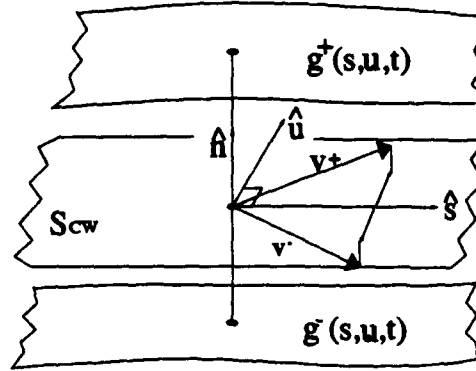


Figure 2-6: Definition of the cavity surface defined with respect to the wake surface.

be considered

$$\begin{aligned} \frac{D}{Dt} (n - g^+(s, u, t)) &= \left[\frac{\partial}{\partial t} + \mathbf{V}^+ \cdot \nabla \right] (n - g^+(s, u, t)) = 0 \\ \frac{D}{Dt} (n - g^-(s, u, t)) &= \left[\frac{\partial}{\partial t} + \mathbf{V}^- \cdot \nabla \right] (n - g^-(s, u, t)) = 0 \end{aligned} \quad (2.24)$$

where $g^\pm(s, u, t)$ defines the upper and lower cavity surfaces, as shown in Figure 2-6. Note that (s, u, n) is an orthogonal system. \mathbf{V}^+ and \mathbf{V}^- are the total velocities on the upper and lower sides of the wake (also shown in Figure 2-6), respectively, and may be written

$$\mathbf{V}^\pm = V_s^\pm \hat{s} + V_u^\pm \hat{u} + V_n^\pm \hat{n} \quad (2.25)$$

The upper and lower cavity surfaces, $g(s, u, t)^\pm$, may be written

$$g(s, u, t)^\pm = C(s, u, t) \pm \frac{1}{2} h_w(s, u, t),$$

where C is the cavity camber in the wake and h_w is the cavity thickness. The quantities g , C and h_w are all taken along the normal to the trailing wake surface. These quantities are also shown in Figure 2-7.

Expanding equations (2.24) we find that

$$V_n^+ - \left[\frac{\partial C}{\partial t} + \frac{1}{2} \frac{\partial h_w}{\partial t} \right] = V_s^+ \left[\frac{\partial C}{\partial s} + \frac{1}{2} \frac{\partial h_w}{\partial s} \right] + V_u^+ \left[\frac{\partial C}{\partial u} + \frac{1}{2} \frac{\partial h_w}{\partial u} \right]$$

$$V_n^- - \left[\frac{\partial C}{\partial t} - \frac{1}{2} \frac{\partial h_w}{\partial t} \right] = V_s^- \left[\frac{\partial C}{\partial s} - \frac{1}{2} \frac{\partial h_w}{\partial s} \right] + V_u^- \left[\frac{\partial C}{\partial u} - \frac{1}{2} \frac{\partial h_w}{\partial u} \right] \quad (2.26)$$

Taking the difference between the two equations in (2.26) and assuming that \hat{s} coincides with the direction of the mean velocity so that

$$V_s^+ = V_s^- \quad (2.27)$$

yields

$$q_w(t) - \frac{\partial h_w}{\partial t} = V_s^+ \frac{\partial h_w}{\partial s} + 2V_u^+ \frac{\partial C}{\partial u} \quad (2.28)$$

Here we have used the definition of the wake source strength (2.7) and following equalities:

$$V_u^+ = -V_u^- \quad \text{and} \quad V_n^+ = -V_n^- \quad (2.29)$$

which readily follow from the assumption (2.27) and the fact that the free vorticity must follow the mean velocity vector.

To be consistent with the dynamic boundary condition, we assume that the spanwise crossflow velocity is small. Applying equation (2.19), the kinematic boundary condition (2.28) reduces to

$$\frac{\partial h_w}{\partial s} \sqrt{n^2 D^2 \sigma_n [1 - f(s)] + |U_w|^2 + \omega^2 r^2 - 2gys - 2 \frac{\partial \phi}{\partial t}} = q_w(t) - \frac{\partial h_w}{\partial t}. \quad (2.30)$$

Note that the cavity height on the blade and in the wake, both shown in Figure 2-7, are defined differently and so are given separate symbols. The computation of h and h_w from (2.23) and (2.30) will be described in section 4.1.3.

The position of the cavity surface over the blade surface is determined by adding the cavity thickness h normal to the blade surface at the midspan of the panel boundaries. In the wake, the cavity camber $C(s, u, t)$ must first be determined. An expression for $C(s, u, t)$ may be found by adding the two equations (2.26) and dividing

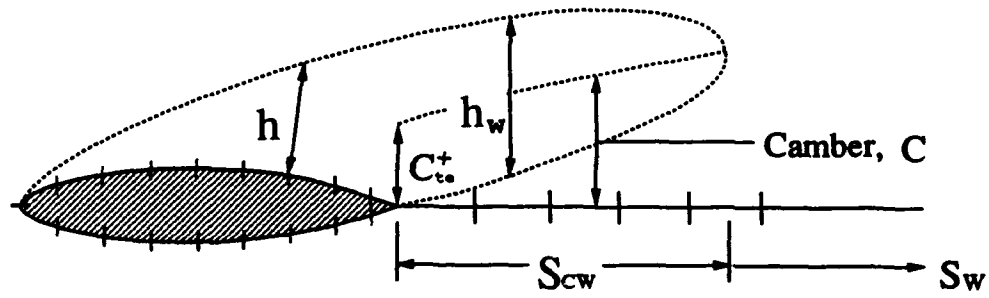


Figure 2-7: Definition of the cavity camber and height for a supercavitating section of the propeller blade.

through by two:

$$V_s^+ \frac{\partial C}{\partial s} = -\frac{\partial C}{\partial t} + U_n + \frac{1}{2} \left(\frac{\partial \phi^+}{\partial n} + \frac{\partial \phi^-}{\partial n} \right) - V_u^+ \frac{\partial h_w}{\partial u} \quad (2.31)$$

where U_n is the inflow velocity normal to the wake sheet. Equation (2.31) is numerically integrated to determine the camber surface in the wake. At the trailing edge of the blade, the continuity of camber and thickness is imposed:

$$\begin{aligned} C_{te}^+ &= \frac{1}{2} h_{wte}^- \\ h_{wte}^+ &= h_{wte}^- \end{aligned} \quad (2.32)$$

Here, the superscripts $+$ and $-$ denote just upstream and just downstream of the trailing edge, respectively. C_{te}^+ is the value of the camber just upstream of the trailing edge. It is determined by adding $\frac{h}{2}$ to the trailing edge along the blade normal (see Figure 2-7). The quantity h_{wte}^- is determined by interpolating the upper cavity surface over the blade at the trailing edge and computing its normal offset from the wake sheet. The upper and lower surfaces of the cavity in the wake are then determined by adding and subtracting half of the cavity thickness h_w from the camber surface. This defines the cavity surface at the midspans of all the spanwise strips. The surface of the cavity at the strip boundaries are determined by interpolation and extrapolation.

KBC on the Wetted Part of the Blade

The kinematic boundary condition on the wetted portion of the blade, S_{WS} , defines the source strength there in terms of the known inflow velocity:

$$\frac{\partial \phi_q}{\partial n_q}(t) = -U_{in}(x_q, y_q, z_q, t) \cdot \hat{n}_q; \quad q \in S_{WS}(t) \quad (2.33)$$

where x_q, y_q, z_q are the coordinates of the point q with respect to the propeller fixed system. As in the case of fully-wetted flow, this boundary condition may be directly substituted in Green's formula.

2.5 The Kutta Condition

The Kutta condition requires that the fluid velocity be finite at the blade trailing edge. It was found necessary, in the fully wetted steady flow propeller solution, to satisfy a nonlinear Kutta condition which ensures pressure equality between the suction and pressure sides at the trailing edge [47]. The so-called pressure Kutta condition was later refined by Kinnas and Hsin [38], who developed an efficient iterative solution. In the present work, an extension of Morino's steady Kutta condition is applied. Development of a pressure Kutta condition for the cavitating propeller is left for the future.

The value of the dipole strength, $\Delta\phi_T(r, t)$, at the blade trailing edge at time t is

$$\Delta\phi_T(r, t) = \phi_T^+(r, t) - \phi_T^-(r, t) = \Gamma(r, t) \quad (2.34)$$

where ϕ_T^+ and ϕ_T^- are the values of the potential at the blade trailing edge at radius r on the suction side and the pressure side, respectively. The potential jump there is also equal to the circulation Γ at time t around the blade section at radius r . This condition is equivalent to requiring the shed vorticity from the blade trailing edge to be proportional to the time rate of change of the circulation around the blade (Kelvin's law). An extension of Morino's Kutta condition for steady flow [52], in

which the potential jump at the trailing edge of the blade is simply replaced by the potential jump at the nearest control points, is applied. This is addressed in detail in section 4.4.

Chapter 3

Discrete Formulation

The greatest complexity of the cavity flow problem is the fact that the cavity extent (planform) is not known *a priori*; its computation, in fact, is a primary goal in the solution. Clearly, since the application of the boundary conditions relies on knowing the extent of the cavity, computing it will require some sort of iterative process of successive guesses. In this chapter, a brief introduction to the iterative procedure will be given, followed by a detailed description of the discretized integral equations and boundary conditions.

3.1 Solution Methodology

The local cavity length (defined as the arclength of the projection of the cavity on the nose-tail helix) is given at each radius r by the function $l(r, t)$. For a given cavitation number, σ_n , the cavity planform $l(r, t)$ will be determined from the requirement:

$$\delta(l(r, t), r; \sigma_n) \stackrel{\text{def}}{=} h(l(r, t), r, t) \text{ [or } h_w(l(r, t), r, t)] = 0. \quad (3.1)$$

Equation (3.1) requires that the cavity close at its trailing edge; this requirement will be used as the basis of an iterative solution to find the cavity planform.

The iterative method for finding the cavity length for given cavitation number evolved from the numerical solution of the *fixed-length two-dimensional* flow problem, in which the cavity length on a two-dimensional hydrofoil is assumed to be known

while the cavitation number is (an additional) unknown [35]. In that case, a cavity closure condition — requiring that the cavity close at its trailing edge — is imposed to provide the necessary additional equation. However, when solving the so-called “direct” problem, where the cavitation number is known and the cavity length is to be determined, there is one fewer unknown and thus the closure condition may be discarded. The resulting indeterminacy is then experienced in the following way: solving the boundary value problem for given cavitation number by guessing the extent of the cavity results in a cavity which does not close *unless the cavity length is the one which corresponds to the given cavitation number*. Put another way, for given cavitation number the correct cavity length is the one for which the cavity closes. This reveals the foundation of the algorithm for finding the correct cavity length: the solution is found for successive guesses of the cavity length until the solution finds a closed cavity¹. Note that the Newton-Raphson iterative method for root-finding is ideal for this application.

Figure 3-1 depicts the process of finding the correct cavity length for a partially cavitating 2-D hydrofoil. Shown are a succession of cavity solutions for a NACA16006 hydrofoil at an angle of attack $\alpha = 4^\circ$ corresponding to a succession of guesses of the cavity length. The cavitation number for all solutions is $\sigma = 1.097^2$. Notice that the cavity closes for the guess $l = 0.4$, as expected. Also shown in Figure 3-1 is the openness of the cavity at its trailing edge, δ , plotted against the cavity length, l . The solution of the direct problem amounts to finding the zero-crossing of this curve.

The iterative solution for the cavity extent may also be applied in three dimensions, where several difficulties are encountered. The most obvious difficulty is the need to determine the cavity length in both chordwise *and* spanwise directions. An additional challenge is the accurate prediction of the cavity planform *without regriding the blade surface for each iteration*³. Perhaps the most severe difficulty arises

¹An open cavity model is also very easily implemented with this method. Instead of requiring the cavity to close, the desired thickness of the cavity at its trailing edge may be specified.

²This cavitation number corresponds to the fixed-length solution for $l = 0.4$.

³The solution for each cavity length shown in Figure 3-1 was found by regriding the hydrofoil for each guess of the cavity length so that the cavity always ended at a panel boundary.

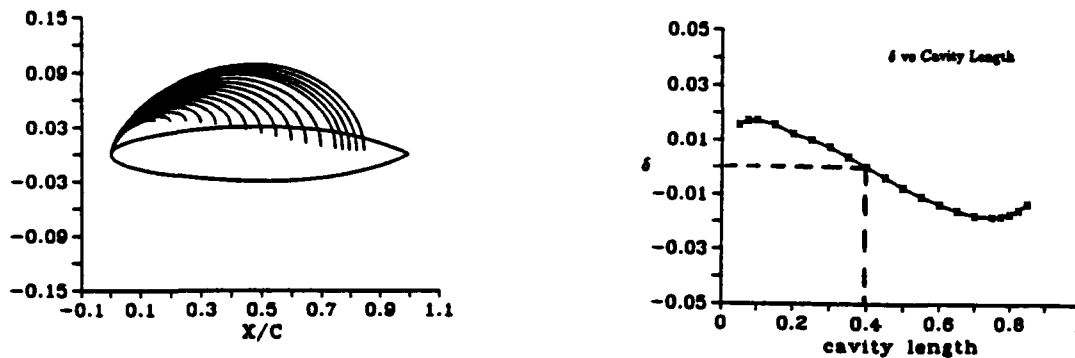


Figure 3-1: NACA16006 hydrofoil at $\alpha = 4^\circ$ and $\sigma = 1.097$ (corresponding to the correct length $l = 0.4$). Left plot shows the predicted cavity shapes for different guesses of l . Right plot shows the resulting behavior of δ vs l .

from the need to simultaneously treat the occurrence of both partial and supercavitation. Before providing answers to these difficulties, however, it is useful to describe the solution for a given guess of the cavity planform. In the following sections, I will describe in detail the numerical discretization of the boundary value problem which has been detailed in Chapter 2.

3.2 Discretized Green's Formula

The objective of the numerical analysis is to invert equations (2.8) and (2.10) subject to the kinematic boundary condition (2.33), the dynamic boundary conditions (2.17) and (2.19), and the Kutta condition. To accomplish this, we first tag one blade with the label *key blade*. The solution at a given time step will be obtained only for the key blade, with the influence of the other blades corresponding to an earlier solution of the key blade. This time stepping algorithm will be detailed in section 4.4. The key blade surface is discretized into N chordwise and M spanwise quadrilateral panels with the corners lying on the blade surface S_{CB} and with the control points located at the panel centroids. An example of a discretized blade is shown in Figure 3-2. The source and normal dipole distributions on each panel are approximated with constant strength distributions. The trailing wake is discretized into panels at constant angular intervals $\Delta\theta_w = \omega\Delta t$ with Δt being the time step. The blade and

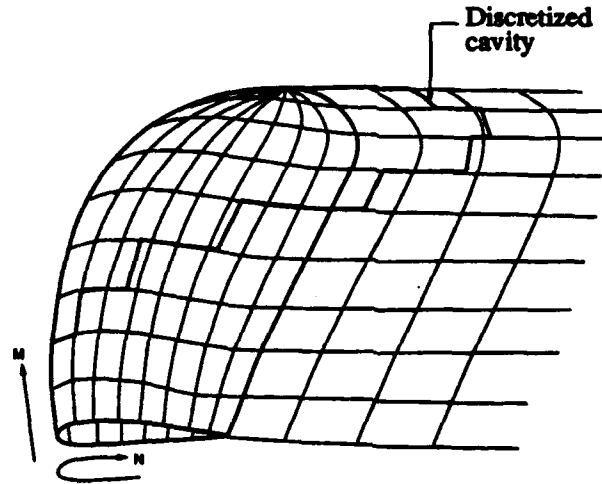


Figure 3-2: Discretization of the propeller blade, the cavity, and their trailing wakes; $N=16$, $M=9$.

trailing wake discretization is identical to that in the case of fully wetted unsteady flow [22, 39, 38]. If we call

N_{WS} = Number of wetted panels on the blade

N_{CB} = Number of cavitating panels on the blade

N_{CW} = Number of cavitating panels in the wake,

then, among the discrete sources and dipoles, we have

- N_{WS} known source strengths, via (2.33)
- N_{CB} known dipole strengths, via (2.17)
- N_{CW} known dipole strengths, via (2.20).

The following are then unknown and must be solved for:

- N_{WS} dipole strengths on the wetted blade surface.
- N_{CB} source strengths on the cavitating blade surface, and
- N_{CW} cavity source strengths in the supercavitating wake.

Prior to substituting the expressions for the known singularity strengths, the discretized Green's formulae (2.8) and (2.10) appear as follows:

$$\sum_{k=1}^{N_B} \sum_{m=1}^M \left\{ \sum_{n=1}^N \left[A_{inm}^k \phi_{nm}^k(\bar{n}) - B_{inm}^k \frac{\partial \phi^k}{\partial n_{nm}}(\bar{n}) \right] - \sum_{l=1}^{N_{C_m}} C_{ilm}^k Q_{nm}^k(\bar{n}) + \sum_{l=1}^{N_W} W_{ilm}^k \Delta \phi_{w_{lm}}^k(\bar{n}) \right\} = 0 \quad i = 1, \dots, N \times M \quad (3.2)$$

and

$$\begin{aligned} 4\pi\phi_i^k(\bar{n}) &= \\ &= \sum_{k=1}^{N_B} \sum_{m=1}^M \left\{ \sum_{n=1}^N \left[D_{inm}^k \phi_{nm}^k(\bar{n}) - E_{inm}^k \frac{\partial \phi^k}{\partial n_{nm}}(\bar{n}) \right] - \sum_{l=1}^{N_{C_m}} F_{ilm}^k Q_{lm}^k(\bar{n}) + \sum_{l=1}^{N_W} W_{ilm}^k \Delta \phi_{w_{lm}}^k(\bar{n}) \right\} \quad i = 1, \dots, N_{CW} \end{aligned} \quad (3.3)$$

where \bar{n} is the discrete time step, N_W is the number of panels on each strip of the wake, and N_{C_m} is the number of cavitating panels on each strip of the wake.

In equations (3.2) and (3.3), the indices i and j map quantities to panels. For example, $\phi_i(\bar{n})$ is the potential at the control point on the i^{th} panel at the \bar{n}^{th} time step. However, each panel may also be identified as the n^{th} panel on the m^{th} strip, so ϕ_i may also be written ϕ_{nm} . In what follows, these indexing alternatives will be used interchangeably to maximize compactness.

Note that the subscript q has been dropped from references to the discretized potential, ϕ_{nm} , and the source strength, $\frac{\partial \phi}{\partial n_{nm}}$, since these quantities are defined at the control points which are by definition variable points in the integration. For the remainder of this section, all of the flow variables will be assumed to be defined at the current time step and \bar{n} will be dropped from the equations.

A_{inm}^k and B_{inm}^k are the potentials induced at the i^{th} control point on the key blade by a unit strength dipole and a unit strength source at the n^{th} panel on the m^{th} strip of the k^{th} blade ($k = 1$ refers to the key blade). When the i^{th} control point lies on

the n^{th} panel on the m^{th} strip of the key blade, then

$$A_{inm}^1 = 2\pi \quad \text{for } i \longleftrightarrow (n, m).$$

C_{inm}^k is the potential induced at the i^{th} panel on the key blade due to a unit strength source at the n^{th} panel on the m^{th} strip of the wake of the k^{th} blade. W_{iml}^k is the potential induced at the i^{th} control point on the key blade by a unit strength dipole at the l^{th} panel of the m^{th} strip of the wake of the k^{th} blade. Similarly, D_{inm}^k and E_{inm}^k are the potentials induced at the i^{th} wake control point by a unit strength dipole and a unit strength source at the n^{th} panel of the m^{th} strip of the k^{th} blade. F_{inm}^k is the potential induced at the i^{th} wake control point due to a unit strength source at the n^{th} wake panel on the m^{th} wake strip of the k^{th} blade. W_{iml}^{*k} is the potential induced at the i^{th} wake panel by a unit strength dipole lying on the m^{th} strip of the wake of the k^{th} blade, where

$$W_{inm}^{*1} = 2\pi \quad \text{for } i \longleftrightarrow (n, m).$$

The shape of the surface bounded by the edges of each quadrilateral panel is approximated by a hyperboloidal surface, and the corresponding influence coefficients are determined analytically. The need for hyperboloidal panels was found to be necessary for the convergence and consistency of the steady flow propeller solution, especially when applied to extreme geometries [38, 53, 21]. Discussion of the computation of these influence coefficients may be found in [55] and [22].

Equations (3.2) and (3.3) may be rewritten to reflect the fact that at any given time step only the potentials on the key blade are unknown, while the rest are assumed to be known. Equation (3.2) becomes

$$\sum_{m=1}^M \left\{ \sum_{n=1}^N \left[A_{inm} \phi_{nm} - B_{inm} \frac{\partial \phi}{\partial n_{nm}} \right] - \sum_{n=1}^{N_{cm}} C_{inm} Q_{nm} + W_{iml} \Delta \phi_{w_{lm}} \right\} = \{ \text{RHS} \}_{S_{CBi}} \\ i = 1, \dots, N \times M \quad (3.4)$$

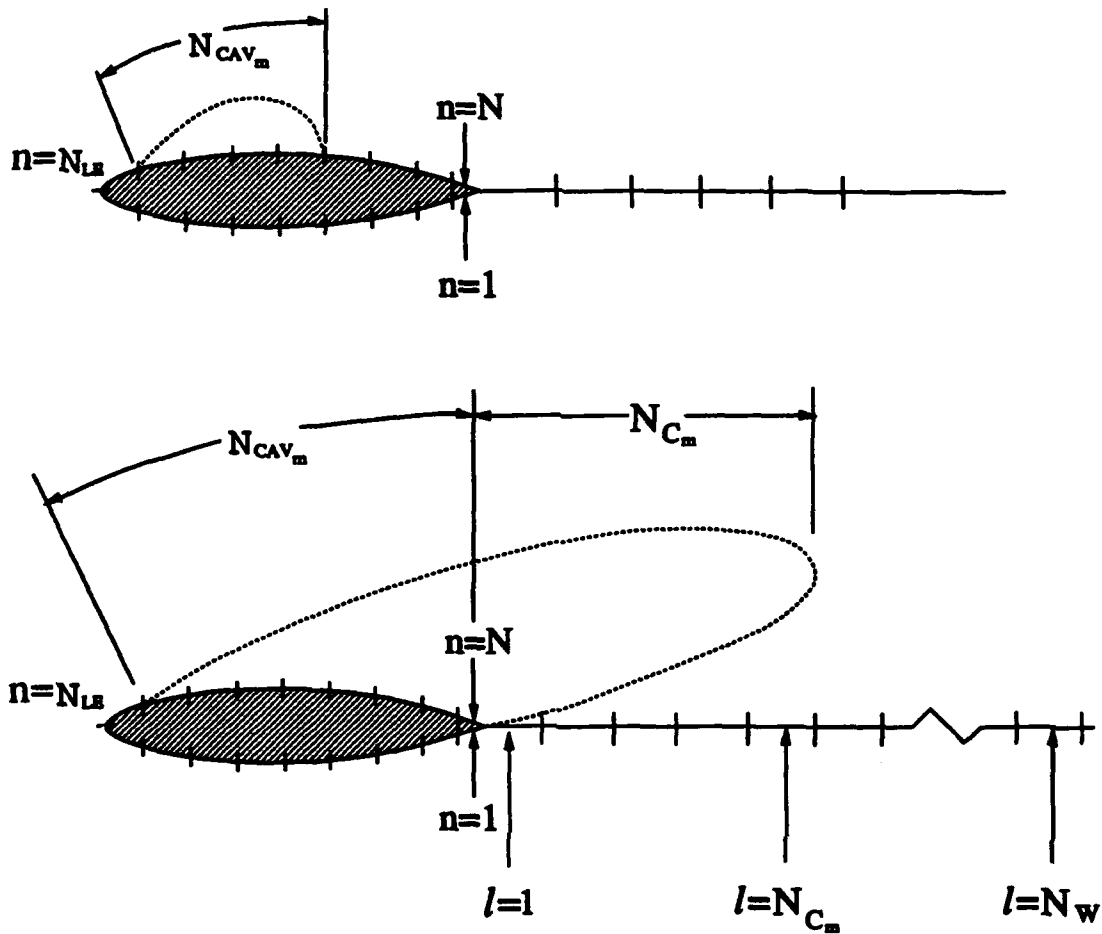


Figure 3-3: Indexing system for the discrete equations.

is

$$\frac{\partial \phi}{\partial n_{jm}} = -U_{in_{nm}} \cdot \hat{n}_{nm} \cdot \quad \begin{array}{l} n = 1, \dots, N_{LE}; N_{LE} + N_{CAV_m}, \dots, N \\ m = 1, \dots, M \end{array} \quad (3.8)$$

where $U_{in_{nm}}$ is the inflow velocity at the current time step, defined at the n^{th} control point on the m^{th} spanwise strip of the blade. The system of indexing is shown in Figure 3-3.

A single discrete equation may be written to replace the dynamic boundary con-

and (3.3) becomes

$$\begin{aligned} \sum_{m=1}^M \left\{ \sum_{n=1}^N \left[D_{inm} \phi_{nm} - E_{inm} \frac{\partial \phi}{\partial n_{nm}} \right] - \sum_{n=1}^{N_{Cm}} F_{inm} Q_{nm} + W_{i1m}^* \Delta \phi_{w_{1m}} \right\} = \\ = 4\pi \phi_i + \left\{ \text{RHS} \right\}_{S_{CW_i}} \quad i = 1, \dots, N_{CW} \end{aligned} \quad (3.5)$$

where

$$\begin{aligned} \left\{ \text{RHS} \right\}_{S_{CB_i}} = \\ = - \sum_{k=2}^{N_B} \left\{ \sum_{m=1}^M \sum_{n=1}^N \left[A_{inm}^k \phi_{nm}^k - B_{inm}^k \frac{\partial \phi^k}{\partial n_{nm}} \right] - \sum_{n=1}^{N_{Cm}} C_{inm}^k Q_{nm}^k + \sum_{l=2}^{N_W} W_{iml}^k \Delta \phi_{w_{lm}}^k \right\} \end{aligned} \quad (3.6)$$

and

$$\begin{aligned} \left\{ \text{RHS} \right\}_{S_{CW_i}} = \\ - \sum_{k=2}^{N_B} \left\{ \sum_{m=1}^M \sum_{n=1}^N \left[D_{inm}^k \phi_{nm}^k - E_{inm}^k \frac{\partial \phi^k}{\partial n_{nm}} \right] - \sum_{n=1}^{N_{Cm}} F_{inm}^k Q_{nm}^k + \sum_{l=2}^{N_W} W_{iml}^{*k} \Delta \phi_{w_{lm}}^k \right\}. \end{aligned} \quad (3.7)$$

In (3.4) and (3.5) the superscript $k = 1$ is implied. In (3.6) and (3.7) the potential ϕ_{nm}^k is equal to ϕ_{nm}^1 taken from the key blade solution at a previous time step, corresponding to the current location of blade k . The same equivalence is true for the source strengths $\frac{\partial \phi^k}{\partial n_{nm}}$ and Q_{nm}^k and the wake dipole strengths $\Delta \phi_{w_{lm}}^k$.

3.3 Discretized Boundary Conditions

The boundary conditions may now be discretized and incorporated in Green's formulae (3.4) and (3.5).

The discretized version of the kinematic boundary condition on the blade (2.33)

ditions on the blade (2.17) and in the wake (2.20)

$$\begin{aligned} \phi_{(N_{LB}+n)m} &= \phi_{0m} + \Psi_{nm} & n &= 1, \dots, N_{CAV_m} + N_{C_m} \\ & & m &= 1, \dots, M \end{aligned} \quad (3.9)$$

where

$$\Psi_{nm} \stackrel{\text{def}}{=} \begin{cases} \int_0^{s_{nm}} \left[\frac{\partial \phi}{\partial s} \text{ from (2.16)} \right] ds & n = 1, \dots, N_{CAV_m} \\ \int_0^{s_{TE_m}} \left[\frac{\partial \phi}{\partial s} \text{ from (2.16)} \right] ds + \int_{s_{TE_m}}^{s_{nm}} \left[\frac{\partial \phi}{\partial s} \text{ from (2.19)} \right] ds & n = N_{CAV_m} + 1, \dots, N_{CAV_m} + N_{C_m} \end{cases} \quad (3.10)$$

$$m = 1, \dots, M$$

and s_{TE_m} is the value of s at the trailing edge of the blade on the m^{th} spanwise strip, as shown in Figure 3-4. The integrals in equation (3.10) are computed by trapezoidal quadrature. The values of the integrands are computed at the control points and at the leading edge of cavity, where $s = 0$. The arclength between two consecutive control points is approximated by the sum of the linear distances between the control points and the panel edges (see Figure 3-4)

$$s_{nm} = \frac{1}{2} \Delta s_{1m} + \sum_{j=1}^{n-1} \frac{1}{2} (\Delta s_{jm} + \Delta s_{(j+1)m})$$

The quantity ϕ_0 in (3.9) is the perturbation potential at the detachment point of the cavity. It is also an unknown. This term is expressed as a cubic extrapolation in terms of the unknown potentials on the wetted panels on the same strip adjacent to the cavity detachment. This is shown schematically in Figure 3-5.

Locally, the potential is assumed to fit a 3rd-order polynomial in arc-length of the form

$$\phi(\bar{s}) \simeq A\bar{s}^3 + B\bar{s}^2 + C\bar{s} + D \quad (3.11)$$

where the coefficients A, B, C, D may be written in terms of the local unknown po-

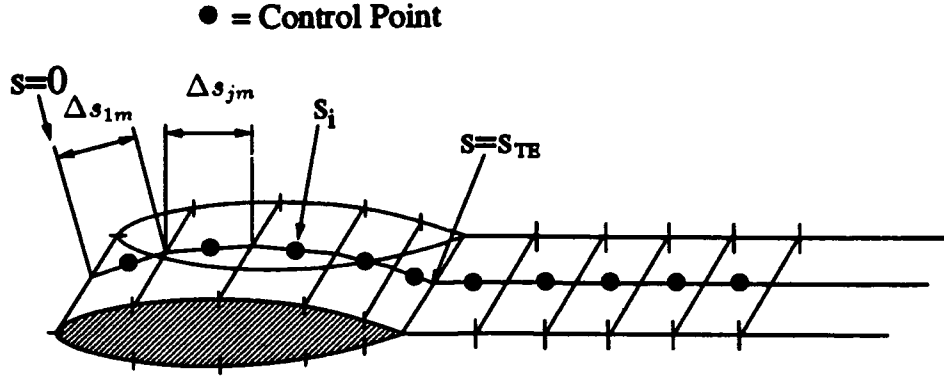


Figure 3-4: Definition of the arclength on a spanwise strip, used in the trapezoidal integration of $\frac{\partial \phi}{\partial s}$.

tentials and the cavity velocity by applying the following boundary conditions (see Figure 3-5):

- $\phi(\bar{s} = 0) \stackrel{\text{def}}{=} \phi_{3m}$
- $\phi(\bar{s} = \bar{s}_2) \stackrel{\text{def}}{=} \phi_{2m}$
- $\phi(\bar{s} = \bar{s}_1) \stackrel{\text{def}}{=} \phi_{1m}$
- $\frac{\partial \phi}{\partial \bar{s}}(\bar{s} = \bar{s}_0) = q_{0m} \stackrel{\text{def}}{=} \frac{\partial \phi}{\partial s}$ at the cavity leading edge (from 2.16).

Solving for the coefficients in (3.11) in terms of these quantities yields the following definition of ϕ_{0m} :

$$\phi_{0m} = R_{1m}\phi_{1m} + R_{2m}\phi_{2m} + R_{3m}\phi_{3m} + R_{4m}q_{0m} \quad (3.12)$$

where R_{1m}, \dots, R_{4m} are rational functions of \bar{s}_0, \bar{s}_1 , and \bar{s}_2 :

$$\begin{aligned} R_{1m} &= \frac{\bar{s}_0^2}{r_1} [1 - 2\bar{s}_0 t_1] \\ R_{2m} &= -\frac{\bar{s}_0^2}{r_1} [2\bar{s}_0 r_1 t_2 - 2\bar{s}_0 t_1 r_2 + r_2] \\ R_{3m} &= 1 + \frac{\bar{s}_0^2}{r_1} [2r_1 t_2 \bar{s}_0 + 2t_1 \bar{s}_0 (1 - r_2) + r_2 - 1] \\ R_{4m} &= 2\bar{s}_0^3 \left[\frac{t_1}{r_1} (\bar{s}_1 - \bar{s}_2 r_2) + \bar{s}_2 t_2 \right] - \frac{\bar{s}_0^2}{r_1} (\bar{s}_1 - \bar{s}_2 r_2) + \bar{s}_0 \end{aligned}$$

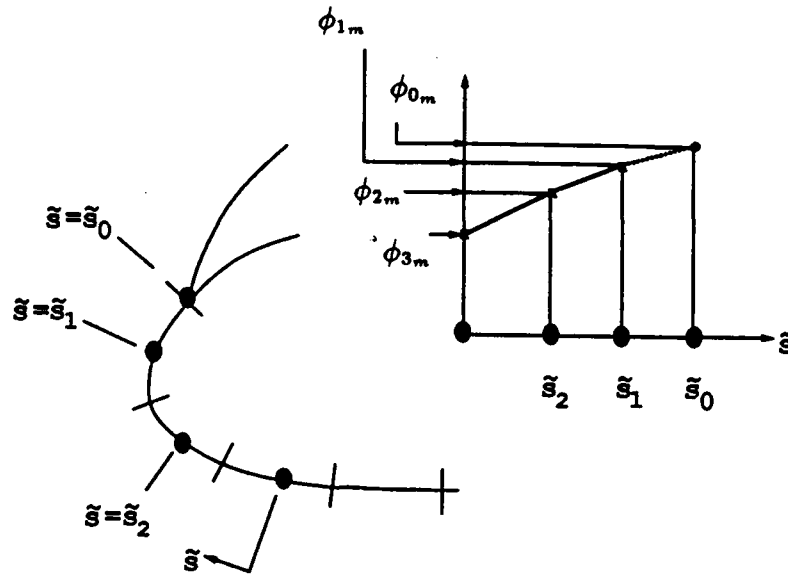


Figure 3-5: Schematic representation of the treatment of ϕ_0 .

where

$$r_1 = \tilde{s}_2 r_2 (\tilde{s}_2 - 2\tilde{s}_0) - \tilde{s}_1^2 + 2\tilde{s}_0 \tilde{s}_1$$

$$r_2 = \frac{\tilde{s}_1}{\tilde{s}_2} \cdot \frac{\tilde{s}_1^2 - 3\tilde{s}_0^2}{\tilde{s}_2^2 - 3\tilde{s}_0^2}$$

$$t_1 = \frac{\tilde{s}_2 - 2\tilde{s}_0}{\tilde{s}_2^2 - 3\tilde{s}_0^2}$$

$$t_2 = \frac{1}{\tilde{s}_2^3 - 3\tilde{s}_0^2 \tilde{s}_2}.$$

ϕ_0 is thus defined in terms of local potentials, which are unknown, and the cavity velocity, which is known. As a result, ϕ_0 is split so that the known part is on the right-hand-side and the unknown part is on the left-hand-side.

For a discussion of the importance of ϕ_0 to the solution, see in section 4.3.

Incorporating the discrete boundary conditions, the discretized Green's formulae take the following form:

On S_{CB}

$$\begin{aligned}
& \sum_{m=1}^M \left\{ \sum_{n=1}^{N_{LB}} A_{inm} \phi_{nm} + \sum_{n=N_{LB}+N_{CAV_m}+1}^N A_{inm} \phi_{nm} + [R_{1m} \phi_{1m} + R_{2m} \phi_{2m} + R_{3m} \phi_{3m}] \xi_{im} - \right. \\
& \left. - \sum_{n=N_{LB}+1}^{N_{LB}+N_{CAV_m}} B_{inm} \frac{\partial \phi}{\partial n_{nm}} - \sum_{l=1}^{N_{Cm}} C_{ilm} Q_{lm} + W_{ilm} [(1 - \text{SOP}_m) \phi_{Nm} - \phi_{1m}] \right\} = \\
& = \sum_{m=1}^M \left\{ - \sum_{n=1}^{N_{CAV_m}} A_{i(N_{LB}+n)m} \Psi_{nm} - \sum_{n=1}^{N_{LB}} B_{inm} U_{in_{nm}} \cdot \hat{n}_{nm} - \sum_{n=N_{LB}+1}^N B_{inm} U_{in_{nm}} \cdot \hat{n}_{nm} \right. \\
& \left. - \text{SOP}_m W_{ilm} \Psi_{Nm} - R_{4m} q_{0m} \xi_{im} \right\} + \left\{ \text{RHS} \right\}_{S_{CBi}} \quad i = 1, \dots, N \times M \quad (3.13)
\end{aligned}$$

where

$$\xi_{im} = \sum_{n=N_{LB}+1}^{N_{LB}+N_{CAV_m}} A_{inm} + \text{SOP}_m W_{ilm}.$$

On S_{CW}

$$\begin{aligned}
& \sum_{m=1}^M \left\{ \sum_{n=1}^{N_{LB}} D_{inm} \phi_{nm} + \sum_{n=N_{LB}+N_{CAV_m}+1}^N D_{inm} \phi_{nm} + [R_{1m} \phi_{1m} + R_{2m} \phi_{2m} + R_{3m} \phi_{3m}] \xi_{im} - \right. \\
& \left. - \sum_{n=N_{LB}+1}^{N_{LB}+N_{CAV_m}} E_{inm} \frac{\partial \phi}{\partial n_{nm}} - \sum_{l=1}^{N_{Cm}} F_{ilm} Q_{lm} + W_{ilm}^* [(1 - \text{SOP}_m) \phi_{Nm} - \phi_{1m}] \right\} = \\
& = -4\pi \Psi_i + \sum_{m=1}^M \left\{ - \sum_{n=1}^{N_{CAV_m}} D_{i(N_{LB}+n)m} \Psi_{nm} - \sum_{n=1}^{N_{LB}} E_{inm} U_{in_{nm}} \cdot \hat{n}_{nm} - \right. \\
& \quad \left. \sum_{n=N_{LB}+N_{CAV_m}+1}^N E_{inm} U_{in_{nm}} \cdot \hat{n}_{nm} \right. \\
& \left. - \text{SOP}_m W_{ilm}^* \Psi_{Nm} - R_{4m} q_{0m} \xi_{im} \right\} + \left\{ \text{RHS} \right\}_{S_{CW_i}} \quad i = 1, \dots, N_{CW} \quad (3.14)
\end{aligned}$$

where

$$\xi_{im} = \begin{cases} \sum_{n=N_{LB}+1}^{N_{LB}+N_{CAV_m}} D_{inm} + \text{SOP}_m W_{i1m}^* + 4\pi & \text{if } i \text{ is on the } m^{\text{th}} \text{ strip} \\ \sum_{n=N_{LB}+1}^{N_{LB}+N_{CAV_m}} D_{inm} + \text{SOP}_m W_{i1m}^* & \text{otherwise} \end{cases}$$

In order to write (3.13) and (3.14), which are true for arbitrary cavity planforms including partial and/or supercavitation, it was necessary to introduce the switch SOP_m to indicate whether a given strip is supercavitating or partially cavitating. This switch is defined as follows:

$$\text{SOP}_m \stackrel{\text{def}}{=} \begin{cases} 1.0 & \text{if the } m^{\text{th}} \text{ strip is supercavitating} \\ 0.0 & \text{otherwise.} \end{cases}$$

Chapter 4

Solution

The aim of this chapter is to complete the description of the solution methodology. The system of equations which must be solved for each planform iteration at each time step is written down and the efficient and robust algorithm for arriving at the correct planform is described. Issues attendant to the algorithm are discussed, including uniqueness and sensitivity to tolerances. The method of time-marching is outlined, followed by the details of obtaining post-processed results, such as the pressure distribution and the cavity shape.

4.1 Solution for Given Cavity Planform

As mentioned, the planform of the cavity, $l(r, t)$, is unknown and has to be determined as a part of the solution. However, since $l(r, t)$ will be determined iteratively by successive guesses, the problem of determining the cavity shape at a prescribed ("guessed") planform will be addressed first.

For a given guess of the cavity planform, (3.13) and (3.14) are satisfied at the control points on the blade and in the wake and the resulting linear system is solved with respect to the unknown source and dipole strengths. However, before solving the system of equations, I have to address the following problem: for a given discretization and an arbitrary guess of $l(r, t)$, the trailing edge of the cavity will not *necessarily* coincide with a panel boundary in the chordwise direction. This is a problem because the singularity distributions which represent the cavity span an integral number of

panels. There are several options for circumventing this problem, one being to simply re-panel the blade surface so that the cavity trailing edge does coincide with a panel boundary. This idea is rejected immediately due to the inordinate expense of recomputing influence coefficients¹. Another option is to approximate the cavity planform by ending the cavity at the nearest panel boundary on each spanwise strip. Although this method has been applied with some success, it was found that the convergence to the correct cavity planform suffered due to discontinuous intermediate discrete cavity planforms [36]. To address this problem we invented the *split-panel technique*, in which the panel at the trailing edge of the cavity is *split* into a cavitating and a non-cavitating part. Figure 4-1 describes this schematically. In the figure, the discretized blade is represented by a rectangular grid and the smooth cavity planform overlays the grid and is seen to cut one chordwise panel on each spanwise strip. The lengths of the split panels at their midspans are l_{L_m} and l_{R_m} , respectively. The split-panel method allows the discrete cavity planforms to be smooth without the added burden of re-computing influence coefficients.

4.1.1 Details of the Split-Panel Method

The source and dipole strengths on the split panels (ϕ_{spm} and $\frac{\partial \phi}{\partial n_{spm}}$) on the blade are defined as averages

$$\phi_{spm} = \frac{\phi_{L_m} l_{L_m} + \phi_{R_m} l_{R_m}}{l_{L_m} + l_{R_m}} \quad \frac{\partial \phi}{\partial n_{spm}} = \frac{\frac{\partial \phi}{\partial n_{L_m}} l_{L_m} + \frac{\partial \phi}{\partial n_{R_m}} l_{R_m}}{l_{L_m} + l_{R_m}} \quad \text{on the split panel} \quad (4.1)$$

with the weights l_{L_m} and l_{R_m} taken as the lengths at the midspan of the split panels. For compactness, the split-panel dipole and source strengths will henceforth be written

$$\phi_{spm} = \phi_{L_m} F_{L_m} + \phi_{R_m} F_{R_m} \quad \frac{\partial \phi}{\partial n_{spm}} = \frac{\partial \phi}{\partial n_{L_m}} F_{L_m} + \frac{\partial \phi}{\partial n_{R_m}} F_{R_m} \quad (4.2)$$

¹Remember the theme discussed in section 2.2: avoid re-computing influence coefficients!

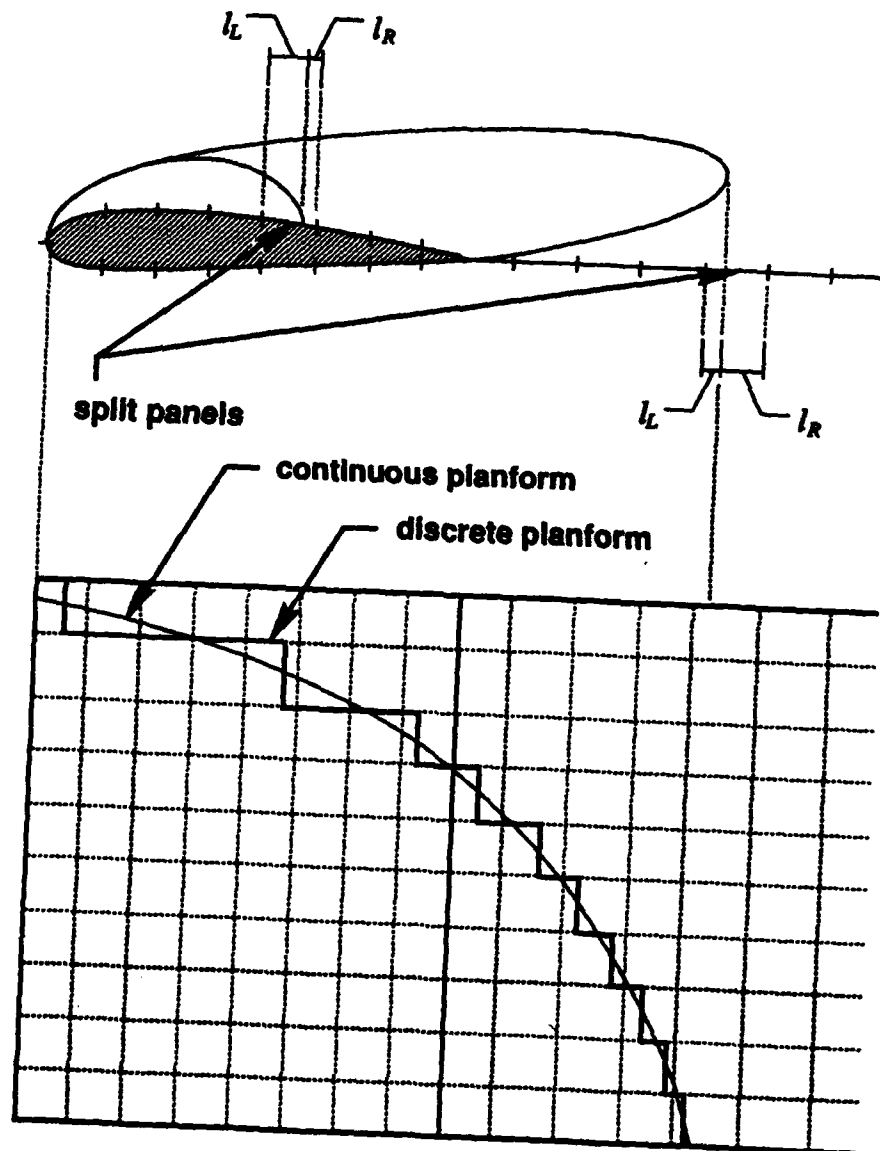


Figure 4-1: Schematic of a cavity planform, showing the split panels.

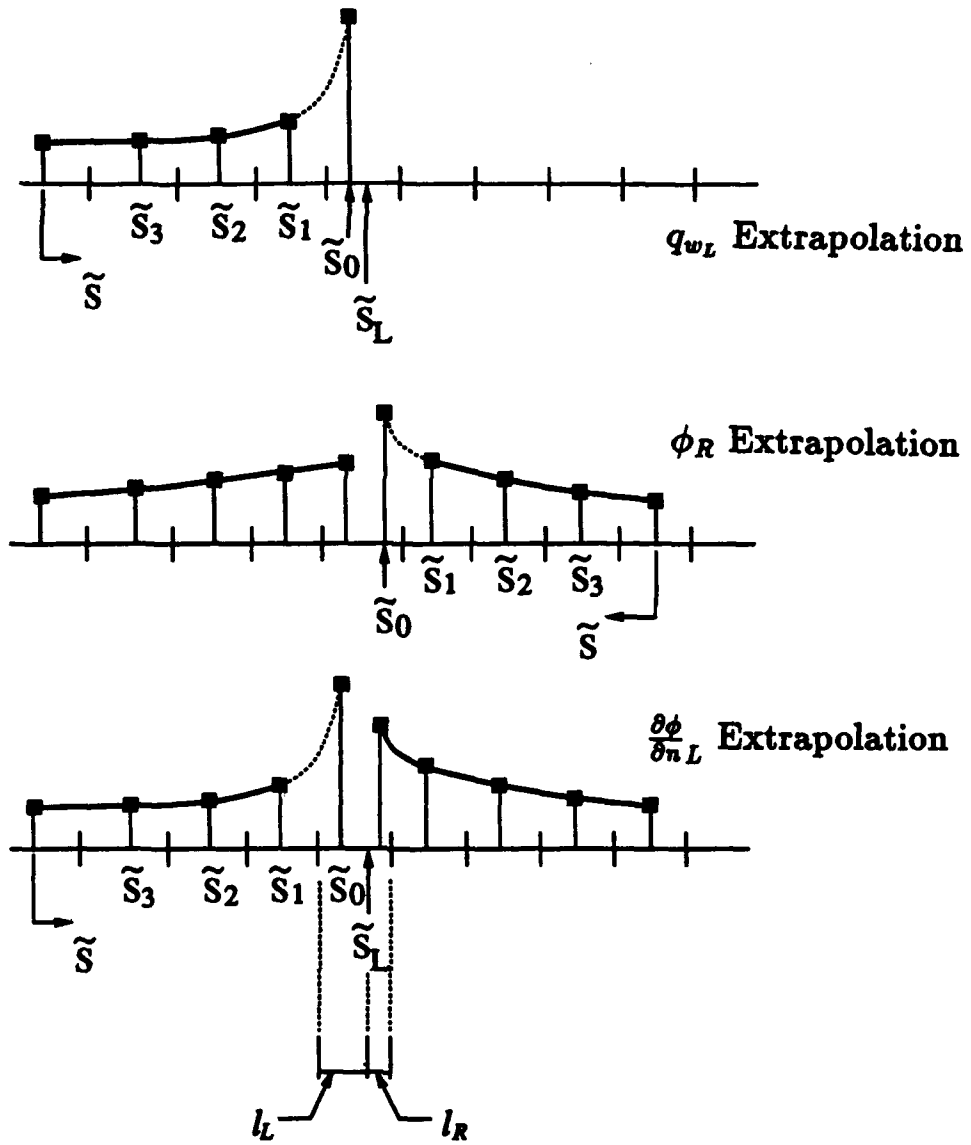


Figure 4-2: Sketch defining split panel extrapolations.

where the factors F_{L_m} and F_{R_m} are defined as follows:

$$F_{L_m} = \frac{l_{L_m}}{l_{L_m} + l_{R_m}}$$

$$F_{R_m} = \frac{l_{R_m}}{l_{L_m} + l_{R_m}}.$$

The quantities ϕ_{L_m} and $\frac{\partial \phi}{\partial n}_{R_m}$ are known from the boundary conditions, (2.17) and (2.33). The quantities ϕ_{R_m} and $\frac{\partial \phi}{\partial n}_{L_m}$ are unknown, but may be defined as extrapolations of the unknowns on adjacent panels, similar to the definition of ϕ_{0_m} in section 3.3. Using the notation of Figure 4-2, ϕ_{R_m} is defined by a cubic extrapolation

of the unknown potentials at the four adjacent control points:

$$\phi_{R_m} = P_{1_m} \phi_{1_m} + P_{2_m} \phi_{2_m} + P_{3_m} \phi_{3_m} + P_{4_m} \phi_{4_m}. \quad (4.3)$$

where

$$\begin{aligned} P_{1_m} &= \frac{\bar{s}_0^3 - \bar{s}_0^2(\bar{s}_2 + \bar{s}_3) + \bar{s}_0 \bar{s}_2 \bar{s}_3}{\bar{s}_1(\bar{s}_2 - \bar{s}_1)(\bar{s}_3 - \bar{s}_1)} \\ P_{2_m} &= \frac{-\bar{s}_0^3 - \bar{s}_0^2(\bar{s}_1 + \bar{s}_3) - \bar{s}_0 \bar{s}_1 \bar{s}_3}{\bar{s}_2(\bar{s}_3 - \bar{s}_2)(\bar{s}_2 - \bar{s}_1)} \\ P_{3_m} &= \frac{\bar{s}_0^3 - \bar{s}_0^2(\bar{s}_2 + \bar{s}_1) + \bar{s}_0 \bar{s}_1 \bar{s}_2}{\bar{s}_3(\bar{s}_3 - \bar{s}_2)(\bar{s}_3 - \bar{s}_1)} \\ P_{4_m} &= 1 + \frac{-\bar{s}_0^3 + \bar{s}_0^2(\bar{s}_1 + \bar{s}_2 + \bar{s}_3) - \bar{s}_0(\bar{s}_1 \bar{s}_2 + \bar{s}_1 \bar{s}_3 + \bar{s}_2 \bar{s}_3)}{\bar{s}_1 \bar{s}_2 \bar{s}_3} \end{aligned} \quad (4.4)$$

$\frac{\partial \phi}{\partial n_{L_m}}$ is also defined as a polynomial extrapolation, but I found it necessary to include a term which is square-root singular at the cavity trailing edge. In this way, the correct behavior of $\frac{\partial \phi}{\partial n}(s)$ near the end of the cavity is captured:

$$\frac{\partial \phi}{\partial n}(\bar{s}) \simeq a(\bar{s} - \bar{s}_L)^2 + b(\bar{s} - \bar{s}_L) + \frac{c}{\sqrt{\bar{s} - \bar{s}_L}} + d.$$

This allows me to write $\frac{\partial \phi}{\partial n_{L_m}}$ as (again using the notation of Figure 4-2)

$$\frac{\partial \phi}{\partial n_{L_m}} = S_{1_m} \frac{\partial \phi}{\partial n_{1_m}} + S_{2_m} \frac{\partial \phi}{\partial n_{2_m}} + S_{3_m} \frac{\partial \phi}{\partial n_{3_m}} + S_{4_m} \frac{\partial \phi}{\partial n_{4_m}}. \quad (4.5)$$

where

$$\begin{aligned} S_{1_m} &= \frac{\bar{s}_2}{D} \left[\frac{T_1}{\sqrt{\bar{s}_L}} - \frac{\bar{s}_L}{\bar{s}_3} (Q_1 T_3 - T_1 Q_3) - \bar{s}_L^2 Q_1 \right] \\ S_{2_m} &= \bar{s}_L^2 \left[\frac{\bar{s}_1 T_1 + \bar{s}_3 T_2}{D} \frac{Q_1}{T_1} + \frac{\bar{s}_3}{T_1} \right] + \bar{s}_L \left[\frac{\frac{1}{\bar{s}_3} T_1 + T_2}{D} \left(\frac{Q_1 T_3}{T_1} - Q_3 \right) + \frac{T_3}{T_1} \right] \\ &\quad - \frac{\bar{s}_1 T_1 + \bar{s}_3 T_2}{D \sqrt{\bar{s}_L}} \\ S_{3_m} &= -\bar{s}_L^2 \left(\frac{\bar{s}_2}{T_1} + \frac{\bar{s}_1 T_1 + \bar{s}_3 T_2}{D} \right) - \bar{s}_L \left(-\frac{1}{\bar{s}_3} + \frac{\bar{s}_2 T_3}{\bar{s}_3 T_1} + \frac{\bar{s}_2 T_2 Q_1 T_3}{\bar{s}_3 T_1 D} - \frac{\bar{s}_2 T_3 Q_3}{\bar{s}_3 D} \right) \end{aligned}$$

$$\begin{aligned}
& + \frac{\bar{s}_2 T_2}{D \sqrt{\bar{s}_L}} \\
S_{4m} = & 1 - \bar{s}_L^2 \left(\frac{\bar{s}_3 - \bar{s}_2}{T_1} + \frac{N Q_1}{D T_1} \right) - \bar{s}_L \left(\frac{1}{\bar{s}_3} + \frac{(\bar{s}_3 - \bar{s}_2) T_3}{\bar{s}_3 T_1} + \frac{N Q_1 T_3}{\bar{s}_3 D T_1} - \frac{N Q_3}{\bar{s}_3 D} \right) \\
& + \frac{N}{D \sqrt{\bar{s}_L}}
\end{aligned} \tag{4.6}$$

and where

$$\begin{aligned}
Q_1 &= \frac{\bar{s}_2}{\sqrt{\bar{s}_L - \bar{s}_3}} - \frac{\bar{s}_3}{\sqrt{\bar{s}_L - \bar{s}_2}} \frac{\bar{s}_3 - \bar{s}_2}{\sqrt{\bar{s}_L}} \\
Q_2 &= \frac{\bar{s}_1}{\sqrt{\bar{s}_L - \bar{s}_2}} - \frac{\bar{s}_2}{\sqrt{\bar{s}_L - \bar{s}_1}} \frac{\bar{s}_2 - \bar{s}_1}{\sqrt{\bar{s}_L}} \\
Q_3 &= \frac{1}{\sqrt{\bar{s}_L - \bar{s}_3}} - \frac{1}{\sqrt{\bar{s}_L}} \\
T_1 &= \bar{s}_2 \bar{s}_3^2 - \bar{s}_2^2 \bar{s}_3 \\
T_2 &= \bar{s}_1 \bar{s}_2^2 - \bar{s}_1^2 \bar{s}_2 \\
T_3 &= \bar{s}_3^2 - 2 \bar{s}_L \bar{s}_3 \\
N &= (\bar{s}_1 - \bar{s}_2) T_1 + (\bar{s}_3 - \bar{s}_2) T_2 \\
D &= Q_2 T_1 - Q_1 T_2
\end{aligned} \tag{4.7}$$

In a similar manner, the source strengths at the wake panels which are split by the trailing edge of the supercavity are defined as

$$Q_{sp_m} = \frac{Q_{L_m} l_{L_m}}{l_{L_m} + l_{R_m}}. \tag{4.8}$$

Q_{L_m} is defined as a polynomial extrapolation in terms of the adjacent unknown cavity source strengths, similar to the definition of $\frac{\partial \phi}{\partial n L_m}$:

$$Q_{L_m} = T_{1m} q_{1m} + T_{2m} q_{2m} + T_{3m} q_{3m} + T_{4m} q_{4m}. \tag{4.9}$$

The expressions which define T_{1m}, \dots, T_{4m} are identical to the expressions which define S_{1m}, \dots, S_{4m} in (4.6). However, since \bar{s} for the Q_{L_m} extrapolation is different from the

\bar{s} used in the $\frac{\partial \phi}{\partial n L_m}$ extrapolation, separate symbols are necessary.

Error Due to Split-Panel Method

There are two sources of error in the split-panel method. They are:

- due to the fact that ϕ_{R_m} and $\frac{\partial \phi}{\partial n L_m}$ are defined by extrapolations which are not exact
- due to the averaging of the influence of two panels into one.

The first source of error is bounded by that of the $\frac{\partial \phi}{\partial n L}$ extrapolation, since the behavior of the source strength is square-root singular near the cavity trailing edge (while the dipole strength is smooth). The correctness of the extrapolation may be gauged in the following way: first solve for the singularity strengths for a two-dimensional flow for given σ , a given guess of the cavity length (without searching for the closed cavity) and a given discretization (using the split-panel method). Next, solve the same problem where the split panel is treated as two distinct panels. The source strength on the left split panel, $\frac{\partial \phi}{\partial n L}$, should be close to the computed source strength. In addition, the source strengths on neighboring panels from the two computations should be equivalent. Figure 4-3 shows the two computations, where the $\frac{\partial \phi}{\partial n L}$ is defined by a plain cubic extrapolation of neighboring unknowns (left) and by the extrapolation just described (right). Comparing the two plots, it is clear that the extrapolation with the square-root singular term is necessary.

The second source of error, due to the averaging of the panel influence, is investigated by the following test: consider the influence of a unit source panel in two dimensions which has been split into two panels at some arbitrary fraction of its length. As depicted in Figure 4-4, the total influence at some field point is the sum of the influence of the left and right interior panels. Denoting B_W as the influence of the original unsplit panel, the induced potential B may be written

$$B = B_L + B_R = B_W \left[\frac{B_L}{B_W} + \frac{B_R}{B_W} \right]$$

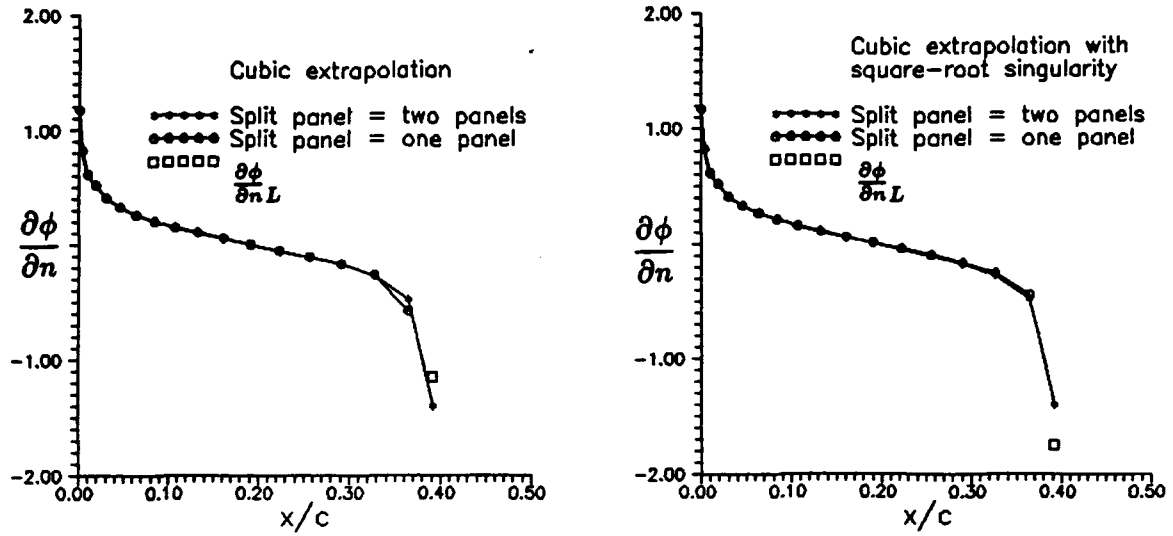


Figure 4-3: Comparison of the source strength computed with a cavity-fit grid to that computed by the split panel method. In the plot on the left, $\frac{\partial \phi}{\partial n}$ is defined as a cubic extrapolation of neighboring unknowns. On the right, $\frac{\partial \phi}{\partial n}$ is defined as a cubic extrapolation with singular term, as in the text. Computations are for a NACA16006 foil with $\sigma = 1.0$, $\alpha = 3^\circ$, and a guess of the cavity length $\frac{l}{c} = 0.4$.

where B_L and B_R are the induced potentials due to the left and right interior panels, respectively. Referring to equation (4.2), it is evident that the split-panel method amounts to approximating the quantities $\frac{B_L}{B_w}$ and $\frac{B_R}{B_w}$ with the constants F_L and F_R . In other words, for all field points the split-panel method makes the approximations $\frac{B_L}{B_w} \approx F_L$ and $\frac{B_R}{B_w} \approx F_R$. This approximation may be expected to do well if the field point is far from the singularities, but break down for field points nearby. In Figure 4-4, the ratio $\frac{B_L}{B_w}$ is shown for a series of field points arrayed along a line adjacent and parallel to a split source panel. To be consistent with the hydrofoil solution, the closest field point is one half a panel length away. From this figure, it is clear that the approximation breaks down within several panel lengths.

The effect of the split panel error on the global solution may be seen by comparing the cavity length for fixed geometry and a given σ obtained from various initial guesses. If the split panel error has a large effect on the solution, then the final cavity length (corresponding to a closed cavity at the given cavitation number) would depend strongly on the initial guess. It has been found that the cavity length depends very

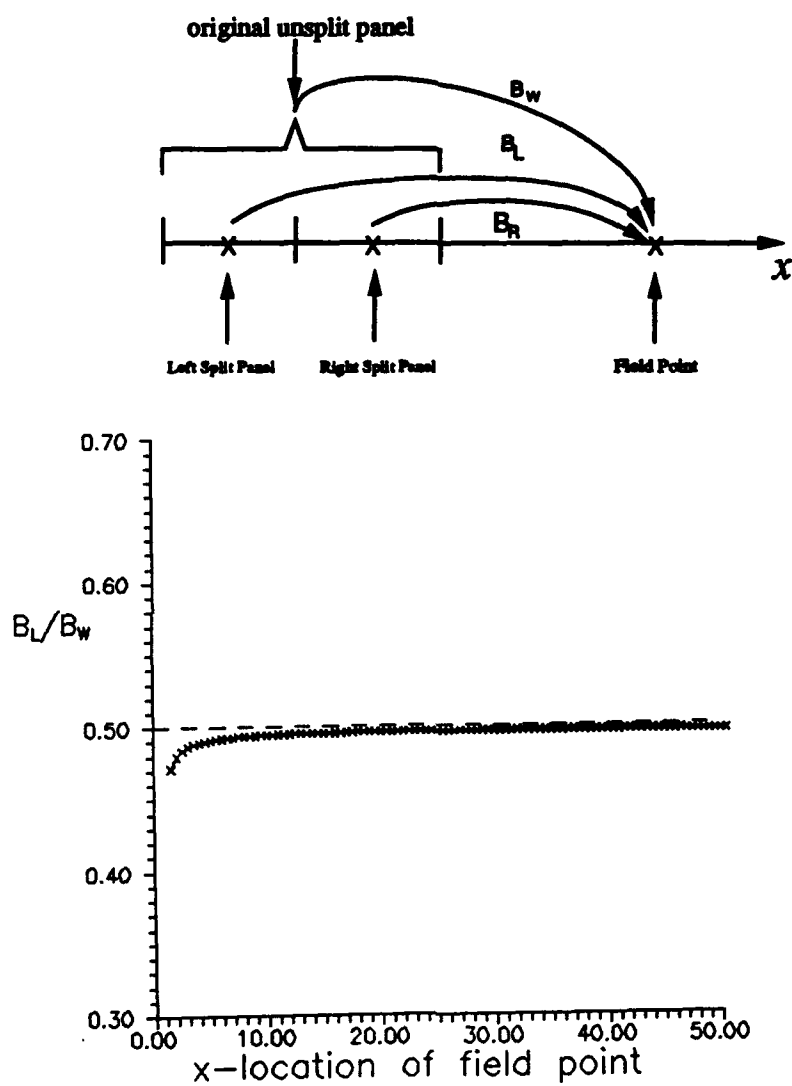


Figure 4-4: Investigation of the error due to representing two interior source panels with a single panel. The length of the unsplit panel is 1.0. The panel is split in half to form two sub-panels. The panel configuration and a sketch of the individual influences are shown above a plot of the ratio $\frac{B_L}{B_W}$.

weakly on the initial guess, and this is shown in Appendix B.

4.1.2 System of Equations

For a given cavity planform, $l(r, t)$, Green's formula should be satisfied at the control points of all $N \times M - n_{spm}$ panels on the key blade. As before, N is the number of panels distributed around the chord of the blade and M is the number of panels distributed spanwise (i.e., the number of strips). n_{spm} is the number of panels on the blade which are "split" by the trailing edge of the cavity (Green's formula is not applied on the split panels). In addition to the applications of Green's formula on the key blade, Green's formula in the wake is satisfied at the N_{CW} cavitating panels on S_{CW} (N_{CW} does not count the split panels on S_{CW}).

The final system of equations, including the influence of the split panels, is as follows:

On S_{CB}

$$\begin{aligned}
 \sum_{m=1}^M \left\{ \sum_{n=1}^{N_{LB}} A_{inm} \phi_{nm} + \sum_{n=N_{LB}+N_{CAV_m}+1}^N A_{inm} \phi_{nm} + [R_{1m} \phi_{1m} + R_{2m} \phi_{2m} + R_{3m} \phi_{3m}] \xi_{im} \right. \\
 + \phi_{Lm} A_{imn_{spm}} F_{Rm} - \sum_{n=N_{LB}+1}^{N_{LB}+N_{CAV_m}} B_{inm} \frac{\partial \phi}{\partial n_{nm}} - \frac{\partial \phi}{\partial n_L} B_{imn_{spm}} F_{Lm} \\
 \left. - \sum_{l=1}^{N_{Cm}} C_{ilm} Q_{lm} - Q_{Lm} C_{imn_{spm}} F_{Lm} + W_{ilm} [(1 - SOP_m) \phi_{Nm} - \phi_{1m}] \right\} = \\
 \sum_{m=1}^M \left\{ - \sum_{n=1}^{N_{CAV_m}} A_{i(N_{LB}+n)m} \Psi_{nm} - A_{imn_{spm}} \Psi_{n_{spm}m} F_{Lm} - \sum_{n=1}^{N_{LB}} B_{inm} U_{in_{nm}} \cdot \hat{n}_{nm} - \right. \\
 - \sum_{n=N_{LB}+N_{CAV_m}+1}^N B_{inm} U_{in_{nm}} \cdot \hat{n}_{nm} - \\
 \left. - B_{imn_{spm}} U_{in_{nm}n_{spm}} \cdot \hat{n}_{nmn_{spm}} F_{Rm} - SOP_m W_{ilm} \Psi_{N_{CAV_m}m} - R_{4m} q_{0m} \xi_{im} \right\} + \\
 + RHS_{S_{CB}i} \quad i = 1, \dots, N \times M - n_{spm} \quad (4.10)
 \end{aligned}$$

where

$$\xi_{im} = \sum_{n=N_{LB}+1}^{N_{LB}+N_{CAV_m}} A_{inm} + A_{i,n_{sp_m}} F_{Lm} + \text{SOP}_m W_{i1m}.$$

On S_{CW}

$$\begin{aligned} \sum_{m=1}^M \left\{ \sum_{n=1}^{N_{LB}} D_{inm} \phi_{nm} + \sum_{n=N_{LB}+N_{CAV_m}+1}^N D_{inm} \phi_{nm} + [R_{1m} \phi_{1m} + R_{2m} \phi_{2m} + R_{3m} \phi_{3m}] \xi_{im} \right. \\ \left. + \phi_{Lm} D_{imn_{sp_m}} F_{Rm} - \sum_{n=N_{LB}+1}^{N_{LB}+N_{CAV_m}} E_{inm} \frac{\partial \phi}{\partial n_{nm}} - \frac{\partial \phi}{\partial n_{Lm}} E_{imn_{sp_m}} F_{Lm} \right. \\ \left. - \sum_{l=1}^{N_{Cm}} F_{ilm} Q_{lm} - Q_{Lm} F_{imn_{sp_m}} F_{Lm} + W_{i1m} [(1 - \text{SOP}_m) \phi_{Nm} - \phi_{1m}] \right\} = \\ -4\pi \Psi_i + \sum_{m=1}^M \left\{ - \sum_{n=1}^{N_{CAV_m}} D_{i(N_{LB}+n)m} \Psi_{nm} - D_{imn_{sp_m}} \Psi_{mn_{sp_m}} F_{Lm} - \right. \\ \left. - \sum_{n=1}^{N_{LB}} E_{inm} U_{in_{nm}} \cdot \hat{n}_{nm} - \sum_{n=N_{LB}+N_{CAV_m}+1}^N E_{inm} U_{in_{nm}} \cdot \hat{n}_{nm} - \right. \\ \left. E_{imn_{sp_m}} U_{in_{sp_m}} \cdot \hat{n}_{n_{sp_m}} F_{Rm} - \text{SOP}_m W_{i1m} \Psi_{Nm} - R_{4m} q_{0m} \xi_{im} \right\} + \text{RHS}_{S_{CW,i}} \\ i = 1, \dots, N \times M \quad (4.11) \end{aligned}$$

where

$$\xi_{im} = \begin{cases} \sum_{n=N_{LB}+1}^{N_{LB}+N_{CAV_m}} D_{inm} + \text{SOP}_m W_{i1m} + D_{in_{sp_m}m} F_{Lm} + 4\pi & \text{if } i \text{ is on the } m^{\text{th}} \text{ strip} \\ \sum_{n=N_{LB}+1}^{N_{LB}+N_{CAV_m}} D_{inm} + \text{SOP}_m W_{i1m} + D_{in_{sp_m}m} F_{Lm} & \text{otherwise} \end{cases}$$

n_{sp_m} is the chordwise index of the split panel on the m^{th} strip.

The system of equations (4.10) and (4.11) must be solved at each time step. This is accomplished by an accelerated block-iterative matrix solver [7, 17].

4.1.3 Cavity Height Computation

Once the problem has been solved for a guessed cavity planform, and $\frac{\partial \phi}{\partial n}$ on the cavity panels is known, the cavity height ($h(s, v, t)$ on the blade and $h_w(s, v, t)$ in the wake) can be determined by integrating the partial differential equations (2.23) and (2.30). This is accomplished by replacing the partial derivatives of h and h_w with two-point backwards difference formulae and solving for h and h_w recursively. Note that the derivatives are defined at the control points. The finite difference models of the derivatives are as follows (h_w may be substituted for h):

$$\begin{aligned}\frac{\partial h}{\partial s} &\approx \frac{h_{(i+1)m}^n - h_{im}^n}{\Delta s_i} \\ \frac{\partial h}{\partial v} &\approx \frac{3\bar{h}_{im}^n - 4\bar{h}_{i(m-1)}^n + \bar{h}_{i(m-2)}^n}{3\Delta v_1 - \Delta v_2} \\ \frac{\partial h}{\partial t} &\approx \frac{\bar{h}_{im}^n - \bar{h}_{im}^{n-1}}{\Delta t}\end{aligned}$$

where

$$\bar{h}_{im} = \frac{1}{2}(h_{(i+1)m}^n + h_{im}^n)$$

Refer to Figure 4-5 for clarification. Substitution of the finite differences in (2.23) and (2.30) yields recursive formulae for h_{i+1}^n and $h_{w,i+1}^n$ in terms of previously computed quantities. The height of the cavity at its trailing edge, $\delta(r, t)$, will in general be non-zero, unless we have guessed the correct cavity planform. The means by which we arrive at the correct planform will be discussed next.

4.2 Finding the Cavity Planform

To find the correct discrete cavity planform we need to solve, with respect to the M unknowns l_1, l_2, \dots, l_M , the system of equations

$$\delta_m(l_1, l_2, \dots, l_M; \sigma) = 0 \quad m = 1, \dots, M \quad (4.12)$$

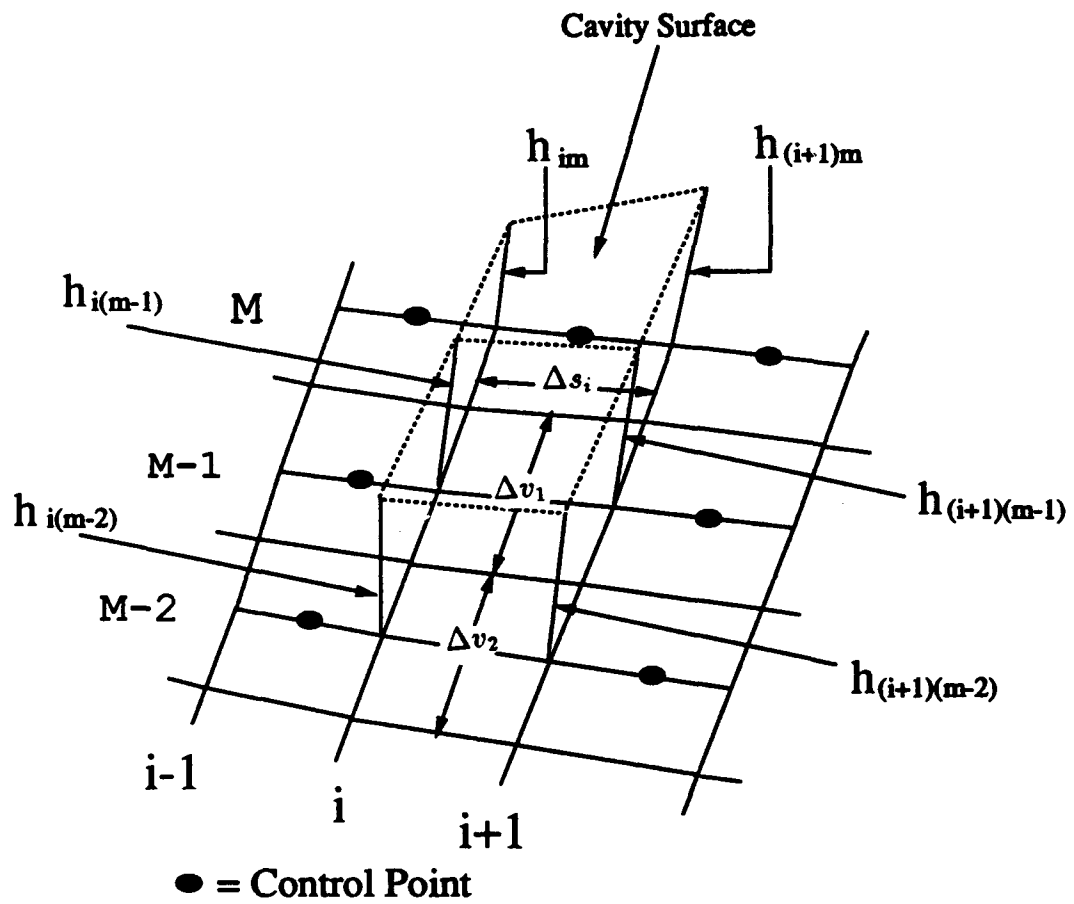


Figure 4-5: Schematic of cavity height computation.

where δ_m is the openness of the cavity trailing edge at the m^{th} spanwise strip and l_m is the cavity length at midspan of the same strip. The system of equations (4.12) may be solved iteratively by applying an M-dimensional Newton-Raphson (secant method) scheme. The updated cavity lengths for the $(k+1)^{\text{st}}$ iteration are given as follows:

$$L^{k+1} = -J^{-1}\delta^k + L^k \quad (4.13)$$

where

$$\begin{aligned} L^T &= [l_1 \ l_2 \ l_3 \ \dots \ l_m] \\ \delta^T &= [\delta_1 \ \delta_2 \ \delta_3 \ \dots \ \delta_m] \end{aligned}$$

and where J is the Jacobian, which has elements

$$J_{ij} = \frac{\partial \delta_i}{\partial l_j}, \quad 1 \leq i, j \leq M.$$

Ideally, we would like to approximate each element of the Jacobian by using a two point finite difference scheme. However, this would mean that the system of equations given by (4.10) and (4.11) would have to be solved $M+1$ times for each *Newton-Raphson iteration*. Even in the case of an accurate initial guess, this scheme clearly would be prohibitively expensive. Fortunately, the iterative method may be accelerated by applying a locally scalar Newton-Raphson (secant method) scheme at each spanwise strip, which is equivalent to ignoring the off-diagonal terms of the Jacobian in solving (4.13) for the updated cavity planform. This method requires only a single solution of the system of equations for each Newton-Raphson iteration.

The second guess of the planform is taken to be a perturbation of the initial guess by a fixed amount (equal to 2% of the local chord length, c_m) in a direction determined by the sign of the local δ_m which resulted from the initial guess. For example, if δ_m from the first guess is negative, then the local cavity length l_m is

shortened by $.02c_m$ for the second iteration. In general, this method will not be stable due to the importance of the off-diagonal terms of the Jacobian, which have been ignored. However, numerical damping renders the method stable by prohibiting each cavity length l_m from changing by an amount greater than a multiple of δ_m , $|\Delta l_m| \leq |k * \delta_m|$. In the event that $|\delta_m|$ is large, the change in length is bounded by $|\Delta l_m| \leq 0.05c_m$. The convergence history is found to be weakly dependent on k , and $k = 4$ yields satisfactory convergence. As in any iterative scheme, however, the speed of convergence is heavily dependent on the initial guess. Fortunately, in the unsteady propeller problem, the planform from the previous time step is an excellent initial guess.

At each time step, the planform will be considered to be converged when the maximum of the absolute values $|\delta_1| \dots |\delta_M|$ is less than or equal to δ_{tol} . The sensitivity of the solution to δ_{tol} is discussed in section 4.2.2.

To demonstrate the three dimensional behavior of δ in the vicinity of the correct cavity planform, Figure 4-6 shows the spanwise distribution of $\delta(y)$ for various cavity planforms on a rectangular hydrofoil. Among these cavity planforms, some lie to the left of the zero- δ planform, and some lie to the right. Notice that $\delta(y)$ for each planform that lies to the left of the correct planform is everywhere positive, while for those that lie to the right $\delta(y)$ is everywhere negative.

Several aspects of the solution are best discussed before describing the details of the unsteady solution. This is done in the following sections.

4.2.1 Multiplicity of Solutions

Figure 4-7 shows a series of planforms for a rectangular hydrofoil at an angle of attack of 5° , and for which the cavitation number is varied from $\sigma = 0.2$ to $\sigma = 1.6$. Below the planforms, the nondimensional cavity length at the midspan, $\frac{l}{c}(y = 0)$ is plotted versus the ratio $\frac{a}{c}$. All cavity planforms were computed using the same discretization ($N = 80$, $M = 20$). In order to avoid clutter, only a subset of the cavity planforms which were computed and presented as points on the $\frac{l}{c}(0)$ vs $\frac{a}{c}$ curve have been shown in the upper figure.

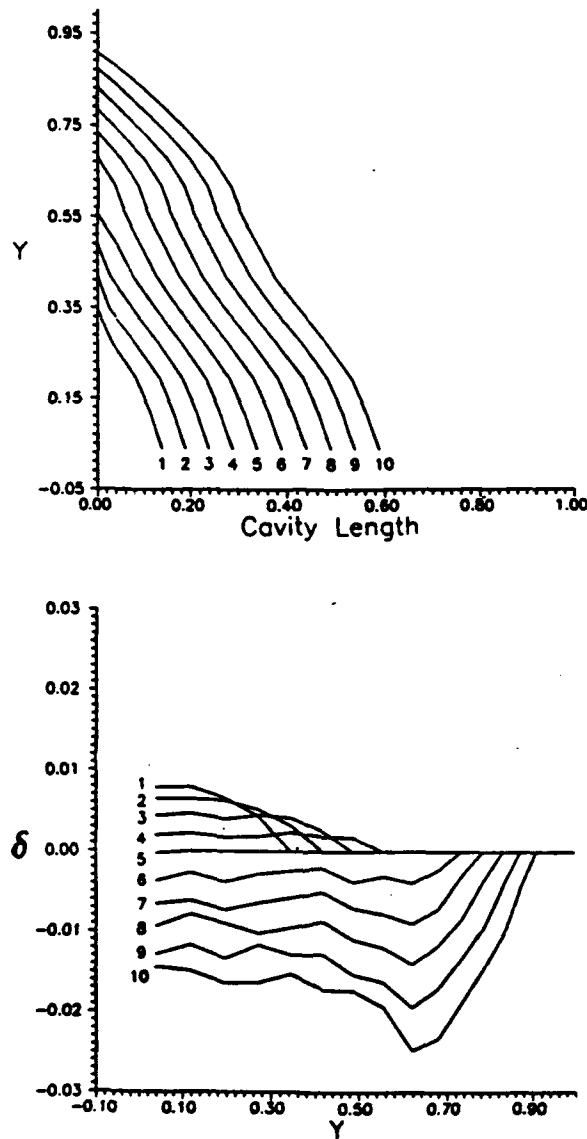


Figure 4-6: Spanwise $\delta(y)$ distributions for various cavity planforms on a rectangular hydrofoil which has a NACA65a crosssection. The curves are labeled 1-10 to correlate each cavity planform to its $\delta(y)$ curve. The thickness is $\frac{t}{c} = 0.05$ at the midspan, tapering elliptically to zero thickness at the tip. The angle of attack is $\alpha = 4^\circ$ and the cavitation number is $\sigma = 0.4$. The foil is twisted spanwise, and the angle of twist is given by $\alpha_t = -8y^3 + 12y^2$. The angle of twist is introduced to prevent the foil from cavitating near the tip.

The most striking result shown in Figure 4-7 is the apparent multiplicity of cavity planforms for a given cavitation number. Curves #3 and #4 both correspond to $\sigma = 0.9$, having been found by different initial guesses (which were uniform cavity planforms with $l(y) = 0.9$ and 1.3 , respectively). Both solutions are converged solutions ($\delta_m \leq \delta_{tol}$ for all m).

Except in a certain well defined regime, there is a one-to-one correlation between cavity length and cavitation number for two-dimensional cavity flows. Inside this regime, the multiplicity of solutions² causes no difficulty, since we know which solution is the physically acceptable one. Although it has generally been believed that the multiplicity of 2-D solutions does not occur for 3-D solutions, the present results appear to confirm the opposite. In fact, the $\frac{l}{c}(0)$ vs $\frac{\sigma}{\sigma_c}$ curve looks very similar to the corresponding 2-D result [1, 66].

Note that each solution in the present method corresponds to a "zero-crossing" of $\delta(y)$ as a function of the local cavity length $l(y)$. In our solution, only the zero-crossings for which the slopes of the $\delta(y)$ vs $l(y)$ curves were negative were searched for. In close correspondence with the multiplicity which occurs in two-dimensions, our method found two "negative-slope" solutions. Additional solutions may exist which our numerical scheme does not search for, corresponding to $\frac{\partial \delta}{\partial l}(y) > 0$ ("positive-slope") or to "mixed-slope" solutions where the sign of $\frac{\partial \delta}{\partial l}(y)$ varies with y . In particular, for the high aspect-ratio rectangular hydrofoil, there may exist a "positive-slope" solution which lies between the two "negative-slope" solutions. However, turning off our negative-slope requirement did not yield a positive-slope solution for this case. This may have been due to the proximity of the two negative-slope solutions. Concerning the possible existence of "mixed slope" solutions, we suspect that, if they exist, they correspond to planforms which have sharp spanwise discontinuities. Our method has never captured such a solution. It is clear that further investigation, perhaps including a cavitating 3-D hydrofoil experiment to examine the stability of long partial cavities and short supercavities, is necessary to resolve this issue.

²For some values of the parameter $\frac{\alpha}{\sigma}$ — α is the angle of attack and σ is the cavitation number — there correspond three cavity lengths, but only the shortest is physically observed [1].

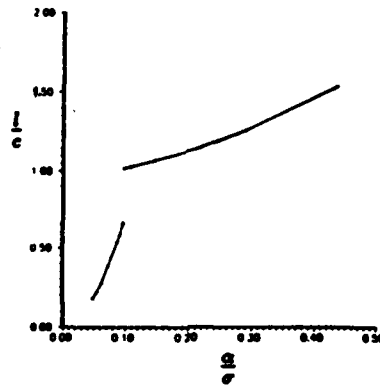
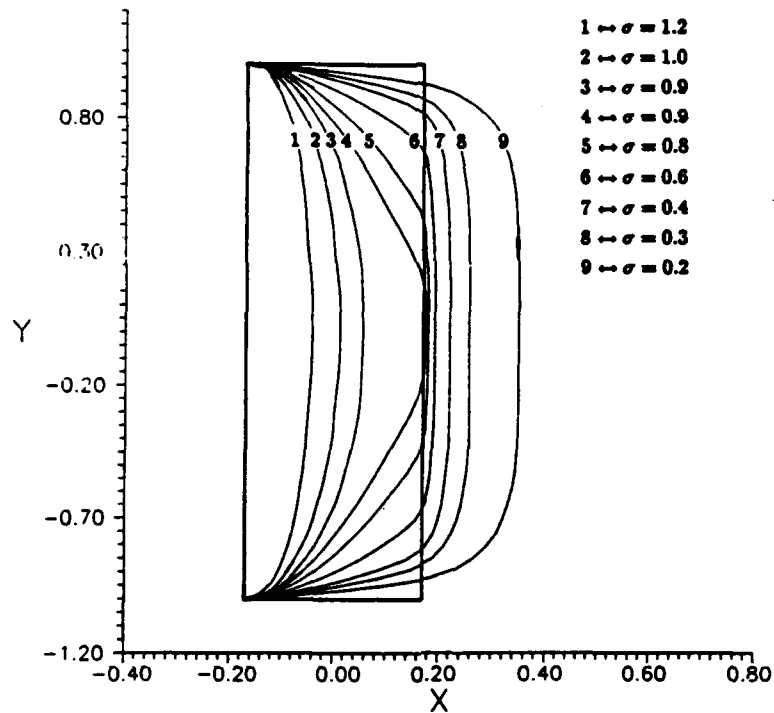


Figure 4-7: Dependence of the cavity planform on σ , showing the existence of multiple solutions.

As would be expected, the multiplicity vanishes as the aspect ratio becomes smaller. Figure 4-8 confirms that this is true for a rectangular foil of varying span-to-chord ratio.

4.2.2 Sensitivity of the Solution to δ Tolerance

Figure 4-9 shows the dependence of the computed cavity planforms on the tolerance on δ . The planform labeled number 1 (which is also the converged planform for $\delta_{tol} = 0.1$) has been used for the initial guess for all the planforms shown. The results shown in this figure suggest that δ_{tol} should be no larger than .001.

4.2.3 Nature of the Tip Solution

Of particular importance to the solution is the behavior of the tip flow. In reality, a cavitating foil or propeller blade which shows significant sheet cavitation typically has a cavitating tip vortex. I have found that the inviscid solution for elliptic hydrofoils, in cases where the tip is cavitating, shows a tendency toward very long supercavities at the tip. An example of this is shown in Figure 4-10. A numerical validation for this case is also presented in Figure 5-10 in section 5.2.2. Due to high skewness of the panels near the tip, it is difficult to obtain accurate representations of the geometry as well as accurate influence coefficients. As a result, it is often difficult for the solution to converge to within the tolerance set for δ . In order to stop the iterations, it was sometimes necessary to use a larger tolerance for δ for the outer 1-2% of the span. The corresponding $\delta(y)$ is also shown in Figure 4-10, where it is seen that δ is largest at the tip.

It may be possible to improve the tip solution, perhaps with the use of an orthogonal grid or a grid which conforms to the local streamlines, but this was not attempted in this work. One reason for avoiding these refinements is the apparent need to include the cavitating tip vortex in the model. It will be proposed that the inner sheet cavity solution be matched to an outer tip vortex solution, in which the vortex is assumed to be cavitating. This will be discussed further in Chapter 6.

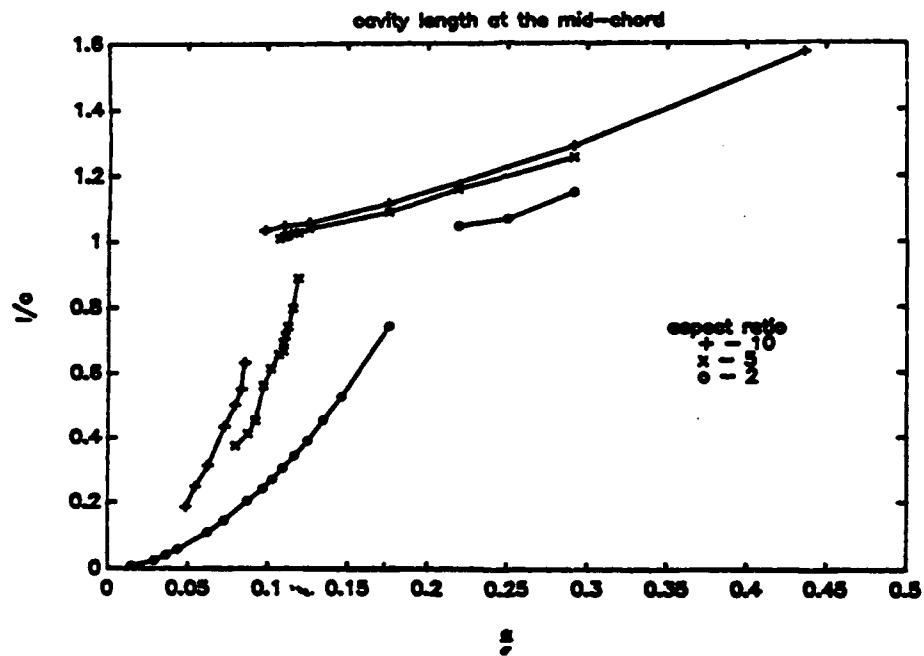
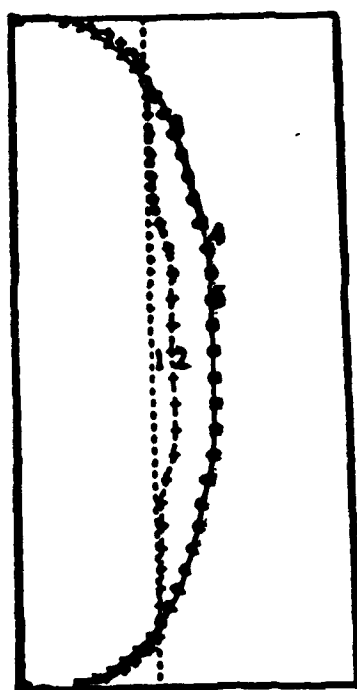
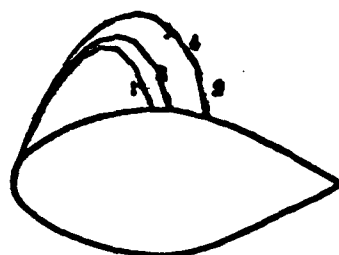


Figure 4-8: Effect of aspect ratio on multiplicity of solutions for a rectangular hydrofoil ($\frac{t}{c} = .05, \alpha = 5^\circ$). The cavity length at the midspan is shown vs $\frac{a}{c}$ for three aspect ratios $AR = 2, 5, 10$.



tolerance
 1 - 0.1
 2 - 0.01
 3 - 0.001
 4 - 0.0001
 5 - 0.00001

Figure 4-9: Dependence of the cavity planform on δ_{tot} , for a rectangular hydrofoil with a span-chord ratio of 5 at an angle of attack of 5° . (For clarity, the span and chord are not drawn to scale.)

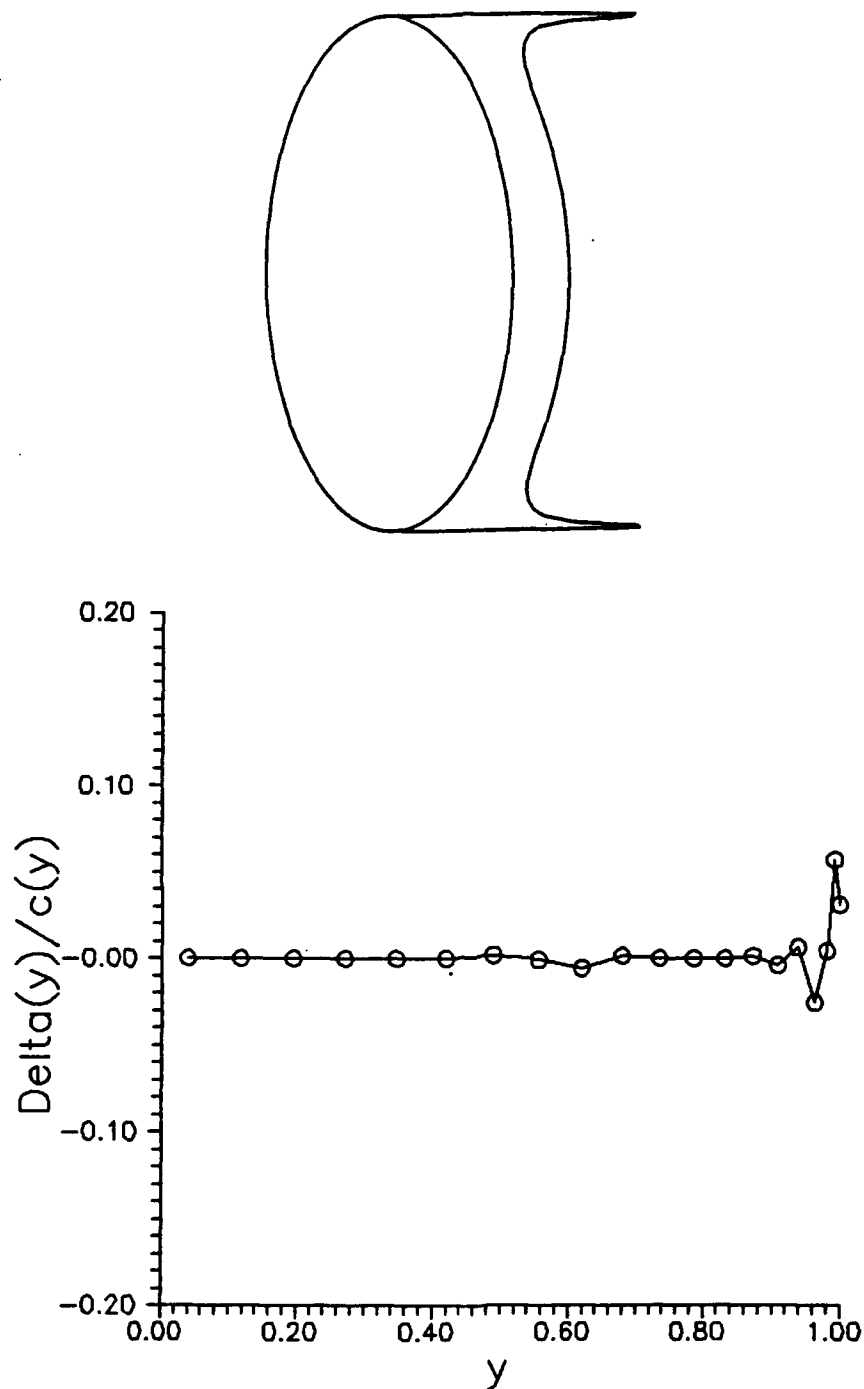


Figure 4-10: An example of a supercavitating elliptic hydrofoil at $\alpha = 3^\circ$ and $\sigma = .20$. The openness of the cavity at its trailing edge, $\delta(y)$ is shown also, where it can be seen that δ has a larger tolerance near the tip.

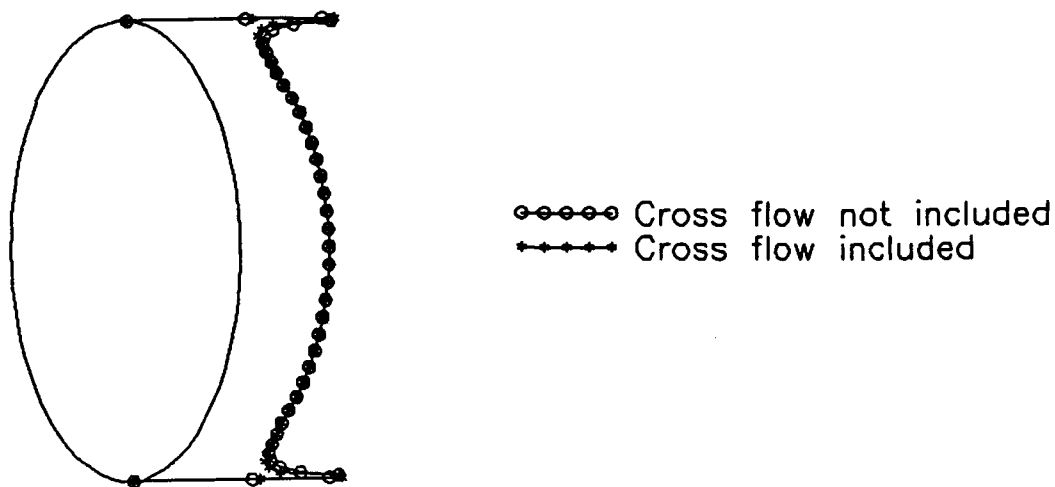


Figure 4-11: Convergence of the cavity planform with updating of the crossflow terms. Same foil and conditions as the previous figure.

4.2.4 Convergence of the Crossflow Term

It was mentioned in section 2.3 that the crossflow terms $\frac{\partial \phi}{\partial v}$ and V_u^+ in the dynamic boundary conditions (2.17) and (2.20) were found to have only a small effect on the solution. This will be shown for three geometries in this section. First, Figure 4-11 shows the cavity planforms from two consecutive iterations where, in between iterations for the cavity planform, the velocities $\frac{\partial \phi}{\partial v}$ and V_u^+ are updated. The first term is computed by numerically differentiating the potentials using second-order accurate central differences (except for $m = 1$ and $m = M$, where forward and backward differences are used, respectively). The second term is computed with central differences far downstream in the wake. Since the wake is assumed to be force-free, the crossflow velocity is constant in the streamwise direction for steady flow. This result is for an elliptic foil (the same foil and conditions shown in Figure 4-10). Note that the cavity planforms do not change significantly between the two iterations. No change was found when an additional iteration was tried. From this example, which showed only supercavitation, it may be concluded only that the term V_u^+ has little effect on the solution.

To gauge the importance of $\frac{\partial \phi}{\partial v}$ on the solution, a rectangular hydrofoil at $\alpha = 3^\circ$

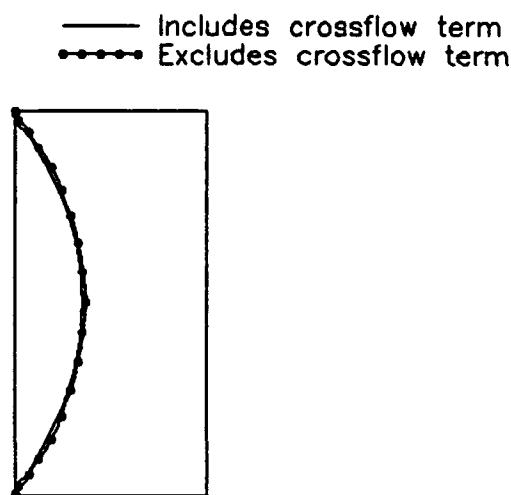


Figure 4-12: Convergence of the cavity planform with updating of the crossflow terms. Rectangular hydrofoil at $\alpha = 3^\circ$, $\sigma = 0.5$, $\frac{l_0(\psi)}{c(\psi)} = .014$.

is tested for $\sigma = 0.5$ with and without inclusion of the crossflow terms. The results are shown in Figure 4-12. Since this example shows only partial cavitation, it can be seen that $\frac{\partial \phi}{\partial \psi}$ also has a negligible effect on the solution, since the two cavity planforms are nearly indistinguishable.

The third geometry is a modified AO-177 propeller (identical to the AO-177, except that the skew is zero), and its geometry is given in Table 4.1. For the propeller solution, the crossflow term has a more marked effect on the cavity planform, although the convergence is still very quick. Shown in Figure 4-13 are cavity planforms on the test propeller geometry for consecutive crossflow iterations.

4.2.5 Nonlinear Effect of Foil Thickness

The nonlinear effect of foil thickness on cavity extent in two-dimensional partially cavitating flows is well known. Namely, increasing the foil thickness for given angle of attack and cavitation number has the effect of *decreasing* the cavity extent, as has been shown by several researchers [34, 69, 72]. The present method has also been found to manifest the nonlinear thickness effect on the shape of the cavity for 2-D flows [36]. A similar behavior has also been found for 3-D flows. This is shown in

$\frac{r}{R}$	$\frac{P}{D}$	$\frac{\text{rake}}{D}$	skew(°)	$\frac{C}{D}$	$\frac{I_{\text{max}}}{C}$	$\frac{t_{\text{max}}}{C}$
0.20	1.125	0.0000	0.0	0.2070	0.0490	0.0414
0.30	1.223	0.0058	0.0	0.2456	0.0444	0.0399
0.40	1.288	0.0210	0.0	0.2722	0.0367	0.0361
0.50	1.318	0.0410	0.0	0.2817	0.0314	0.0304
0.60	1.309	0.0650	0.0	0.2684	0.0300	0.0236
0.70	1.250	0.0913	0.0	0.2320	0.0295	0.0166
0.80	1.140	0.1090	0.0	0.1815	0.0281	0.0107
0.90	0.970	0.1168	0.0	0.1180	0.0263	0.0059
0.95	0.857	0.1170	0.0	0.0810	0.0252	0.0038
1.00	0.722	0.1148	0.0	0.0010	0.0000	0.0015

Table 4.1: Test propeller geometry, identical to the AO-177 propeller, except the skew is zero.

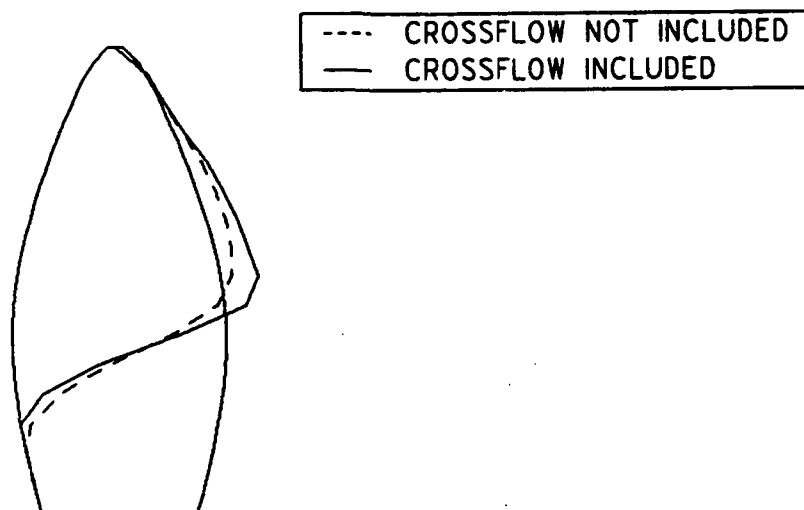


Figure 4-13: Convergence of the cavity length with updating of the crossflow terms for a test propeller.

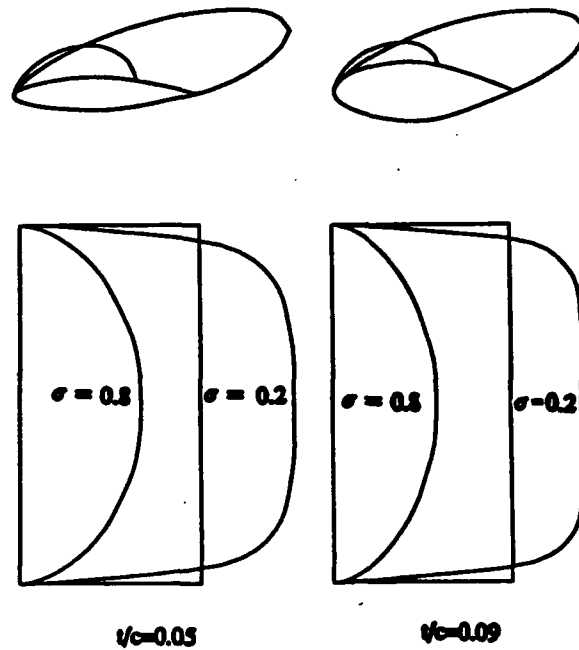


Figure 4-14: Nonlinear effect of foil thickness on cavity extent and volume. Cavity planforms and shapes at midspan are shown for rectangular hydrofoils, $\alpha = 5^\circ$, Aspect Ratio $AR = 5.0$, $t/c = .05, .09$ (span and chord are not drawn to scale).

Figure 4-14 where the cavity planforms and shapes at midspan are shown for two rectangular hydrofoils at two cavitation numbers. Both hydrofoils have an aspect-ratio of 5, zero camber, and a NACA65a thickness section the maximum thickness of which varies elliptically to zero in the spanwise direction. Both foils are at an angle of attack $\alpha = 5^\circ$. The first has a thickness-to-chord ratio at midspan $t/c = .05$ and the second has $t/c = .09$. A smaller cavity (in volume and extent at all spanwise locations) is predicted for the thicker foil at the same cavitation number. The effect of foil thickness on cavity size appears to be less pronounced in the case of supercavities. This has also been found to be the case for two dimensional flows.

4.3 The Effect of ϕ_0 on the Solution

The quantity ϕ_0 is the value of the potential at the leading edge of the cavity. It is not a primary variable because it is defined at a panel edge rather than at the control point. Nonetheless, it is an unknown in the system of equations and it is important to the solution. Mainly, it is important for ϕ_0 to be relatively independent of gridding so that the solution will converge with number of panels. The consequence of having a grid dependent definition is shown in this section.

ϕ_0 was first defined as a quadratic extrapolation of the unknown potentials at the three control points in front of the cavity leading edge (see Figure 3-5 for clarification). Figure 4-15 shows the resulting convergence characteristics of $\delta(y)$ for a 3-D rectangular hydrofoil and a guess of the cavity planform. $\delta(y)$ is not zero because the planform is not correct. The rectangular hydrofoil is 5% thick at the midspan, tapering elliptically to zero thickness at the tip. The angle of attack is $\alpha = 3^\circ$ and the cavity length is $\frac{l}{c}(y) = 0.5$ for all y . Computations were made for panel arrangements of $(N, M) = (60, 30), (80, 30), (100, 30)$ and $(120, 30)$.

The convergence of $\delta(y)$ with number of panels is seen to be rather slow. This was found to improve drastically when a cubic extrapolation is used (see equation (3.11)) which includes a condition on the slope of $\phi(s)$ at the cavity leading edge. The resulting $\delta(y)$ convergence is shown in Figure 4-16.

4.4 Time-Marching Scheme

The time marching scheme is identical to that used in the fully wetted solution, and is described in detail in [22]. The main features of the scheme will be outlined here for the sake of completeness.

Time is discretized into equal increments of span Δt . During one time step, each propeller blade rotates through an incremental angle $\Delta\theta = \omega\Delta t$. At each time step, the solution is found for the key blade only, while the singularities on the other blades are assumed to be known. Before proceeding to the next time step, vorticity is shed

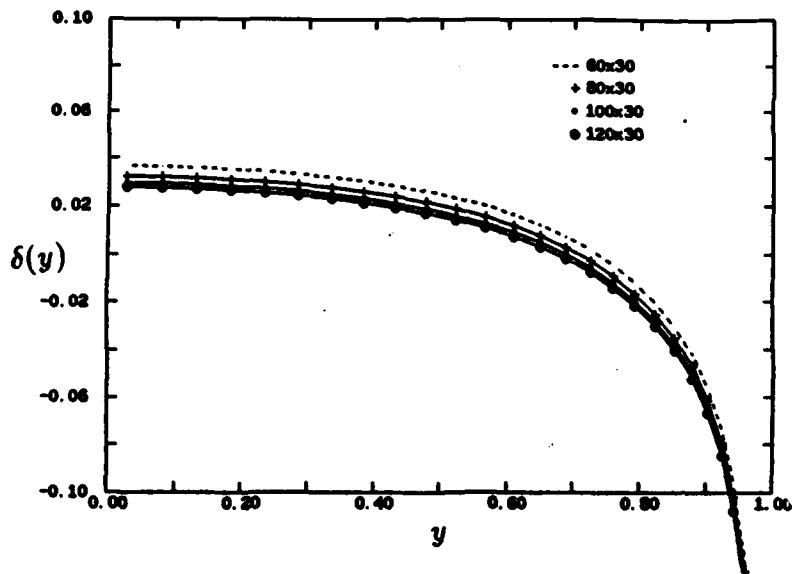


Figure 4-15: $\delta(y)$ for a rectangular foil at $\alpha = 4^\circ$ and $\sigma = .16$ with a cavity length $\frac{l}{c}(y) = 0.5$ for all y . In this case ϕ_0 is defined as a quadratic extrapolation.

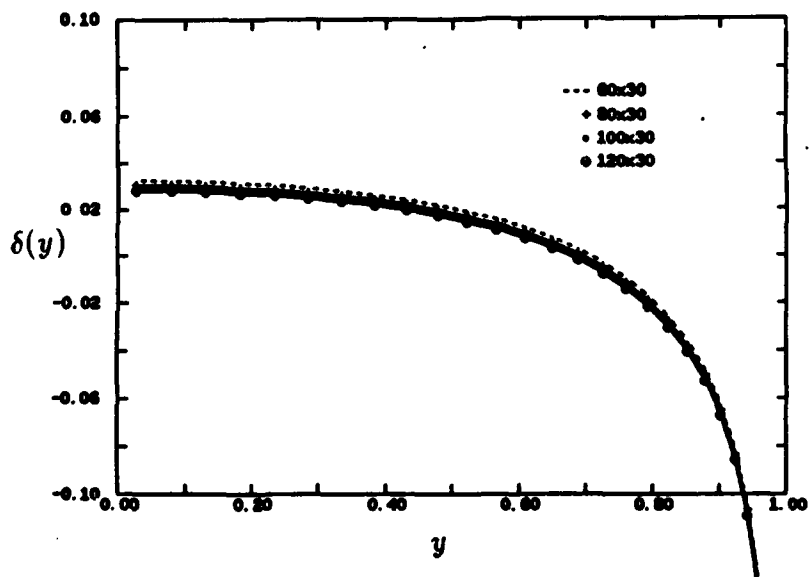


Figure 4-16: $\delta(y)$ for a rectangular foil at $\alpha = 4^\circ$ and $\sigma = .16$ with a cavity length $\frac{l}{c}(y) = 0.5$ for all y . In this case, ϕ_0 is defined as a cubic extrapolation with specified slope at the cavity leading edge.

downstream along the assumed wake surface through an angular distance equal to the incremental rotation $\Delta\theta$. This enforces the equality of the strength of the shed vorticity and the time rate of change of the circulation on the blade. The strength of the circulation is given in terms of the potential jump at the trailing edge of the blade

$$\Gamma(r, t) = \Delta\phi_T(r, t) = \phi_T^+(r, t) - \phi_T^-(r, t) = \phi_{Nm} - \phi_{1m}.$$

and the potential jump at the first wake panel is given by

$$\Delta\phi(r, t) = \frac{\Gamma(t) + \Gamma(t - \Delta t)}{2}. \quad (4.14)$$

Thus, the vorticity convection is used to define the wake dipole strengths. Although this an extension of Morino's Kutta condition in steady flow, it is not equivalent to the Kutta condition he applied in unsteady flow [52].

The solution is initiated by the fully wetted *steady* solution. Next, the fully wetted *unsteady* solution is obtained, which then serves as the "initial guess" for the unsteady cavity solution. The unsteady cavity solution is turned on when the key blade is at the 6 O'Clock position, so that it is likely to start out fully wetted. This was found to be an important time-saving measure in the linear solution by Lee [45]. The singularity strengths on the other blades and their wakes are taken from earlier key blade solutions. During the first revolution of the key blade, the singularities on another blade are taken either from the fully wetted solution or from the cavity solution when the key blade was in the same angular position. For subsequent revolutions, the other blade singularities are taken from previous cavity solutions when the key blade was in the same angular position.

4.5 Treatment of the Unsteady Terms

The dynamic and kinematic boundary conditions (2.17), (2.19), (2.23) and (2.30), include time derivatives of the potential and cavity thickness. The numerical treatment of these terms will be described in this section.

The dynamic boundary condition (2.17) expresses ϕ as a function of, among other things, the time derivative $\frac{\partial \phi}{\partial t}$. At a given time step, $\frac{\partial \phi}{\partial t}$ is assumed to be known and given by a quadratic extrapolation of its values from previous time steps. Specifically, the derivative is assumed to behave locally quadratically in time

$$\frac{\partial \phi}{\partial t}(t) \sim At^2 + Bt + C$$

and the coefficients A, B, C are defined in terms of the values of $\frac{\partial \phi}{\partial t}$ at the three previous time steps. The time derivative at the current time step is then extrapolated forward according to

$$\frac{\partial \phi}{\partial t}(t) = 3\frac{\partial \phi}{\partial t}(t - \Delta t) - 3\frac{\partial \phi}{\partial t}(t - 2\Delta t) + 8\frac{\partial \phi}{\partial t}(t - 3\Delta t)$$

The derivative at each time step is computed numerically via a backwards fourth-order accurate finite difference scheme³. The extrapolation of $\frac{\partial \phi}{\partial t}$ fits well with the time marching scheme, since several revolutions are required to obtain the steady-state oscillatory solution due to the time lag of the solution on the other blades. The convergence of the solution with revolutions is discussed in section 5.1.

In the kinematic boundary conditions (2.23) and (2.30), the time derivatives of the cavity thickness, $\frac{\partial h}{\partial t}$ and $\frac{\partial h_m}{\partial t}$, are replaced by first order backwards finite differences (see section 4.1.3). These do not require any further special treatment. These boundary conditions are used to compute the cavity thickness, after the solution at the current time step has been found and the source strengths are known. In addition, however, these terms must be used to determine the strength of a source panel which is wetted at the current time step, but which was cavitating during the previous time step. In other words, a collapsing cavity has an *additional* sink on the panels which lie between the trailing edge of the cavities from consecutive time steps. This was

³Various finite difference schemes have been tried for the computation of the fully wetted unsteady pressure distribution and the fourth order finite difference model was chosen for reasons of robustness [22].

first noticed by Van Houten [73]. The magnitude of the source will be given as

$$\frac{\partial \phi}{\partial n} = -U_n + \frac{\partial h}{\partial t}. \quad (4.15)$$

In order to understand the importance of the unsteady terms of the boundary conditions, an unsteady two dimensional model of a partially cavitating hydrofoil was investigated, wherein the cavitation number is allowed to vary harmonically ($\sigma(t) = \sigma_0 + \sigma_g \cos \omega t$) while the inflow is steady and uniform and the wake is steady (no shed vorticity, but the wake dipole strength changes each time step). Although this model is not an adequate model of the physical flow, it allows us to see the relative effects of the various unsteady terms on the global 2-D solution. To this end, the time history of the cavity length was computed for a NACA16006 foil operating at an angle of attack of 4° and with a time-dependent cavitation number equal to $\sigma(t) = 1.2 + 0.2 \cos \omega t$ at a reduced frequency of $k = \frac{\omega c}{2U} = 1.0$. Figure 4-17 shows the cavity length as a function of ωt for one cycle for two different solutions. The first solution contains no history at all; the time derivatives of both the potential and the cavity thickness are set to zero. The second solution contains the unsteady terms. Note that the unsteady solution is shifted to the right, indicating that the growth stage lasts longer than the collapse stage, a well known characteristic of unsteady cavitation [73, 66].

Figure 4-18 shows cavity shapes from several time steps during the second cycle of the unsteady solution. Of particular interest is the difference between the cavity shapes at $\omega t = 90^\circ$ and $\omega t = 270^\circ$ for which *the cavitation numbers are identical*. The difference between the shapes is due entirely to the unsteady terms. This shows the importance of the unsteady terms.

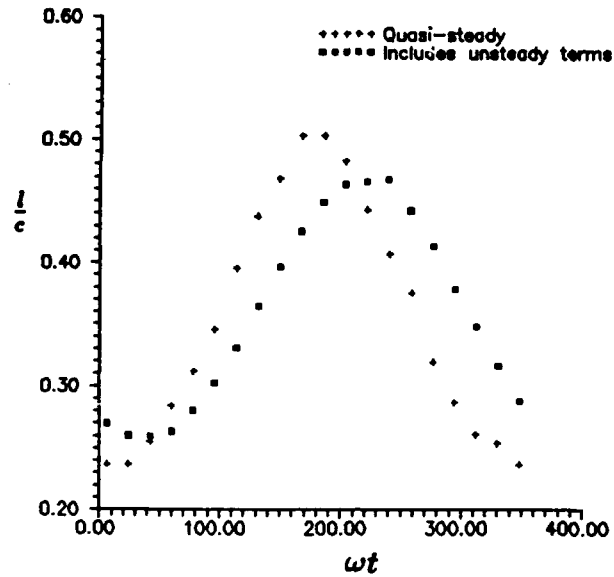


Figure 4-17: Cavity length vs ωt for a NACA16006 2-D section at $\alpha = 4^\circ$ and $\sigma(t) = 1.2 + 0.2 \cos \omega t$. Shown are the quasi-steady and the unsteady solutions.

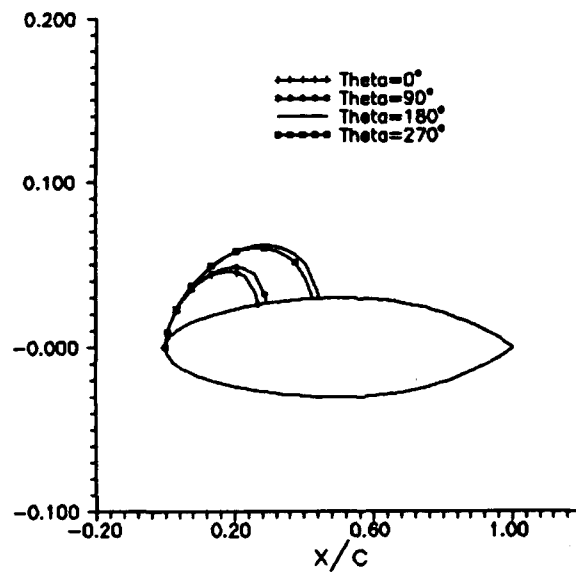


Figure 4-18: Cavity shapes from several time steps of the unsteady solution shown in the previous figure.

Chapter 5

Numerical Validation

The goal of this chapter is to show the present method to be convergent and consistent, as all viable numerical methods must be. Here, a convergent solution implies that as the number of panels tends to infinity and the average panel size tends to zero the solution would converge to an answer which is exact for the given assumptions. A consistency test is applied to test the accuracy of the solution. Comparison is made between the results of the present theory with results of linear theory and linear theory with leading edge corrections. Some comparisons are made to published experimental results and observations.

5.1 Convergence

Figure 5-1 shows convergence of the spanwise δ distribution and chordwise cavity thicknesses for a rectangular hydrofoil and a guess of the cavity planform $l = 0.5$ at all spanwise strips. This was the initial convergence test and eliminates the effects of the split-panel method ($l = 0.5$ always corresponds to a panel boundary with cosine spaced panels) and the δ -tolerance associated with the planform convergence scheme. The hydrofoil has a NACA65a crosssection with $\frac{t}{c} = .05$ at the midspan, tapering elliptically to zero at the foil tips. The foil is twisted so that the angle of attack is lower at the tips than at the midspan; the twist angle, in degrees, is given by $\alpha_t(y) = 8y^3 - 12y^2$. The detachment point is 2.4% of the local chord length aft of the leading edge at each spanwise strip. The aspect ratio is $AR = 5.9$, the cavitation

number is $\sigma = 0.4$ and the angle of attack is $\alpha = 4^\circ$. Figure 5-1 displays excellent convergence characteristics for these variables under these conditions.

Figure 5-2 shows the convergence of the cavity planform and the cavity volume with number of panels for the same rectangular hydrofoil used in the previous example, except that in this case the twist angle α_t is zero everywhere. This convergence test is more demanding than the previous because of the use of the split panel method, which introduces some error into the computation. The angle of attack is 3° and the cavitation number is 0.12. The chordwise discretization is varied from 60 to 120 with the spanwise discretization fixed at 20. With the chordwise discretization fixed at 80, the spanwise discretization is varied from 20 to 30. In each case, the wake is divided into 60 panels, with 40 in the near wake, which extends one half-span downstream, and 20 in the far wake, which extends an additional 9 half-spans. From these results, it can be concluded that a foil discretization of 80×20 is sufficient to obtain a converged result for the rectangular hydrofoil.

The next task is to test the convergence characteristics of the propeller solution. Figure 5-3 shows convergence of the cavity planform and cavity thickness on a test propeller which is a N4381 geometry with modified pitch distribution. The modified N4381 has an unloaded tip in order to ensure that the blades do not supercavitate near the tip, so that the convergence characteristics of the partial cavitation solution may be investigated. The propeller geometry is given in Table 5.1. First, the method is applied to the test propeller with a single blade operating in a uniform inflow with advance coefficient $J_S = V_S/(nD) = 0.8$, where V_S is the ship speed, and $\sigma_n = 2.7$. The variation in hydrostatic pressure is ignored and the resulting solution is steady. The cavity is assumed to detach 2.4% of the local chord length aft of the leading edge. Results of this convergence test show that a blade discretization of 80×20 is sufficient to obtain a converged result in steady flow for the partially cavitating test propeller.

The convergence of a supercavitating propeller is tested next. Shown in Figure 5-4 is the steady cavity solution on a single bladed version of the AO-177 propeller at $J_S = 0.6$ and $\sigma_n = 2.5$. The AO-177 propeller geometry is provided in Table 5.2.

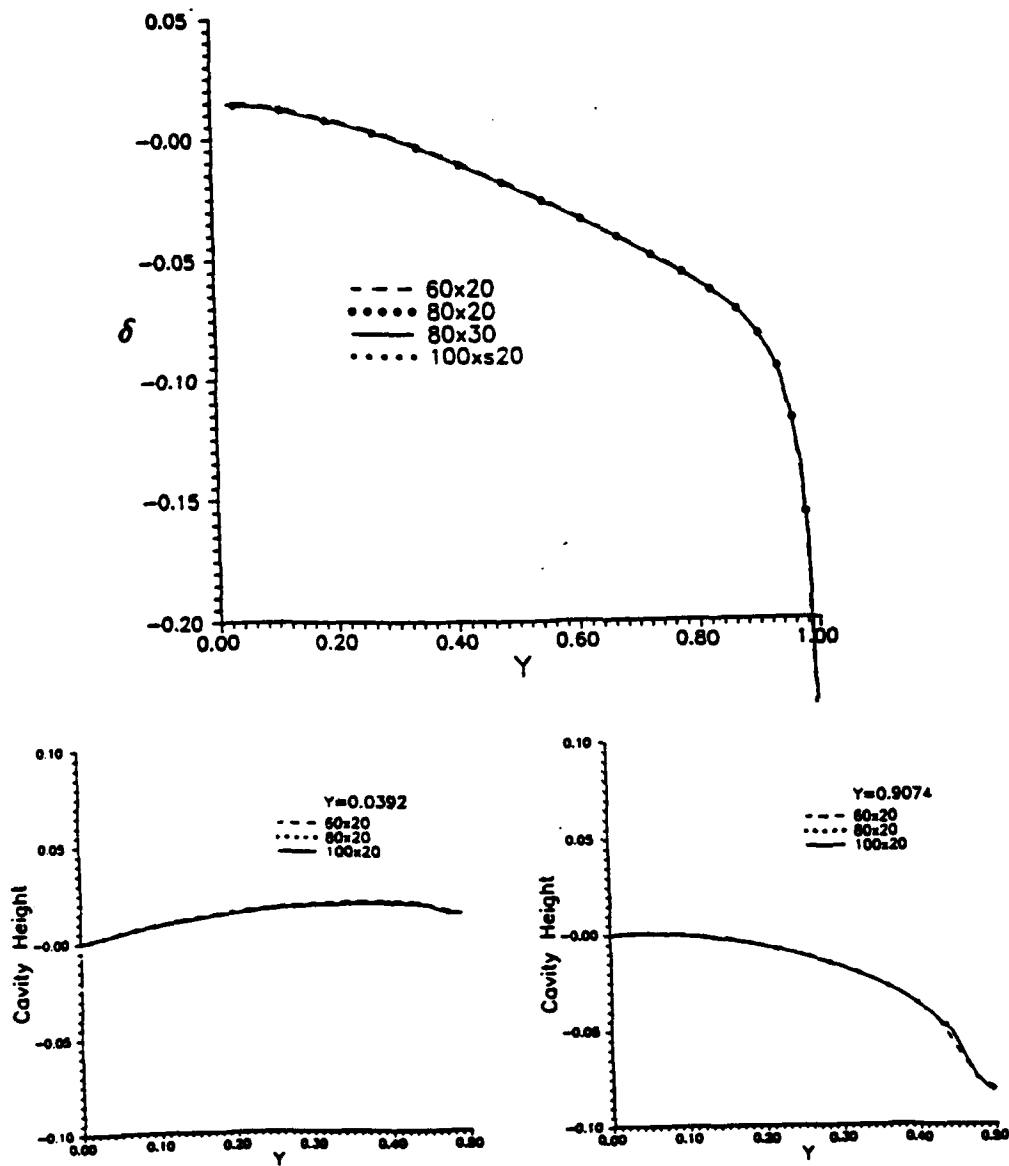


Figure 5-1: Convergence of spanwise and chordwise cavity thickness distributions with number of panels. The foil and cavity characteristics are described in the text.

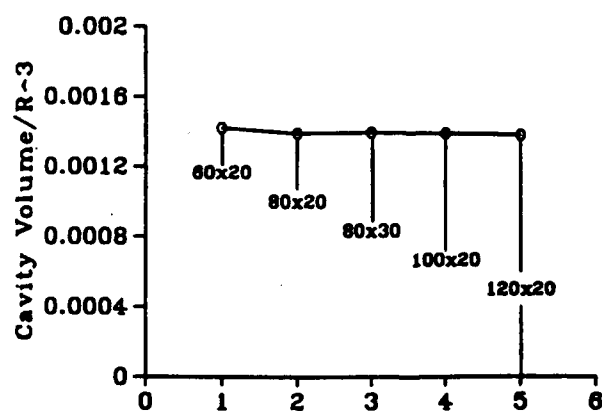
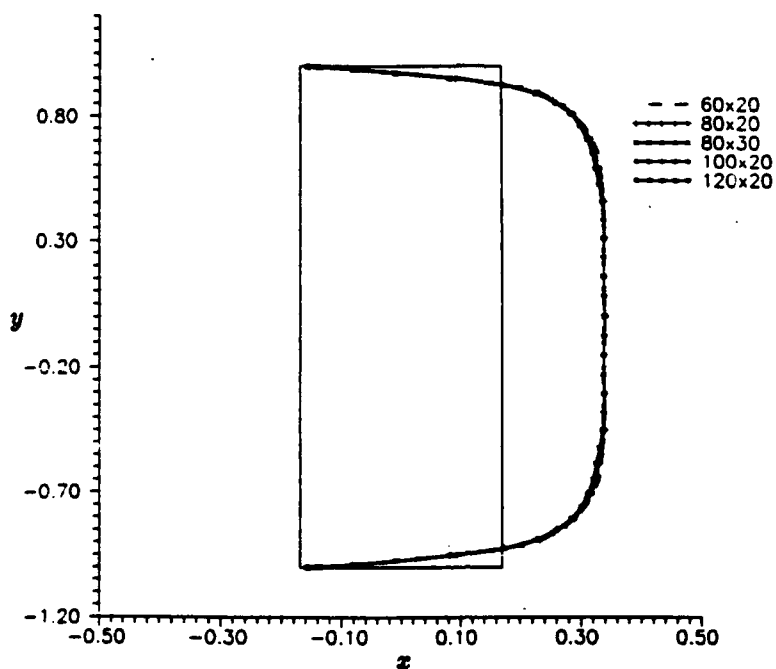


Figure 5-2: Convergence of cavity planform (top plot) and cavity volume (bottom plot) with number of panels.

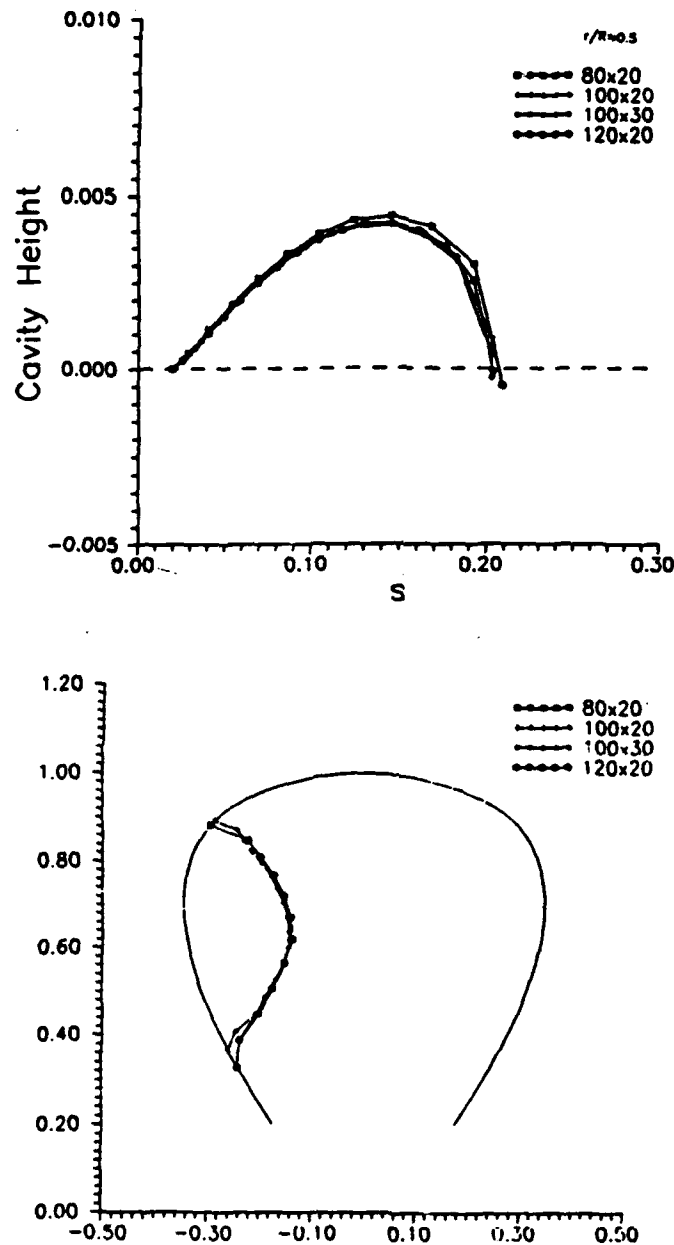


Figure 5-3: Convergence of cavity planform and cavity thicknesses with number of panels for the modified N4381 one-bladed propeller in steady flow; $J_S = 0.8$, $\sigma_n = 2.7$. The cavity detaches 2.4% of the local chord length aft of the leading edge at all spanwise locations.

$\frac{r}{R}$	$\frac{P}{D}$	$\frac{\text{rake}}{D}$	skew($^{\circ}$)	$\frac{C}{D}$	$\frac{I_{\text{max}}}{C}$	$\frac{I_{\text{max}}}{C}$
0.20	1.332	0.0	0.0	0.174	0.0351	0.0651
0.25	1.338	0.0	0.0	0.202	0.0369	0.0594
0.30	1.345	0.0	0.0	0.229	0.0368	0.0537
0.40	1.358	0.0	0.0	0.275	0.0348	0.0441
0.50	1.350	0.0	0.0	0.312	0.0307	0.0360
0.60	1.310	0.0	0.0	0.337	0.0245	0.0286
0.70	1.250	0.0	0.0	0.347	0.0191	0.0219
0.80	1.150	0.0	0.0	0.334	0.0148	0.0157
0.90	0.950	0.0	0.0	0.280	0.0123	0.0101
0.95	0.750	0.0	0.0	0.210	0.0128	0.0072
1.00	0.500	0.0	0.0	0.000	0.0120	0.0044

Table 5.1: The DTMB propeller N4381, with modified pitch distribution to unload the tip (referred to in the text as the "test propeller").

In this case, the cavity is assumed to detach at the blade leading edge. To find the planform, the trailing edge openness δ is required to converge to zero everywhere except at the two outermost strips, for $r/R \geq .98$. As mentioned, the converged planform is difficult to obtain near the tip due to inaccurate modelling of the geometry (see discussion in section 4.2.3). However, in most cases $\delta(r)$ converges to less than 10% of the tip chord length (which is usually less than 5% of the blade diameter). In contrast, the tolerance set for δ_m for $r/R < .98$ in this example was $\delta_{\text{tol}} = .001$.

Next, the test propeller is run in a nonuniform inflow which is characterized by a 15% dent in the axial inflow, symmetric about $\theta = 0$ (see equation (2.2) for a definition of the inflow velocity). The other components of the flow are zero. Due to the circumferential symmetry, all of the harmonic coefficients of the sine series for the axial flow are zero ($B_n = 0 \forall n$). The mean axial velocity is set to one ($A_1(r) = 1$). The coefficients of the cosine series are given in Table 5.3.

The circumferential distribution of axial inflow velocity is shown in Figure 5-5. Also shown in this figure are convergence with revolutions and convergence with time step size of the cavity volume history.

$\frac{r}{R}$	$\frac{P}{D}$	$\frac{\text{rake}}{D}$	skew($^{\circ}$)	$\frac{C}{D}$	$\frac{I_{\text{max}}}{C}$	$\frac{I_{\text{min}}}{C}$
0.20	1.125	0.0000	0.0	0.2070	0.0490	0.0414
0.30	1.223	0.0058	2.2	0.2456	0.0444	0.0399
0.40	1.288	0.0210	7.1	0.2722	0.0367	0.0361
0.50	1.318	0.0410	13.1	0.2817	0.0314	0.0304
0.60	1.309	0.0650	20.0	0.2684	0.0300	0.0236
0.70	1.250	0.0913	27.7	0.2320	0.0295	0.0166
0.80	1.140	0.1090	34.5	0.1815	0.0281	0.0107
0.90	0.970	0.1168	40.3	0.1180	0.0263	0.0059
0.95	0.857	0.1170	42.79	0.0810	0.0252	0.0038
1.00	0.722	0.1148	45.0	0.0010	0.0000	0.0015

Table 5.2: The AO-177 propeller geometry.

n	A_n	n	A_n
1	1.0	9	0.0000
2	-.0360	10	0.0009
3	-.0318	11	0.0009
4	-.0257	12	0.0005
5	-.0187	13	0.0000
6	-.0120	14	-.0003
7	-.0064	15	-.0003
8	-.0023	16	-.0002

Table 5.3: Harmonic coefficients A_n for the nonuniform axial inflow velocity.

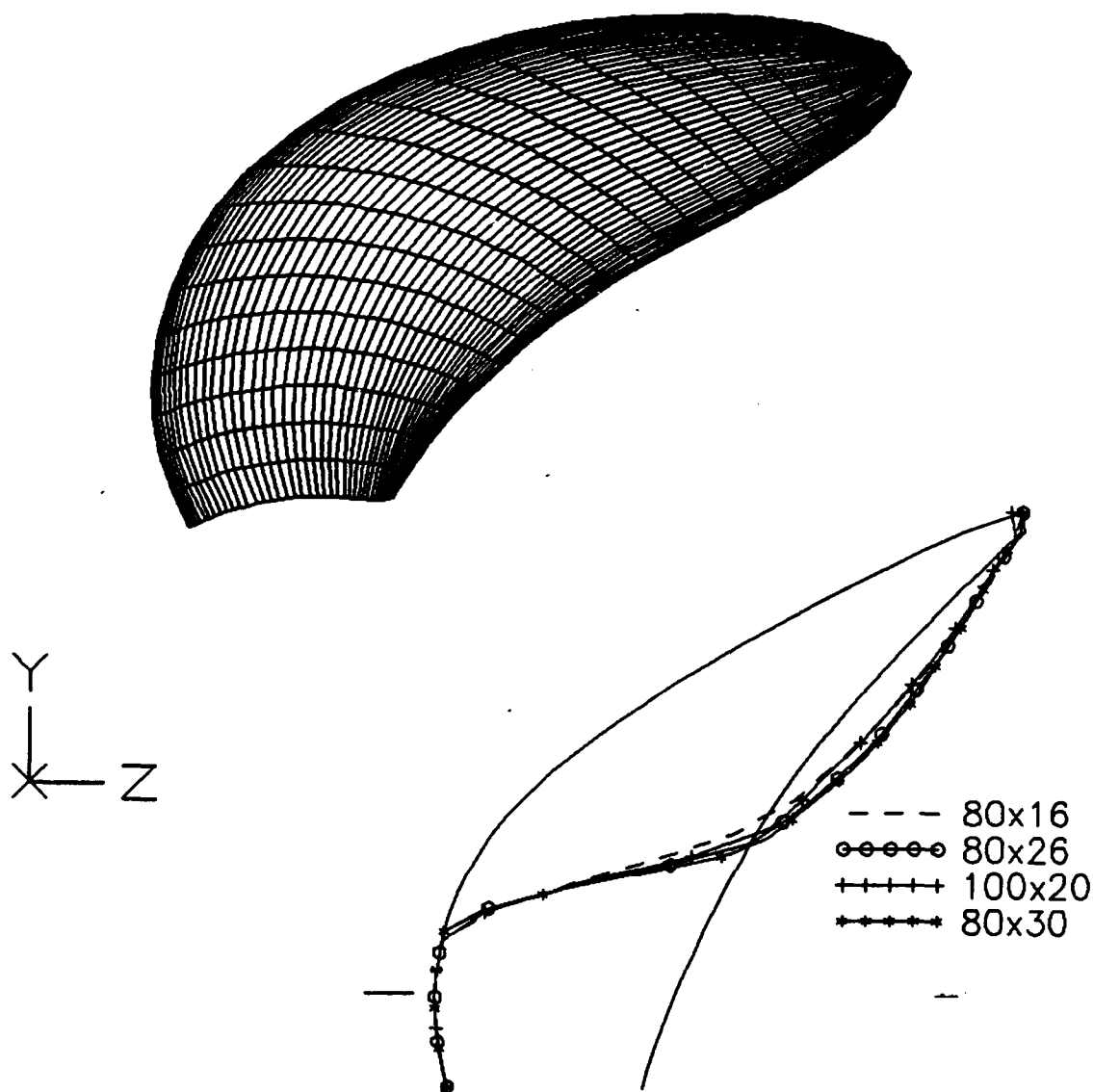


Figure 5-4: Convergence of cavity planform with number of panels for the one-bladed AO-177 propeller in steady flow; $J_S = 0.6$, $\sigma_n = 2.5$. Shown also is the discretized blade for $(N, M) = (100, 20)$.

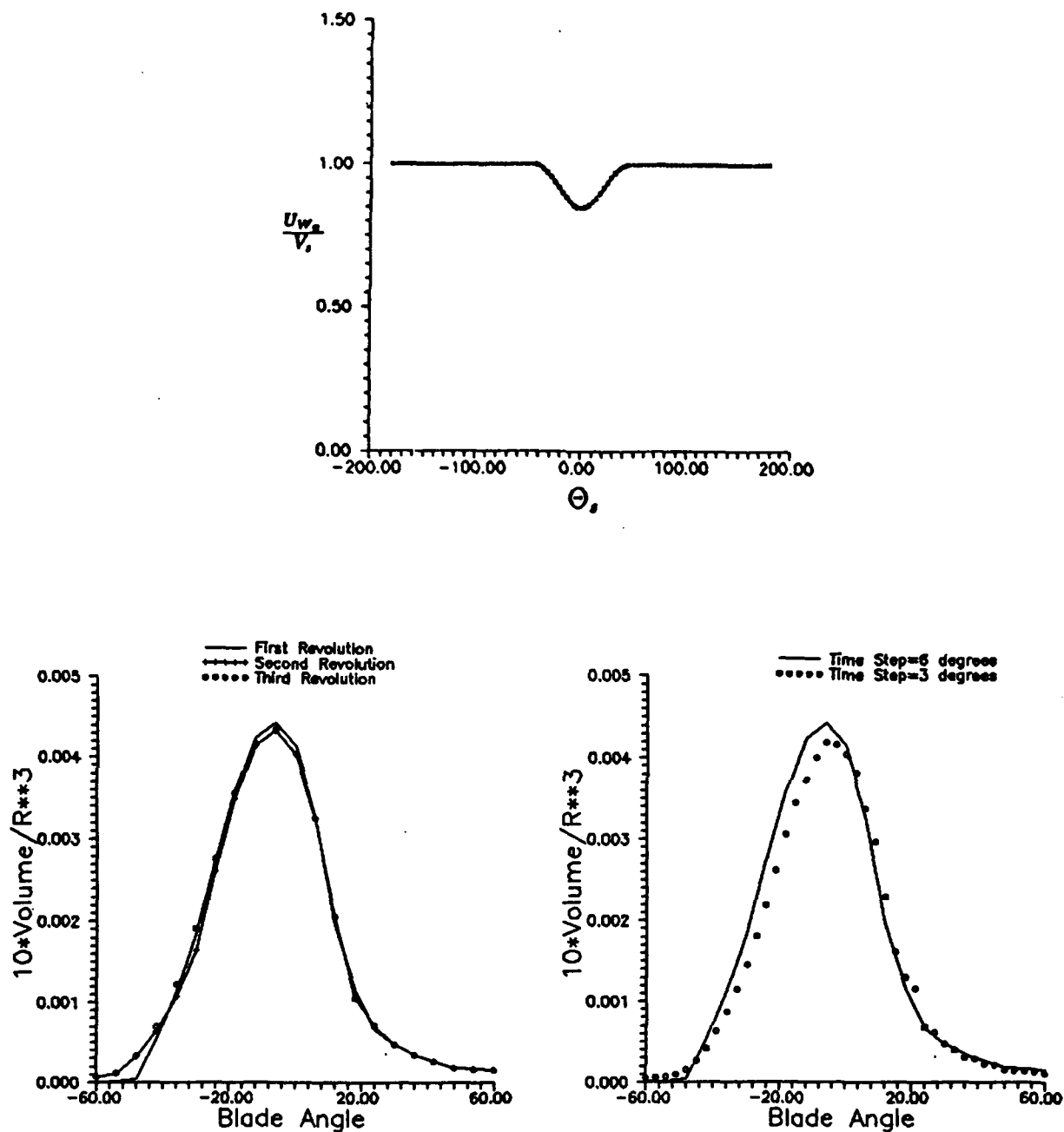


Figure 5-5: Convergence, with revolutions and with time step size, of cavity volume history for the one-bladed test propeller operating in a nonuniform axial inflow. The axial inflow is shown at the top of the figure.

5.2 Consistency

5.2.1 Fully Wetted Consistency Test

One very useful consistency test consists of replacing the dynamic boundary condition (3.9) with

$$\begin{aligned}\phi_{(N_{LB}+n)m} &= \phi_{fw} & n &= 1, \dots, N_{CAV_m} + N_{C_m} \\ & & m &= 1, \dots, M\end{aligned}\tag{5.1}$$

where ϕ_{fw} is the potential from the fully wetted solution. The resulting solution should be equivalent to the fully wetted solution (i.e., the cavity thickness should be zero everywhere and the resulting circulation distribution should be equivalent to the fully wetted circulation). As a test of self-consistency, this tool was very useful for de-bugging the computer code. The first check of any code was to apply this consistency test.

Figure 5-6 shows the results of the fully wetted consistency test for the N4381 test propeller in *steady flow*. Shown in the figure are the circulation distributions from the fully wetted solution and the cavity solution (with the dynamic boundary condition replaced with (5.1)). The two circulation distributions are very nearly identical, with the slight discrepancy near the tip perhaps attributable to the different tolerances set on the iterative matrix solutions. This discrepancy is considered negligible.

5.2.2 Pressure Validation

To validate the solution, a modified geometry is created by combining the cavity and foil (or blade) to form a single surface and representing the resulting surface by a lattice of quadrilateral panels. The grid is adapted to the shape of the cavity so that panels are clustered around the cavity trailing edge. The fully wetted flow is then computed about the modified foil and the resulting pressure distribution is compared to the pressure from the cavity solution. If the cavity shape is the correct shape which corresponds to the applied dynamic boundary condition, then the two pressure distributions will match. For example, if the solution were the *fully nonlinear*

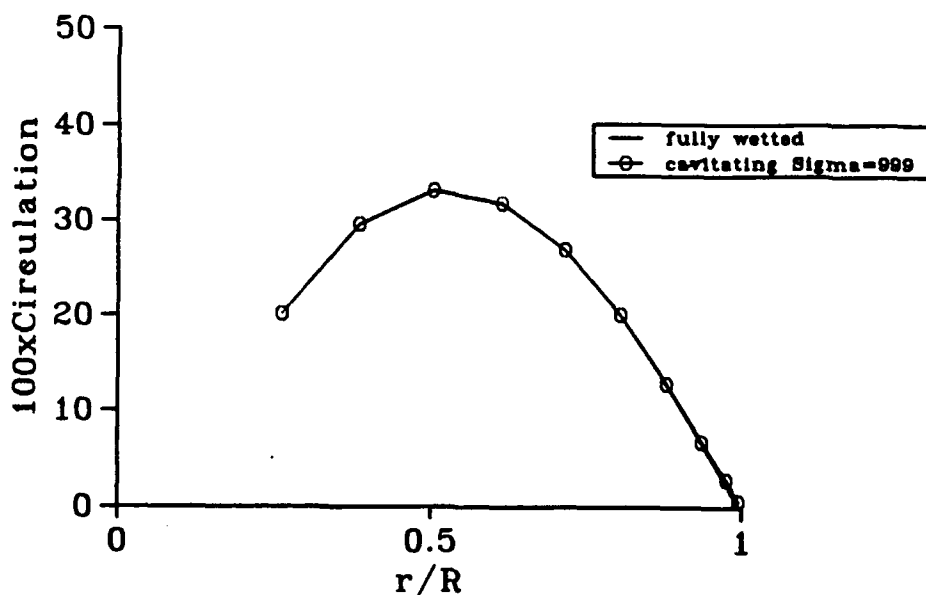


Figure 5-6: Results of a fully wetted consistency test. Circulation distributions from the fully wetted solution and the cavity solution. The two distributions should match because the potential on the cavity panels is set equal to the fully wetted potential.

solution, then the pressures should match exactly. The discrepancy between the two pressure distributions is therefore a measure of the error introduced by applying the boundary conditions on the approximate surface. This test will be referred to as *pressure validation*, and will be shown for several configurations.

3-D Partially Cavitating Hydrofoil

Figures 5-8 and 5-9 show the results of a pressure validation test for a partially cavitating rectangular hydrofoil which is the same as the foil shown in Figure 5-1 (including the angle of twist which tends to eliminate tip cavitation). An example of an adapted grid on which the fully wetted flow is computed is shown in Figure 5-7. In Figure 5-8 the angle of attack is $\alpha = 3^\circ$ and $\frac{a}{c} = .105$, while in Figure 5-9 the angle of attack is $\alpha = 5^\circ$ for the same $\frac{a}{c}$. For the smaller of the two angles of attack, the comparison between the fully wetted pressure and the cavity pressure is excellent at all spanwise strips. For the higher angle, however, the comparison deteriorates. This indicates that the shape of the cavity from the first iteration is further from the correct nonlinear shape for higher angles of attack. This is not surprising. However, the results in 2-D, discussed extensively in Appendix B, show that the difference between

the first iteration and converged cavity lengths and volumes is not substantial, even at moderately high angles of attack. In other words, from my experience in applying the same validation test in 2-D, the pressure distributions from the first iteration and the converged solution differ more than the corresponding cavity lengths and shapes.

3-D Supercavitating Hydrofoil

Figure 5-10 shows pressure validation for an elliptic hydrofoil (the chord length is maximum at the midspan, tapering elliptically to zero at the tip) at $\alpha = 3^\circ$ and $\frac{a}{c} = 0.33$. The aspect ratio is $AR = 1.27$. In general, this comparison is very good everywhere except very close to the tip. For the foil strips beyond $y = .98R$, the planform was not required to converge to zero- δ , although it came very close. The difficulty in finding the correct planform near the tip would be mitigated by the inclusion of the tip vortex in the model. This will be discussed further in Chapter 6.

One-bladed Test Propeller in Steady Flow

Figure 5-11 shows pressure validation for the test propeller in steady flow¹ at $r/R = .75$. The advance coefficient is $J_s = 0.8$ and the cavitation number is $\sigma_n = 2.7$. For these conditions, the pressure validation shows that the first iteration propeller solution does a good job of predicting the correct nonlinear cavity shape at this advance coefficient.

5.2.3 Comparison to PUF-3A

Figure 5-12 shows a comparison between the cavity planform computed by the present method (labeled PROPCAV, which is the name of the program) and those computed by linear theory and linear theory with leading edge corrections (labeled PUF-3A [31, 34]). The computations are done for steady flow conditions on the one-bladed modified N4381 test propeller. Linear theory is seen to overpredict the cavity extent,

¹The pressure validation test is not applied to the unsteady case due to the excessive computation times that would require.

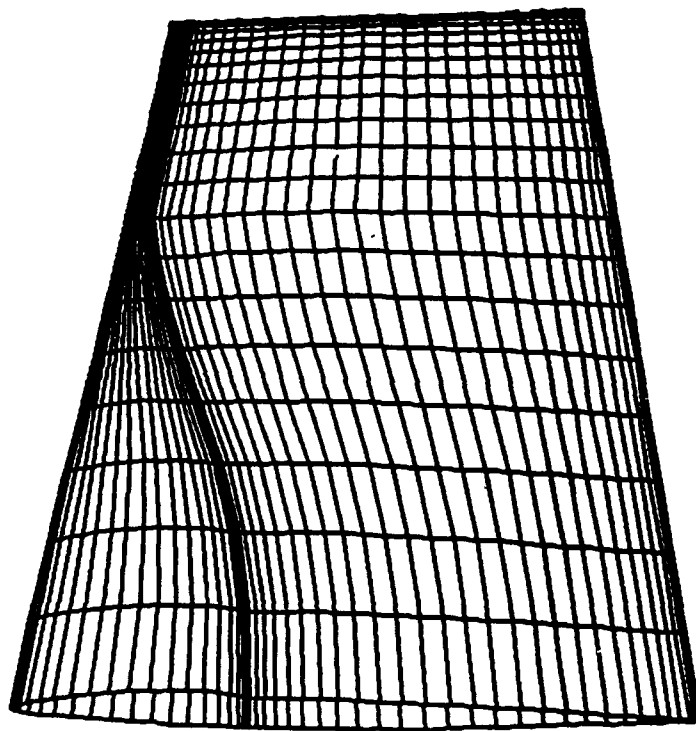


Figure 5-7: Adapted grid fit to the shape of the cavity, used to compute the fully wetted flow on the modified foil/cavity boundary for the pressure validation shown in the next figure.

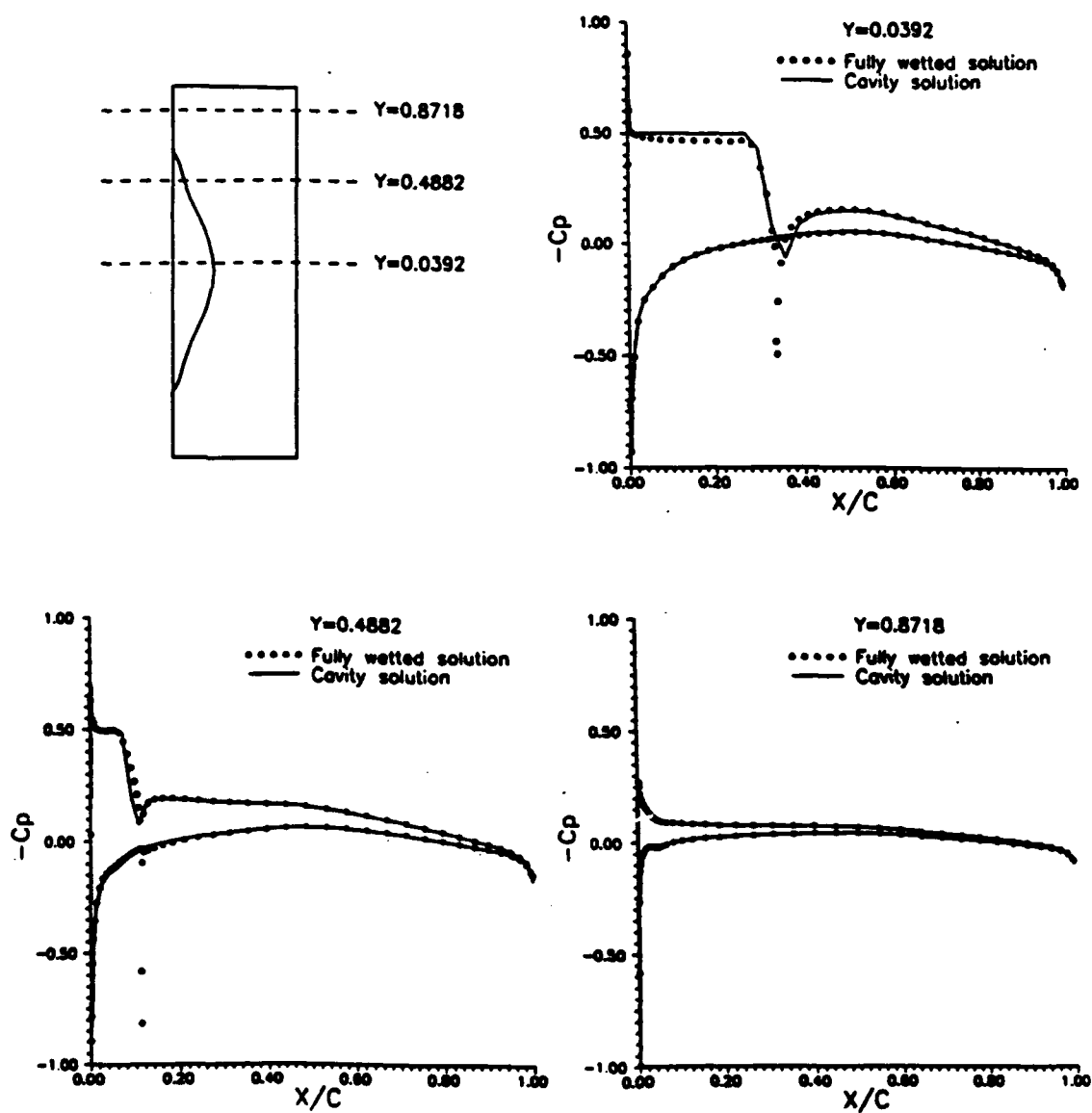


Figure 5-8: Pressure validation for a rectangular hydrofoil at $\alpha = 3^\circ$ and $\frac{a}{c} = .105$. The cavity detaches at .4% of the chord length aft of the leading edge at all spanwise strips.

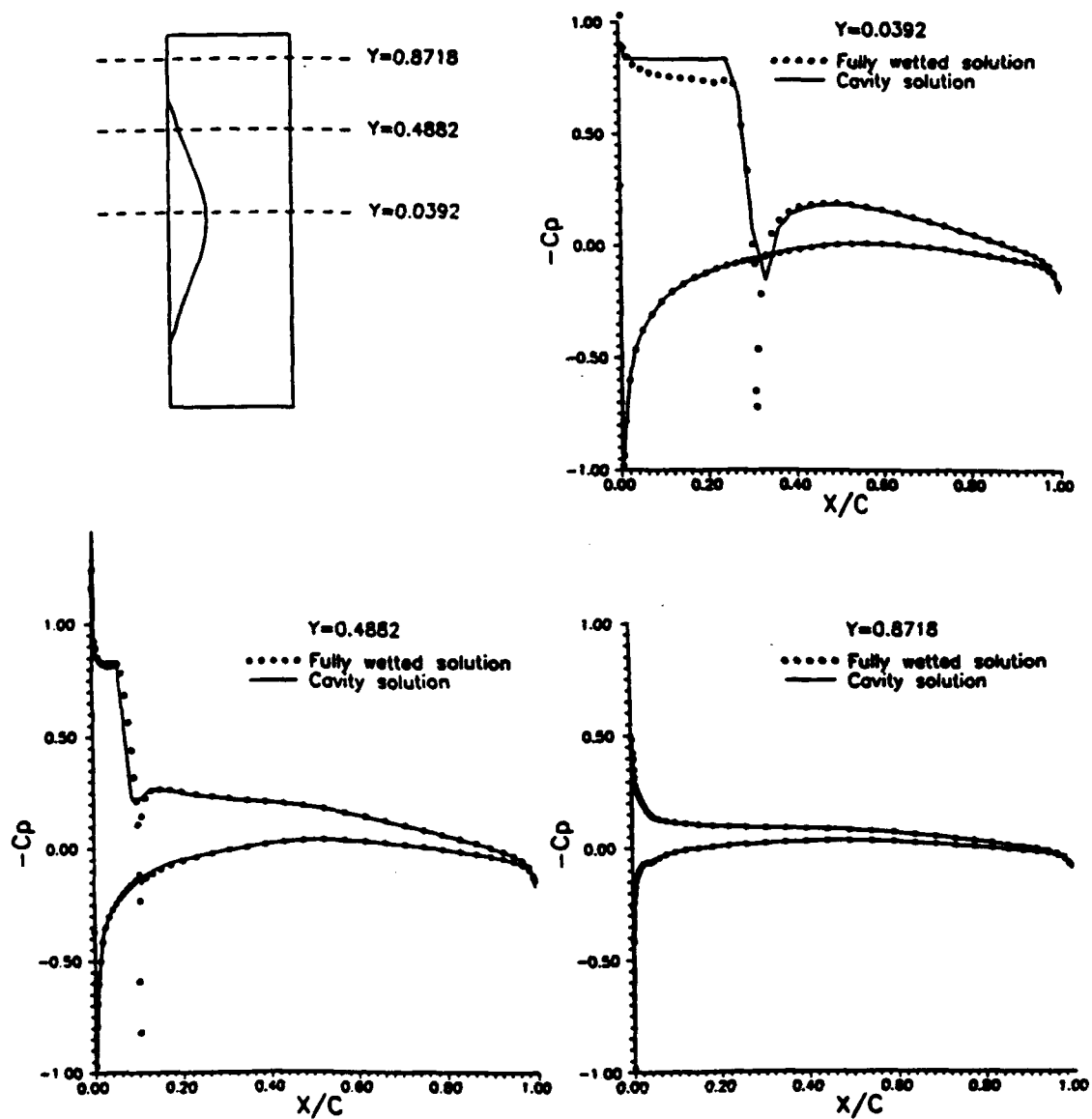


Figure 5-9: Pressure validation for a rectangular hydrofoil at $\alpha = 5^\circ$ and $\frac{\sigma}{\rho} = .105$. The cavity detaches at .4% of the chord length aft of the leading edge at all spanwise strips.

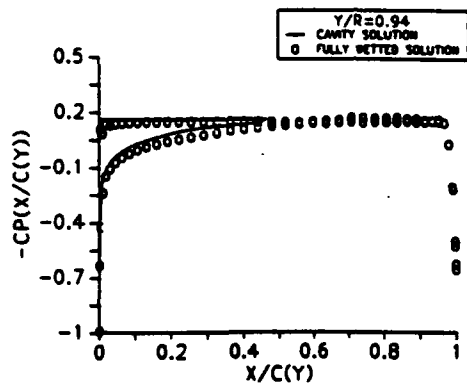
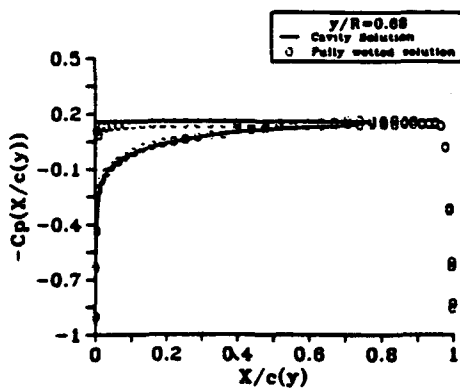
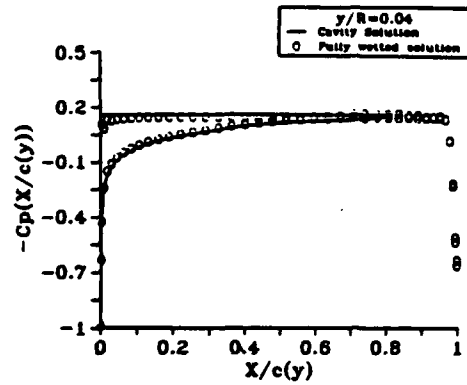
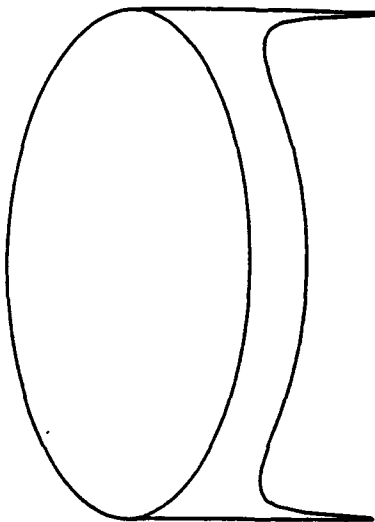


Figure 5-10: Pressure validation for a supercavitating elliptic hydrofoil at $\alpha = 3^\circ$ and $\frac{g}{\rho} = .33$.

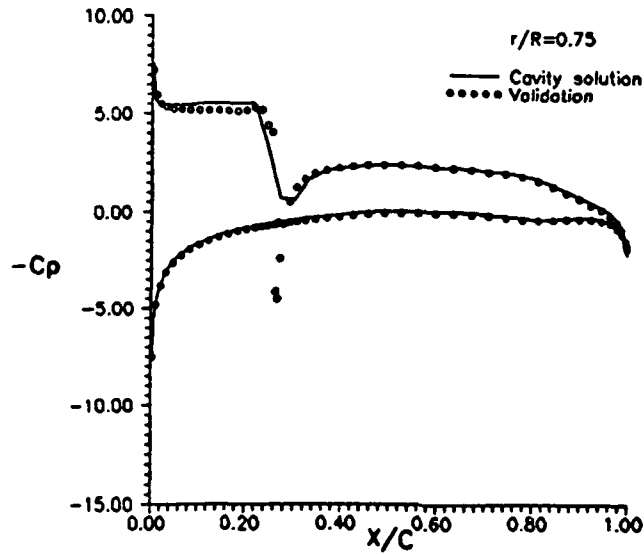


Figure 5-11: Pressure validation for the test propeller at $J_S = 0.8$ and $\sigma = 2.7$.

as it does in 2-D. We see that the cavity extent is overpredicted by linear theory in both spanwise and chordwise directions. On the other hand, the linear theory with leading edge corrections is seen to underpredict the extent, although the shape it produces is more accurate than linear theory. A comparison is then made for the same propeller in nonuniform axial wake inflow (the same inflow as shown in Figure 5-5). In this case, the hydrostatic terms are turned on ($Fr = n^2 D/g = 10.45$). The advance coefficient and the cavitation number are kept the same as in the steady flow case. The cavity volume histories predicted by the three methods are shown in Figure 5-13.

5.2.4 Effect of the Hub

The hub may be included in the solution. Quadrilateral panels are placed on the surface of the hub and Green's formula is satisfied, subject to the kinematic boundary condition. The modelling of the hub has been described by J.T. Lee [49].

The effect of the hub on the cavity solution is shown in Figure 5-14 for the test propeller at $J_S = 0.8$ and $\sigma_n = 2.7$ in steady flow. Note that the presence of the hub makes the cavity larger at the inner radii because the local increase in circulation. This effect is not captured in the linear solution (PUF-3A), because the hub is not

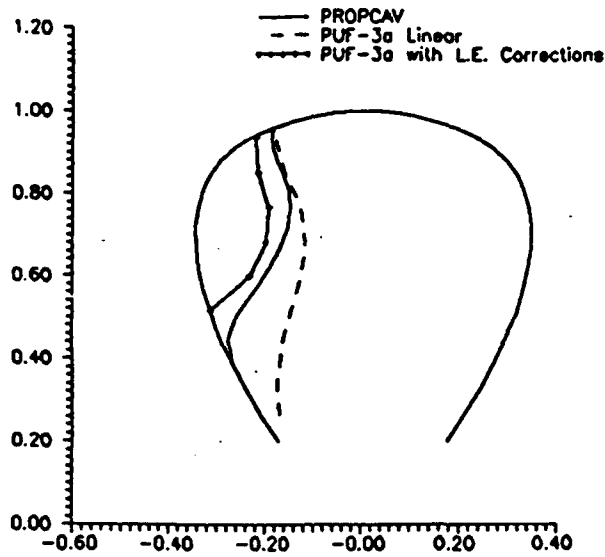


Figure 5-12: Cavity planforms predicted by PUF-3A (with and without the leading edge correction) and the present method (implemented in the code PROPCAV) on the modified N4381 test propeller at $J_S = 0.8$ and $\sigma = 2.7$ in uniform flow.

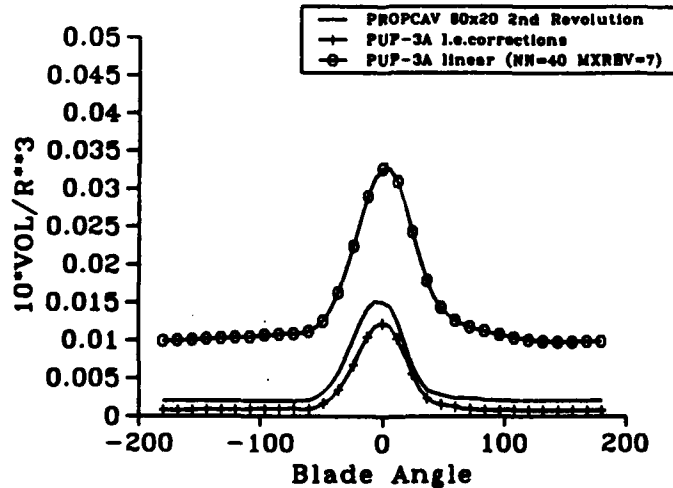


Figure 5-13: Cavity volume histories predicted by PUF-3A (with and without the leading edge correction) and the present method on the test propeller at $J_S = 0.8$ and $\sigma = 2.7$ in nonuniform flow.

included in that model.

5.2.5 Comparison to Experimental Results

No systematic comparisons of numerical results to experimental results have been done for this thesis. However, several qualitative comparisons can be made to published observations. Since one of the main accomplishments of the present work has been the prediction of cavity planforms, it would be useful to compare predicted planforms to observed planforms. In a paper by Kato, et al [26], experimental results are presented for an elliptic hydrofoil. A reproduction of one of their observed planforms is shown in Figure 5-15. Although there are some ambiguities about the geometry and operating conditions, I have computed a planform using the present method for conditions which I believe are close (if not identical) to the experimental conditions. The computed results are also shown in Figure 5-15. This comparison shows at least qualitative agreement. For example, the behavior of the cavity near the tip (for $r/R > .8$, say) seems to agree qualitatively.

Van Houten studied a 3-D pitching rectangular foil under cavitating and noncavitating conditions [72]. The unsteady nature of his experiment makes it impossible to compare his observations to the present computations. However, the rapid decrease of the cavity extent near the tip, which may be expected to occur also in steady flow, appear in the present computations (see, for example, Figure 5-2). An example of Van Houten's experimental observations is shown in Figure 5-16, where this sharp drop-off of cavity length near the tip is visible.

Cumberbatch studied tip effects on a cavitating rectangular wedge at an angle of attack. In his study, he observed supercavity patterns which tended to disappear near the tip, in qualitative agreement with the present results (as shown in Figure 5-2). According to Cumberbatch's observations, the tip vortex and the sheet cavity were separated by a wetted region.

A supercavitating 2-D hydrofoil experiment was carried out at MIT's Marine Hydrodynamics Laboratory in the Variable Pressure Water Tunnel by Kinnas and Mazel [40]. In that work, the authors compared measured velocities to those computed

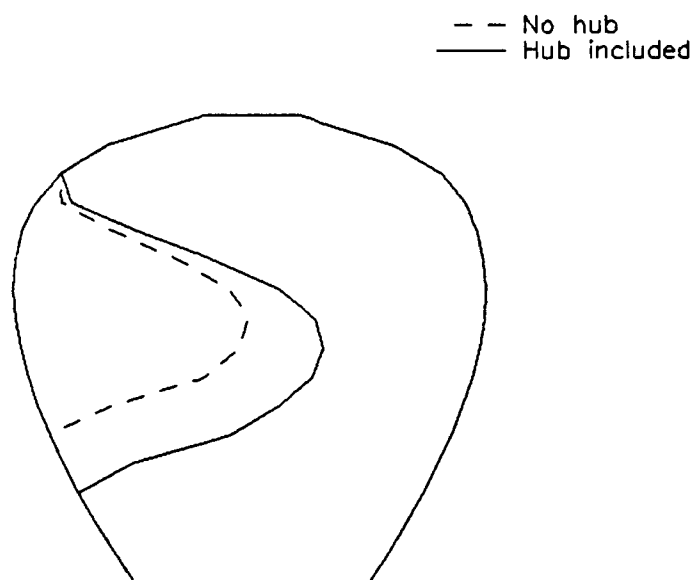


Figure 5-14: Cavity planform with and without inclusion of the hub for the test propeller at $J_S = 0.8$ and $\sigma = 2.7$ in steady flow.

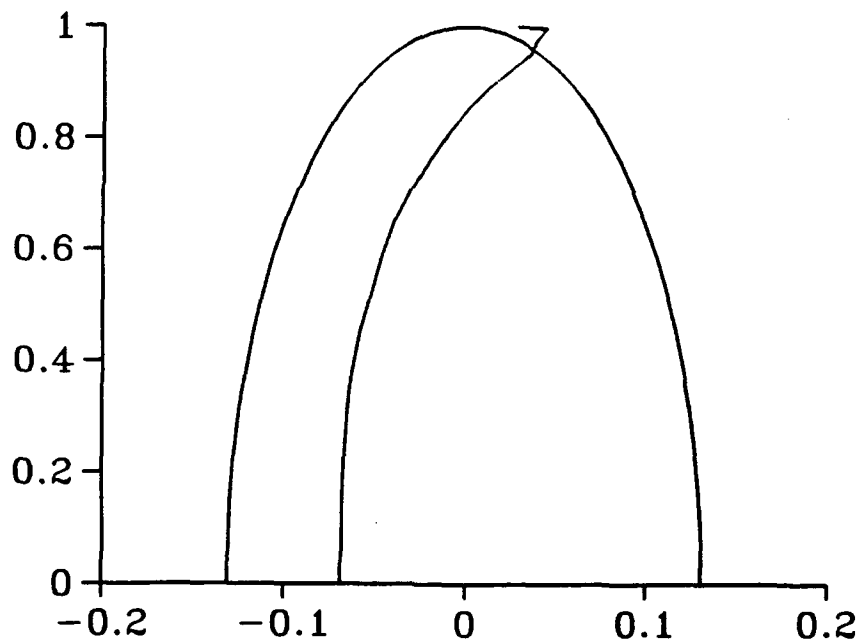
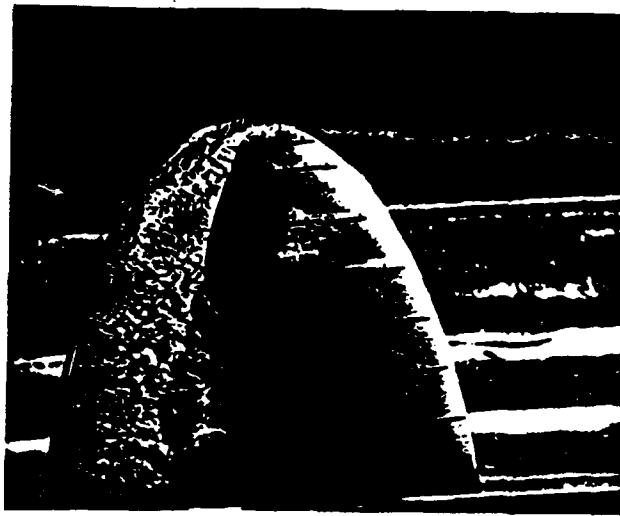


Figure 5-15: Qualitative comparison between numerical results and experimental observation for an elliptic hydrofoil which is 12% thick with aspect ratio $AR = 3$ at $\alpha = 10^\circ$ and $\sigma = 0.6$. Photograph taken from Kato, et al (1992).



Figure 5-16: A reproduction of a photograph of a partially cavitating 3-D pitching hydrofoil. The cavitation number was $\sigma = .97$ and the reduced frequency of the pitching motion was $k = 1.0$. The picture was taken by Van Houten and found in MIT Marine Hydrodynamics Lab archives.

by the fully nonlinear boundary element method developed in this thesis. In order to make the comparison, the method of images was used to account for the presence of the walls. An example of the resulting comparison is shown in Figure 5-17. Shown are several numerical and experimental horizontal velocity profiles computed and measured near the surface of the cavity. The comparison is very good away from the cavity surface, deteriorating as the measurement point approaches the mean cavity surface. One explanation for the poor comparison near the cavity surface may be the transient nature of the flow there due to unsteady motions of the cavity [40]. Nevertheless, the authors concluded that the overall agreement between theory and experiment was very good, with the analysis predicting the flow away from the cavity quite accurately.

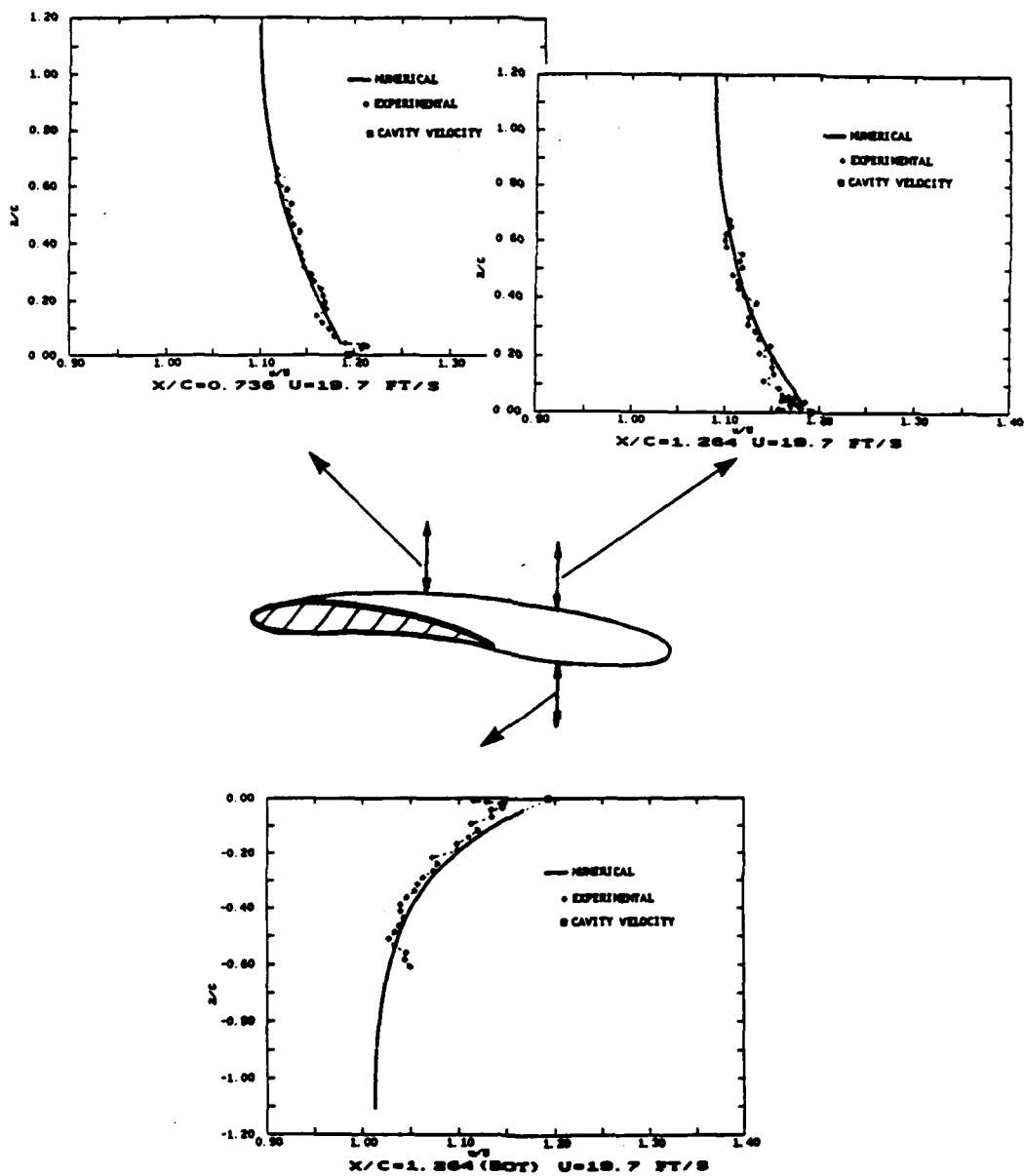


Figure 5-18: A comparison of experimental (measurements by Kinnas and Mazel) and numerical (computations by Fine) velocity profiles on a supercavitating 2-D hydrofoil in a water tunnel. Taken from Kinnas and Mazel (1992).

Chapter 6

Conclusions and Recommendations

6.1 Conclusions

In this thesis, an efficient and robust numerical method has been developed for accurately predicting the extent and shape of sheet cavities on propellers in unsteady flow. Along the way, the method was extensively validated by numerical convergence and consistency tests for 2-D and 3-D hydrofoils in steady flow, for propellers in steady flow, and for propellers in unsteady flow. The applied boundary conditions include all nonlinear and crossflow terms. However, for three dimensional flows, the conditions are satisfied on the solid body surface (either the hydrofoil or propeller blade surface) and the portion of the wake surface overlapped by the cavity, rather than on the exact cavity surface. This solution represents the first iteration towards the fully nonlinear solution. The first iteration solution has been shown (here and in the cited references), for two-dimensional flows, to be very close to the converged nonlinear solution for a reasonable range of angles of attack. This result has been used to argue that the first iteration is sufficient to obtain a nonlinear solution for 3-D flows, which is expected to differ only slightly from the fully nonlinear solution.

One virtue of using only the first iteration solution is the significant computational savings it represents. Both the fully wetted and the cavity solutions are found for a fixed discretization, so that the influence coefficients need only be computed once. The resulting 3-D solution has been shown to capture the nonlinear thickness effect. The dynamic boundary condition has been verified by the pressure validation test.

An additional time-saving innovation, which also solved the problem of poor planform convergence, was the split-panel method. This allowed cavity planforms to be continuous and general without adding the expense of computing additional influence coefficients.

The method developed in this thesis for treating *general* cavity planforms may be described as a *uniform formulation*, meaning that partial and supercavity planforms are both treated within the same mathematical framework using the same discretization. This makes the treatment of mixed cavity planforms, which are prevalent on cavitating propellers, simple and natural.

The method revealed the existence of multiple solutions for high aspect-ratio rectangular hydrofoils. This multiplicity is reminiscent of the analogous 2-D case, where the flat plate solution shows that there are three cavity lengths for each cavitation number for $\frac{a}{c} \leq 0.1$. For this case, experiments have shown that 2-D cavities longer than $\frac{l}{c} \approx 0.75$ are violently unstable, which effectively eliminates the occurrence two of the three predicted cavity lengths. No such observations have been reported for 3-D hydrofoils. Even though it has generally been believed that the 2-D instability (and corresponding multiplicity) disappear due to "three dimensional effects", it is highly plausible that, for high aspect ratio 3-D foils, neither the instability *nor* the multiplicity of solutions are mitigated by three-dimensionality. The multiplicity has been shown to disappear as the aspect ratio is lowered. No multiplicity has been found for the propeller solution, although a systematic investigation has yet to be tried.

In comparing the present method to the results of linear theory and linear theory with leading edge corrections for two dimensional flows, I found that linear theory substantially overpredicted the cavity length and volume (this was not a new result). The linear theory with leading edge corrections was much closer, but at high angles of attack the computed cavity volume differed substantially from the exact volume. Meanwhile, even for high angles of attack the first iteration of the nonlinear solution compares very well to the exact solution. As a result, the first iteration of the nonlinear solution was adopted in the present method.

In making a similar comparison for the propeller solution, I found that cavity planforms predicted by linear theory and linear theory with leading edge corrections each differed from the nonlinear result. The linear theory with leading edge corrections, while underpredicting the cavity extent, seemed to capture the correct character of the solution. Meanwhile, the conventional linear theory overpredicted the cavity planform in both spanwise and chordwise directions.

The pressure validation test was used as means of validating the results of the present method with respect to the fully nonlinear results. The pressure validation test showed that the first iteration cavity shapes satisfy the dynamic boundary condition within acceptable accuracy, from which it is concluded that the shapes are close to the exact nonlinear shapes. The present method is able to predict cavity shapes and pressure distributions near the leading edge and the tip with greater accuracy than linear theory, especially for propellers with extreme geometry. We conclude that the method developed in this thesis is preferable to that of PUF-3A. However, the present method labors under extensive CPU times compared to PUF-3A. For example, a fully unsteady solution (through 120 time steps, or two revolutions) of a one-bladed propeller with $(N,M)=(80,16)$ took 8 hours on a DEC 9000. PUF-3A, which uses a discretization of 40 chordwise and 9 spanwise discrete vortex/source lines, took 2.5 hours for the same geometry. For the near future, the present method is more likely to be used as a validation tool for PUF-3A. However, with ever-improving computer hardware and increasing computer speeds, it may not be long before the use of the method as a design tool is feasible. One need only look at the CPU-time history of PUF-3A as a recent example of a prohibitively expensive tool becoming cost-efficient.

6.2 Recommendations for Future Research

The following improvements may be made to the current method.

- The method is in need of an efficient algorithm for applying the nonlinear pressure Kutta condition. It should be possible to implement a base-problem solution, such as the one developed by Kinnas and Hsin [38].

- The first dipole panel in the wake should be given a linear strength distribution in order to make the solution more nearly independent of time step size [22]. This may be readily implemented in the present code.
- The ability to predict face cavitation, where the supercavity detaches forward of the trailing edge, may be added to the model. It may also be possible to treat partial cavities which occur near the leading edge on the pressure side. However, this would be logically more difficult to implement.

Other improvements which are recommended for further research are more fundamental in nature. As mentioned in Chapter 1, the fundamental assumptions made in order to admit a potential flow solution render the model incomplete. The effects of viscosity, tip and hub vortex cavitation, bubble and cloud cavitation, and the cavity trailing edge flow are all unaccounted for in the present model. However, the present model is amenable to inclusion of many of these effects. For instance, the effects of viscosity may be included via an interactive viscous/inviscid boundary layer solution, similar to the one developed by Hufford for fully wetted flows [23]. The boundary layer solution could be used to determine the thickness of the cavity wake so that the openness of the cavity correctly correlates to the sectional drag coefficient. A model for determining the correct detachment point, by correlating the point of laminar separation or turbulent transition to the point of cavity detachment (as suggested by several previous researchers [2, 13]), may also be implemented. A model of the cavitating tip vortex may be added to improve the solution at the tip. This could be accomplished by treating the tip vortex as an inner problem, the solution of which should be matched to the outer solution from the present method. The inner problem could be treated by a boundary element method with a grid which is chosen to fit a vortex with an assumed core radius (possibly determined semi-empirically).

Before implementing any of these models, however, a systematic series of experiments should be performed to better define the physical nature of the flow. For example, detailed flow mapping should be done to determine the nature of the boundary layer in front of and behind the cavity. This should be done first for a two-dimensional

hydrofoil. It would also be useful to obtain more detailed velocity profiles above and approaching the cavity surface, especially near the cavity trailing edge. Experiments should also be used to systematically validate the computations for propeller sheet cavitation. Accurate measurements of cavity planforms should be obtained, first for a propeller in steady flow, for comparison to computed planforms. Thrust, torque, efficiency and spanwise circulation distributions may also be measured and compared to computed values. Later, a wake screen should be used to create a circumferentially nonuniform inflow to the propeller and a similar systematic comparison should be made. While the propeller is being studied, velocity measurements should be made through a tip vortex to determine its size. The effect of parameters, such as advance coefficient, cavitation number, and Reynolds number on the vortex core diameter should be investigated. The boundary layer near the tip and its relationship to the vortex core size should also be studied.

A firm foundation, in the form of an accurate inviscid solution, is required to build our more physical models. The vortex/source lattice method, as implemented in the code PUF-3A, is not a very strong foundation due to the neglect of blade thickness and the crude treatment of the propeller tip geometry. The present method, however, is an accurate inviscid solution and will serve as a good base for implementing the additional models.

Bibliography

- [1] A.J. Acosta. A note on partial cavitation of flat plate hydrofoils. Technical Report No. E-19.9, California Institute of Technology, Hydrodynamics Laboratory, October 1955.
- [2] H. Arakeri. Viscous effects on the position of cavitation separation from smooth bodies. *Journal of Fluid Mechanics*, vol 68(Ns 4):pp 779-799, 1975.
- [3] G.K. Batchelor. *An Introduction to Fluid Dynamics*. Cambridge University Press, Cambridge, 1967.
- [4] G. Birkhoff and E.H. Zarantonello. *Jets, Wakes and Cavities*. Academic Press Inc., New York, 1957.
- [5] J.P. Breslin, R.J. Van Houten, J.E. Kerwin, and C-A Johnsson. Theoretical and experimental propeller-induced hull pressures arising from intermittent blade cavitation, loading, and thickness. *Trans. SNAME*, 90, 1982.
- [6] G. Chahine, R. Duraiswami, and M. Rebut. Analytical and numerical study of large bubble/bubble and bubble/flow interactions. In *Proceedings of the Nineteenth Symposium on Naval Hydrodynamics*, Seoul, Korea, August 1992.
- [7] R.W. Clark. A new iterative matrix solution procedure for three-dimensional panel methods. In *23rd Aerospace Sciences Meeting*, Reno, Nevada, January 1985. AIAA.
- [8] L. D'Agostino and C.E. Brennen. Linearized dynamics of spherical bubble clouds. *Journal of Fluid Mechanics*, 199, 1989.

- [9] A.G. Efros. Hydrodynamic theory of two-dimensional flow with cavitation. *Dokl. Akad. Nauk. SSSR*, vol 51:pp 267-270, 1946.
- [10] A.G. Fabula. Thin-airfoil theory applied to hydrofoils with a single finite cavity and arbitrary free streamline detachment. *Journal of Fluid Mechanics*, vol 12:pp 227-240, 1962.
- [11] N.E. Fine. Computational and experimental investigations of the flow around cavitating hydrofoils. Technical Report No. 88-6, MIT, Department of Ocean Engineering, September 1988.
- [12] N.E. Fine and S.A. Kinnas. A Boundary Element Method for the Analysis of the Flow Around 3-D Cavitating Hydrofoils, March 1992. Recommended for publication in *Journal of Ship Research*.
- [13] J.P. Franc and J.M. Michel. Attached cavitation and the boundary layer: Experimental investigation and numerical treatment. *Journal of Fluid Mechanics*, vol. 154:pp 63-90, 1985.
- [14] O. Furuya. Nonlinear calculation of arbitrarily shaped supercavitating hydrofoils near a free surface. *Journal of Fluid Mechanics*, vol. 68:pp 21-40, 1975.
- [15] O. Furuya. Three-dimensional theory on supercavitating hydrofoils near a free surface. *Journal of Fluid Mechanics*, 71:pp. 339-359, 1975.
- [16] J.A. Geurst and R. Timman. Linearized theory of two-dimensional cavitation flow around a wing section. *IX International Congress of Applied Mechanics*, 1956.
- [17] D.S. Greeley. Private communication.
- [18] D.S. Greeley and J.E. Kerwin. Numerical methods for propeller design and analysis in steady flow. *Trans. SNAME*, vol 90, 1982.

- [19] L. Guerri, G. Lucca, and A. Prosperetti. A numerical method for the dynamics of non-spherical cavitation bubbles. In *Proc. Second International Colloquium on Drops and Bubbles*, Monterey, CA, November 1981.
- [20] Lemonnier H. and Rowe A. Another approach in modelling cavitating flows. *Journal of Fluid Mechanics*, vol 195, 1988.
- [21] T. Hoshino. Hydrodynamic analysis of propellers in steady flow using a surface panel method. In *Proceedings of the Spring Meeting*, number 1-6. The Society of Naval Architects of Japan, May 1989.
- [22] Ching-Yeh Hsin. *Development and Analysis of Panel Method for Propellers in Unsteady Flow*. PhD thesis, Department of Ocean Engineering, MIT, September 1990.
- [23] G. Hufford. Viscous flow around marine propellers using boundary layer strip theory. Master's thesis, Massachusetts Institute of Technology, May 1992.
- [24] B. Jacoby, P. Delpero, and S. Price. Hydrodynamic measurements around a cavitating hydrofoil, 1990. Unpublished.
- [25] C.W. Jiang and P. Leehey. A numerical method for determining forces and moments on supercavitating hydrofoils of finite span. In *Second Int'l Conf. Numer. Ship Hydrodynamics*, Berkeley, September 1977.
- [26] H. Kato, N. Takasugi, and H. Yamaguchi. Numerical analysis of a cavitating hydrofoil with finite span. In *Int. Symp. on Propulsors and Cavitation*, Hamburg, June 1992.
- [27] D. P. Keenan. *Marine Propellers in Unsteady Flow*. PhD thesis, M.I.T., Department of Ocean Engineering, May 1989.
- [28] J.E. Kerwin. A numerical method for the analysis of cavitating propellers in a nonuniform flow, MIT-PUF-3 user's manual. Technical Report 83-6, MIT, Department of Ocean Engineering, June 1983.

- [29] J.E Kerwin. Marine propellers. *Ann. Rev. Fluid Mech.*, 18:pp. 387-403, 1986.
- [30] J.E. Kerwin, S.A. Kinnas, J-T Lee, and W-Z Shih. A surface panel method for the hydrodynamic analysis of ducted propellers. *Trans. SNAME*, 95, 1987.
- [31] J.E. Kerwin, S.A. Kinnas, M.B. Wilson, and McHugh J. Experimental and analytical techniques for the study of unsteady propeller sheet cavitation. In *Proceedings of the Sixteenth Symposium on Naval Hydrodynamics*, Berkeley, California, July 1986.
- [32] J.E. Kerwin and C-S Lee. Prediction of steady and unsteady marine propeller performance by numerical lifting-surface theory. *Trans. SNAME*, vol 86, 1978.
- [33] S.A. Kinnas. Leading-edge corrections to the linear theory of partially cavitating hydrofoils. *Journal of Ship Research*, 35(1):pp. 15-27, March 1991.
- [34] S.A. Kinnas. Leading edge correction to the linear theory of cavitating hydrofoils and propellers. In *Int. Symp. on Propeller and Cavitation*, Hangzhou, China, September 1992.
- [35] S.A. Kinnas and N.E. Fine. Non-Linear Analysis of the Flow Around Partially or Super-Cavitating Hydrofoils by a Potential Based Panel Method. In *Boundary Integral Methods-Theory and Applications, Proceedings of the IABEM-90 Symposium of the International Association for Boundary Element Methods*, pages 289-300, Rome, Italy, October 1990. Springer-Verlag.
- [36] S.A. Kinnas and N.E. Fine. A Numerical Nonlinear Analysis of the Flow Around 2-D and 3-D Partially Cavitating Hydrofoils, September 1991. Submitted for Publication. Also in report form (Technical Report number 91-7, Department of Ocean Engineering, MIT, September 1991).
- [37] S.A. Kinnas and N.E. Fine. Analysis of the flow around supercavitating hydrofoils with midchord and face cavity detachment. *Journal of Ship Research*, vol 35(No. 3):198-209, September 1991.

- [38] S.A. Kinnas and C-Y. Hsin. A boundary element method for the analysis of the unsteady flow around extreme propeller geometries. *AIAA Journal*, March 1992.
- [39] S.A. Kinnas, C-Y. Hsin, and D.P. Keenan. A potential based panel method for the unsteady flow around open and ducted propellers. In *Proceedings of the Eighteenth Symposium on Naval Hydrodynamics*, pages 667-685, Ann Arbor, Michigan, August 1990.
- [40] S.A. Kinnas and C.H. Mazel. Numerical vs. experimental cavitation tunnel (a supercavitating hydrofoil experiment). In *23rd ATTC Conference*, New Orleans, LA, 1992.
- [41] R.T. Knapp, J.W. Daily, and F.G. Hammitt. *Cavitation*. McGraw-Hill, New York, 1970.
- [42] G. Kreisel. Cavitation with finite cavitation numbers. Technical Report No. R1/H/36, Admiralty Res. Lab., 1946.
- [43] A. Kubota, H. Kato, and H. Yamaguchi. A new modelling of cavitating flows: a numerical study of unsteady cavitation on a hydrofoil section. *Journal of Fluid Mechanics*, 240:pp 59-96, 1992.
- [44] Sir Horace Lamb. *Hydrodynamics*. Cambridge University Press, sixth edition, 1932.
- [45] Chung-Sup Lee. *Prediction of Steady and Unsteady Performance of Marine Propellers with or without Cavitation by Numerical Lifting Surface Theory*. PhD thesis, M.I.T., Department of Ocean Engineering, May 1979.
- [46] C.S. Lee, Y.G. Kim, and J.T. Lee. A potential-based panel method for the analysis of a 2-d super- or partially cavitating hydrofoil. *Journal of Ship Research*, 36:pp 168-181, 1992.
- [47] Jin-Tae Lee. *A Potential Based Panel Method for the Analysis of Marine Propellers in Steady Flow*. PhD thesis, MIT, Department of Ocean Engineering, 1987.

- [59] Widnall S.E. Unsteady loads on supercavitating hydrofoils. *Journal of Ship Research*, 9:pp. 107-118, 1966.
- [60] M. Shiffman. On free boundaries of an ideal fluid — i. In *Communications on Pure and Applied Mathematics*, 1948.
- [61] M. Shiffman. On free boundaries of an ideal fluid — ii. In *Communications on Pure and Applied Mathematics*, 1949.
- [62] Sir John Thornycroft and S.W. Barnaby. Torpedo boat destroyers. *Minutes of Proc. Inst. of Civil Engineers*, 122, 1895.
- [63] M.P. Tulin. Steady two-dimensional cavity flows about slender bodies. Technical Report 834, DTMB, May 1953.
- [64] M.P. Tulin. Supercavitating flow past foils and struts. In *Symposium on Cavitation in Hydrodynamics*, NPL, Teddington, England, September 1955.
- [65] M.P. Tulin. Supercavitating flows - small perturbation theory. *Journal of Ship Research*, vol 7(No. 3):pp. 16-37, 1964.
- [66] M.P. Tulin. An analysis of unsteady sheet cavitation. In *Proceedings of the 19th ATTC Conference*, pages 1049-1079, 1980.
- [67] M.P. Tulin and C.C. Hsu. New applications of cavity flow theory. In *13th Symposium on Naval Hydrodynamics*, Tokyo, Japan, 1980.
- [68] J.S. Uhlman. A partially cavitated hydrofoil of finite span. *Journal of Fluids Engineering*, 100(3):pp. 353-354, September 1978.
- [69] J.S. Uhlman. *A Surface Singularity Method for Cavitating Hydrofoils*. PhD thesis, Department of Ocean Engineering, M.I.T., October 1983.
- [70] J.S. Uhlman. The surface singularity method applied to partially cavitating hydrofoils. *Journal of Ship Research*, vol 31(No. 2):pp. 107-124, June 1987.

- [48] P. Leehey. Supercavitating hydrofoil of finite span. In *IUTAM Symposium on Non-Steady Flow of Water at High Speeds*, pages 277-298, Leningrad, June 1971.
- [49] B. Maskew. Prediction of subsonic aerodynamic characteristics: A case for low-order panel methods. *Journal of Aircraft*, vol 19(no 2):pp 157-163, February 1982.
- [50] Jack Moran. *An Introduction to Theoretical and Computational Aerodynamics*. John Wiley and Sons, 1984.
- [51] L. Morino and B.K. Bharadvaj. A unified approach for potential and viscous free-wake analysis of helicopter rotors. *Vertica*, vol 12(no 1/2), 1988.
- [52] L. Morino, Jr. Kaprielian, Z., and S.R. Sipcic. Free wake aerodynamic analysis of helicopter rotors. Technical Report CCAD-TR-83-01, Boston University, MAY 1983.
- [53] Luigi Morino and Ching-Chiang Kuo. Subsonic potential aerodynamic for complex configurations : A general theory. *AIAA Journal*, vol 12(no 2):pp 191-197, February 1974.
- [54] J.N. Newman. *Marine Hydrodynamics*. The MIT Press, Cambridge, Massachusetts, 1977.
- [55] J.N. Newman. Distributions of sources and normal dipoles over a quadrilateral panel. *Journal of Engineering Mathematics*, vol 20:pp 113-126, 1986.
- [56] T. Nishiyama. Lifting line theory of supercavitating hydrofoil of finite span. *ZAMM*, 50:645-653, 1970.
- [57] C. Pellone and A. Rowe. Supercavitating hydrofoils in non-linear theory. In *Third International Conference on Numerical Ship Hydrodynamics*, Paris, France, June 1981. Basin d'essais des Carènes.
- [58] D. Riabouchinsky. On steady fluid motions with free surfaces. *Proceedings of London Math. Soc.*, Vol. 19:pp 206-215, 1921.

Appendix A

Green's Formula on the Wake Surface

The goal of this Appendix is to prove that equation (2.9) of Chapter 2 is correct. This equation is a modified version of Green's formula, when the control point lies on the upper half of the wake surface (see section 2.2). The canonical problem of a fully wetted hydrofoil with a wake will be considered (see Figure A-1). The wake will be a surface of discontinuity in ϕ only, since the treatment of the source discontinuity in the cavity flow problem is relatively straightforward.

Consider a hydrofoil subject to an incoming free stream U_{in} , as shown in Figure A-1. If there exists a velocity potential ϕ which is harmonic everywhere in the flow field, then it is a classic result that ϕ must satisfy Green's 3rd identity, which can be written in the following form

$$I = \int_{S_B} \left[\phi_q \frac{\partial G(p; q)}{\partial n_q} - G(p; q) \frac{\partial \phi_q}{\partial n_q} \right] dS + \int_{S_w} (\phi_q^+ - \phi_q^-) \frac{\partial G(p; q)}{\partial n_q} dS \quad (A.1)$$

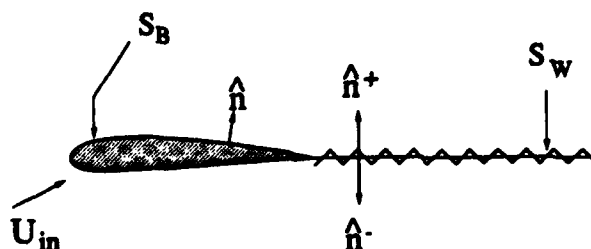


Figure A-1: Hydrofoil and wake, showing the branch cut on the wake surface.

- [71] J.S. Uhlman. The surface singularity or boundary integral method applied to supercavitating hydrofoils. *Journal of Ship Research*, vol 33(No. 1):pp. 16-20, March 1989.
- [72] R.J. Van Houten. The transient cavitation of a two dimensional hydrofoil comparison of theory and experiment, 1979. Unpublished.
- [73] R.J. Van Houten. The numerical prediction of unsteady sheet cavitation on high aspect ratio hydrofoils. In *14th Symposium on Naval Hydrodynamics*, 1982.
- [74] R.B. Wade and A.J. Acosta. Experimental observation on the flow past a plano-convex hydrofoil. *Transactions ASME, J. Basic Engineering*, 88-1, 1966.
- [75] T.Y. Wu. Cavity flows and numerical methods. In *First International Conference on Numerical Ship Hydrodynamics*, 1975.
- [76] T.Y. Wu and D.P. Wang. A wake model for free-streamline flow theory. part 2. cavity flows past obstacles of arbitrary profile. *Journal of Fluid Mechanics*, vol 18:pp 65-93, 1964.

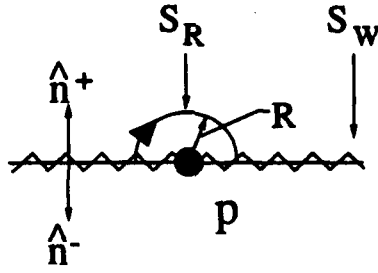


Figure A-2: A blow-up of the field point p , showing the small patch of the surface replaced by a hemisphere of radius R .

where p and q are the field point and the variable point in the integration, respectively. $G(p; q) = 1/R(p; q)$ is Green's function, where $R(p; q)$ is the distance between the points p and q . The surface S_W is the upper half of the wake, as shown in Figure A-1. The value of the integral I depends on the location of the field point:

$$I = \begin{cases} 4\pi\phi_p & \forall p \text{ outside } S_B, S_W \\ 0 & \forall p \text{ inside } S_B \\ 2\pi\phi_p & \forall p \text{ on } S_B \end{cases} \quad (\text{A.2})$$

Equation (A.1) is a Fredholm integral equation of the second kind when the field point is either in the flow field or on the hydrofoil surface. However, equation (A.2) does not define I for the case when the field point lies on a branch cut, which is the case for the cavity flow problem discussed in Chapter 2. In the following, equation (A.2) will be generalized to include the case where p lies on the upper side of a surface across which ϕ is discontinuous.

Consider Green's 3rd identity when the field point lies on the wake surface S_W . In this case, the integral over S_W must exclude the field point in order for Green's formula to hold. This is done by surrounding the field point by a hemisphere S_R of radius R which indents the surface into the external flow, as shown in Figure A-2. Green's formula now takes the form

$$\frac{1}{4\pi} \int_{S_B} \left[\phi_q \frac{\partial G(p; q)}{\partial n_q} - G(p; q) \frac{\partial \phi_q}{\partial n_q} \right] dS + \frac{1}{4\pi} \int_{S_W + S_R} (\phi_q^+ - \phi_q^-) \frac{\partial G(p; q)}{\partial n_q} dS = 0. \quad (\text{A.3})$$

or

$$\begin{aligned} & \frac{1}{4\pi} \int_{S_B} \left[\phi_q \frac{\partial G(p; q)}{\partial n_q} - G(p; q) \frac{\partial \phi_q}{\partial n_q} \right] dS + \frac{1}{4\pi} \int_{S_W} (\phi_q^+ - \phi_q^-) \frac{\partial G(p; q)}{\partial n_q} dS = \\ & - \frac{1}{4\pi} \int_{S_R} (\phi_q^+ - \phi_q^-) \frac{\partial G(p; q)}{\partial n_q} dS \end{aligned} \quad (A.4)$$

Consider the integral on the right-hand-side of equation (A.4). We first split the integral into two integrals

$$\frac{1}{4\pi} \int_{S_R} (\phi_q^+ - \phi_q^-) \frac{\partial G(p; q)}{\partial n_q} dS = \frac{1}{4\pi} \int_{S_R} \phi_q^+ \frac{\partial G(p; q)}{\partial n_q} dS - \frac{1}{4\pi} \int_{S_R} \phi_q^- \frac{\partial G(p; q)}{\partial n_q} dS. \quad (A.5)$$

In the limit as R tends to zero the two integrals on the right-hand-side of (A.5) may be evaluated under the assumption that ϕ is regular on S_R . Equation (A.5) becomes

$$\begin{aligned} & \frac{1}{4\pi} \int_{S_R} (\phi_q^+ - \phi_q^-) \frac{\partial G(p; q)}{\partial n_q} dS = \frac{1}{4\pi} \lim_{R \rightarrow 0} \left[\phi^+ \frac{\partial}{\partial r} \frac{1}{r} \right]_{r=R} \cdot 2\pi R^2 \\ & - \frac{1}{4\pi} \lim_{R \rightarrow 0} \left[-\phi^- \frac{\partial}{\partial r} \frac{1}{r} \right]_{r=R} \cdot 2\pi R^2 = -\frac{1}{2} [\phi_p^+ + \phi_p^-] \end{aligned} \quad (A.6)$$

Green's formula for the case where the field point lies on the upper wake surface may now be written:

$$2\pi(\phi_p^+ + \phi_p^-) = \int_{S_B} \left[\phi_q \frac{\partial G(p; q)}{\partial n_q} - G(p; q) \frac{\partial \phi_q}{\partial n_q} \right] dS + \int_{S_W} (\phi_q^+ - \phi_q^-) \frac{\partial G(p; q)}{\partial n_q} dS.$$

Equation (A.2) may now be generalized to

$$I = \begin{cases} 4\pi\phi_p & \forall p \text{ outside } S_B, S_W \\ 0 & \forall p \text{ inside } S_B \\ 2\pi\phi_p & \forall p \text{ on } S_B \\ 2\pi(\phi_p^+ + \phi_p^-) & \forall p \text{ on } S_W \end{cases} \quad (A.7)$$

Appendix B

Performance of the Method for 2-D Flows

The numerical method was developed first in two-dimensions before extending it to three dimensional geometries. The reasons for this chronology are twofold: first, it is useful to establish convergence and consistency of the method in 2-D, where algorithms are simple and computing times are negligible; and second, the general characteristics of a method are the same for 2-D and 3-D applications, a fact which allows the basics of a method to be established in 2-D before tackling the geometrically more complex 3-D problem. For example, one of the main characteristics of the present nonlinear method — which I will demonstrate in this Appendix — is that the first iteration solution is very close to the converged nonlinear solution for a wide range of operating conditions. This may be said to be a characteristic of the potential-based panel method, since the velocity-based panel method (whose influence functions are one degree more singular) converges very slowly with iterations [70]. Clearly, the quick convergence with iterations is a characteristic which may be expected to hold for 3-D geometries.

In addition to demonstrating the above-mentioned rapid convergence, the objective of this Appendix is to display numerical convergence and consistency of the 2-D solution. Details of the solution, which are entirely analogous to the details of the unsteady propeller solution described in the main body of this thesis, are reported in several articles which are included in the references.

N	σ	Volume/ c^3
40	0.4508	0.0036
60	0.4493	0.0034
80	0.4502	0.0033
100	0.4506	0.0033
120	0.4506	0.0033

Table B.1: Convergence with number of panels for a partially cavitating NACA16006 symmetric foil at $\alpha = 3^\circ$, $\frac{l}{c} = 0.5$ and $\frac{h_a}{c} = 0.048$. The termination model parameters are: $\frac{\lambda}{l} = 0.1$, $A = 0.3$ and $\nu = 1.0$ (for the definition of these parameters, see Appendix C).

B.1 Fixed-length Solution

The investigation of the numerical method began with the two-dimensional fixed-length problem, as reported in [35]. In what follows, I will show the results of convergence (with number of panels and with iterations) and consistency tests for partially- and super-cavitating 2-D hydrofoils with fixed-length cavities.

B.1.1 Partial Cavitation

Table B.1 shows convergence with number of panels for the first iteration solution (all panels on the foil surface) of a partially cavitating ($l = 0.4$) NACA16006 symmetric hydrofoil at $\alpha = 3^\circ$. There are two things to learn from this convergence test. The first and most important is simply that the solution does converge. The second is the number of panels required to obtain what I consider to be a converged solution (three significant figures in σ). In this case that number is near 80, which is more than that required for the fully-wetted solution (which requires roughly 60 panels for the circulation to converge to 3 significant figures [47]). One likely explanation for needing more panels for the cavity solution is the sensitivity to the leading edge flow [33, 70]. I have found that clustering panels near the leading edge (at the expense of panel density aft of the leading edge) sped the convergence of the fixed length solution slightly.

Figure B-1 shows the solution history as it proceeds from the first iteration solution

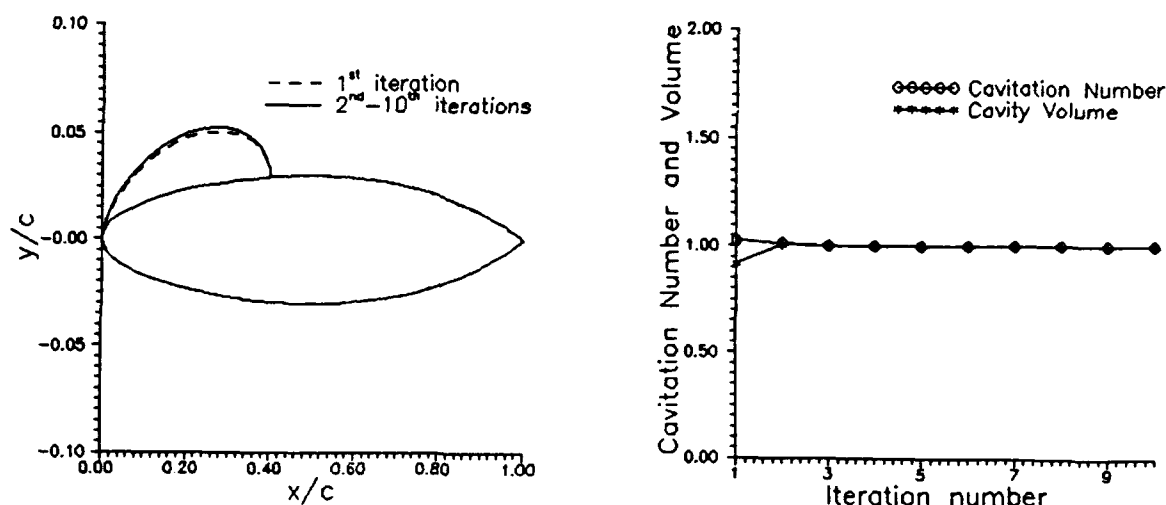


Figure B-1: Convergence history of a fully nonlinear partial cavitation fixed-length solution. NACA16006 foil at $\alpha = 3^\circ$, $\frac{l}{c} = 0.4$ and $\frac{t}{c} = 0.0$. The termination model parameters are $\lambda = 0.1$, $A = 0.5$, and $\nu = 1.0$; the number of panels is $N = 100$. The cavitation number and cavity volume shown in the plot on the right are normalized on their converged values.

to the fully nonlinear solution. The progression of cavity shapes is shown on the left of the figure and the cavitation numbers and the cavity volumes (normalized on the converged values) are shown on the right. The exceptionally quick convergence which is depicted in this figure is characteristic of the solution at a wide range of angles of attack and foil thicknesses. This will be shown for the solution of the fixed- σ problem, which is described in the next section.

Figure B-2 shows pressure validation of the first and last iterations in the nonlinear solution for a NACA16006 foil at $\alpha = 3^\circ$ and $\frac{l}{c} = 0.4$. The pressure validation, which is also described in section 5.2.2, consists of computing the fully wetted flow about a modified foil made up of the original foil and the computed cavity. The resulting pressure distribution should be constant and equal to $-\sigma$ on the cavity. The deviation from this is a measure of the error introduced by iterating only once. Notice that the pressures match exactly for the fully nonlinear solution and that, even for the first iteration solution, the pressures are very close.

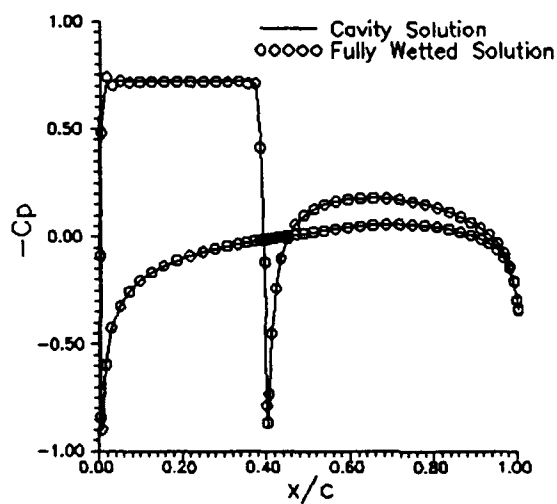
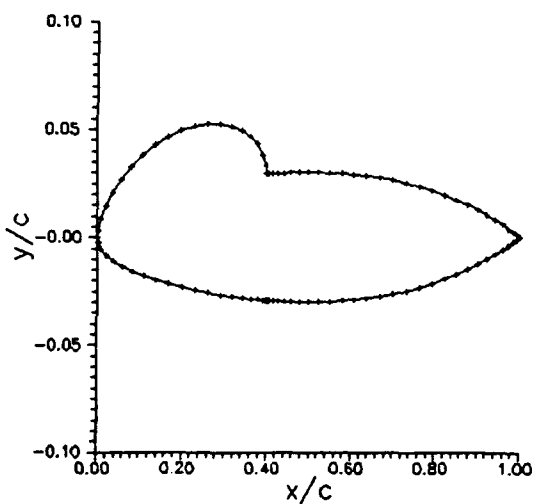
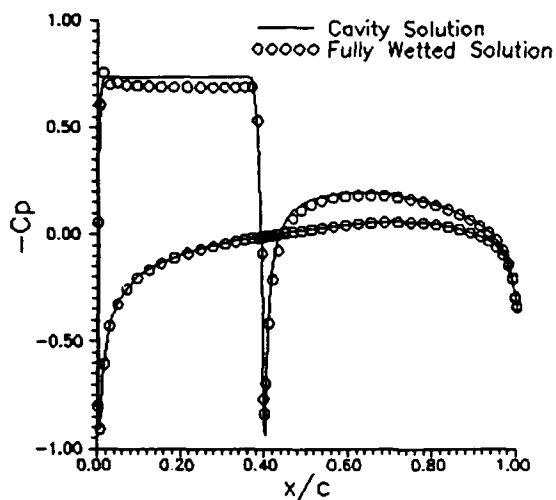
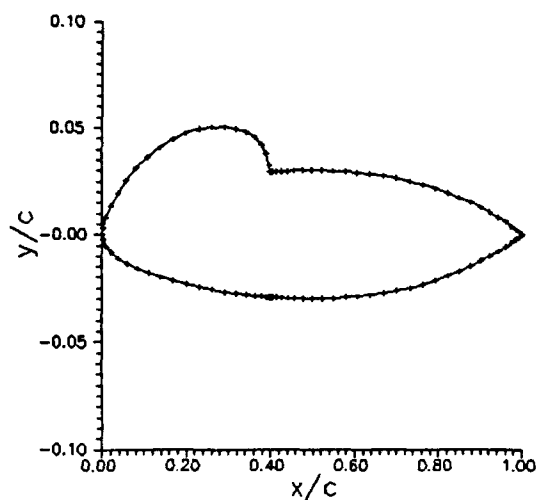


Figure B-2: Pressure validation test for the first (top) and last (bottom) iterations of the nonlinear solution presented in the previous figure. Shown to the left of each pressure distribution is the corresponding panel arrangement for the fully wetted solution.

N	σ	Volume/ c^2
80	0.130	0.190
120	0.124	0.183
160	0.122	0.180
200	0.123	0.181
240	0.123	0.181

Table B.2: Convergence with number of panels of the fixed-length solution for a supercavitating NACA16004 symmetric foil at $\alpha = 5^\circ$, $\frac{l}{c} = 2.0$ and $\frac{h_a}{c} = 0.024$. The termination model parameters are: $\frac{\lambda}{\gamma} = 0.07$, $\frac{\lambda}{\gamma} = 0.07$ (for the definition of these parameters, see Appendix C). The number of panels is $N = 100$.

B.1.2 Supercavitation

The nonlinear fixed-length solution for supercavitating hydrofoils is found by using the cavity shape predicted by linear theory as the initial guess. This is a much better initial guess than the one used for the partial cavitation fixed- l solution, since linear theory is known to be more accurate for long cavities than for short. Note that now the phrase "first iteration" means that the panels are arranged on the surface determined from linear theory (so the linear theory is the zeroth iteration). Even though there is no reasonable 3-D extension to an algorithm which uses linear theory as an initial guess, it is nonetheless useful to investigate the character of this solution. For example, the fixed-length solution will be used to investigate termination models in Appendix C. Meanwhile, since the code is available, it does not hurt to verify that the solution is convergent and consistent.

Table B.2 shows convergence with equivalent number of panels. N is the number of panels distributed around the entire foil/cavity surface, where the cavity surface is the one predicted by linear theory. The cavity length is $\frac{l}{c} = 2.0$, so the equivalent number of panels is twice that in Table B.1.

Figure B-3 shows convergence with iterations of the cavity shape, cavitation number and cavity volume for a supercavitating NACA16006 foil at $\alpha = 3^\circ$, $\frac{l}{c} = 1.5$ and $\frac{h_a}{c} = 0.05$. In this plot, the cavity shapes are shown from linear theory, the nonlinear 1st iteration, and the converged nonlinear solution. The shapes from all

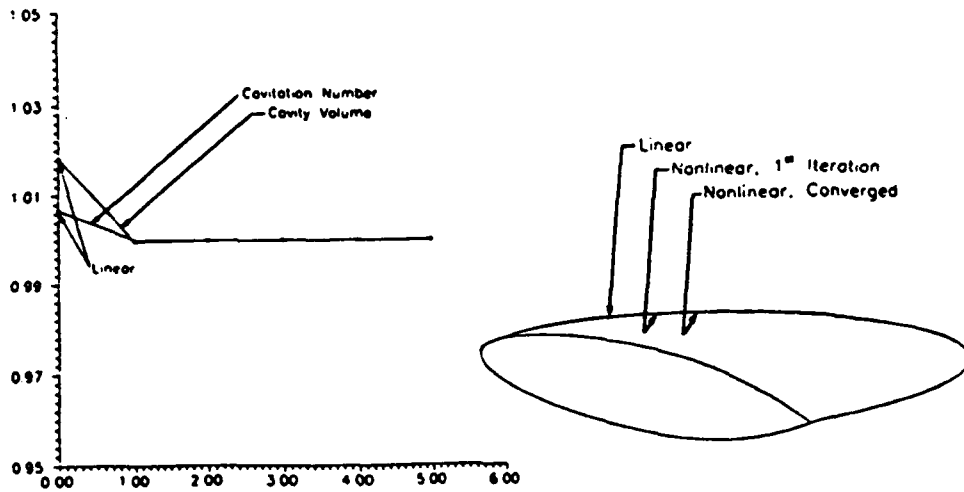


Figure B-3: Convergence of cavity shapes, cavitation number, and cavity volume with number of iterations for a supercavitating NACA16006 foil at $\alpha = 3^\circ$, $\frac{l}{c} = 1.5$, $\frac{l_a}{c} = 0.05$, $\frac{\lambda_a}{\gamma} = 0.05$, $\frac{\lambda_l}{\gamma} = 0.05$. The number of panels is $N = 100$.

three solutions are nearly indistinguishable. Figure B-4 shows pressure validation for the foil and conditions shown in Figure B-3. Here, only the first iteration pressure validation is shown, since the other solutions are nearly identical. Note that the pressure distribution reveals pressures on the lower surface which are *lower* than the cavity pressure. This means that part of the lower surface near the foil trailing edge should be cavitating and underscores the need to include so-called “face cavitation” in the model. This was done using linear theory by Kinnas and Fine [38] (where the suction-side cavity detachment point was found from the Villat-Brillouin condition), and should be added to the present method. Figure B-5 shows convergence with iterations for the same foil and conditions as in Figure B-3, except that in this case, the cavity detaches at the leading edge ($\frac{l_a}{c} = 0.0$). Note that the three solutions are now different and the linear theory no longer comes close to predicting the correct cavity shape. This may be due to the fact that the exact cavity surface intersects the foil near the leading edge, as shown in Figure B-5.

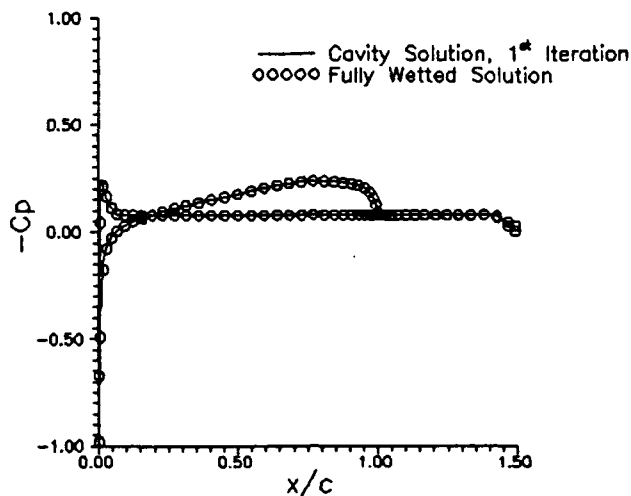


Figure B-4: Pressure validation of a supercavitating NACA16006 foil. Same foil and conditions as in Figure B-3.

B.2 Fixed- σ Solution

In practical problems, including the problem of predicting unsteady propeller sheet cavitation, the cavitation number is known and the cavity length is to be determined. In light of the ultimate goals of the research, it was clearly beneficial to solve this so-called “direct problem” in two dimensions before attempting it in three. The details of the algorithm for the first iteration solution have been described in the main body of this thesis and in [37] and [13]. The details of the fully nonlinear solution will be given in section B.2.3. In this section, I will show results of convergence and consistency tests for the 2-D fixed- σ solutions.

B.2.1 Partial Cavitation

In all of the convergence and consistency tests shown in this section, the solution is found for constant panelling (using the split panel method). Table B.3 shows convergence of cavity length and volume with number of panels (first iteration solution only) for a NACA16006 symmetric foil at $\alpha = 3^\circ$. There are two reasons why the fixed- σ solution does not converge uniformly with number of panels: first, there is a small amount of error due to the split panel method, and that error does not vanish

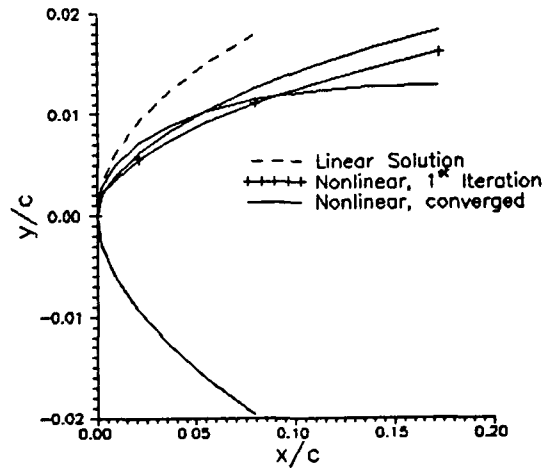
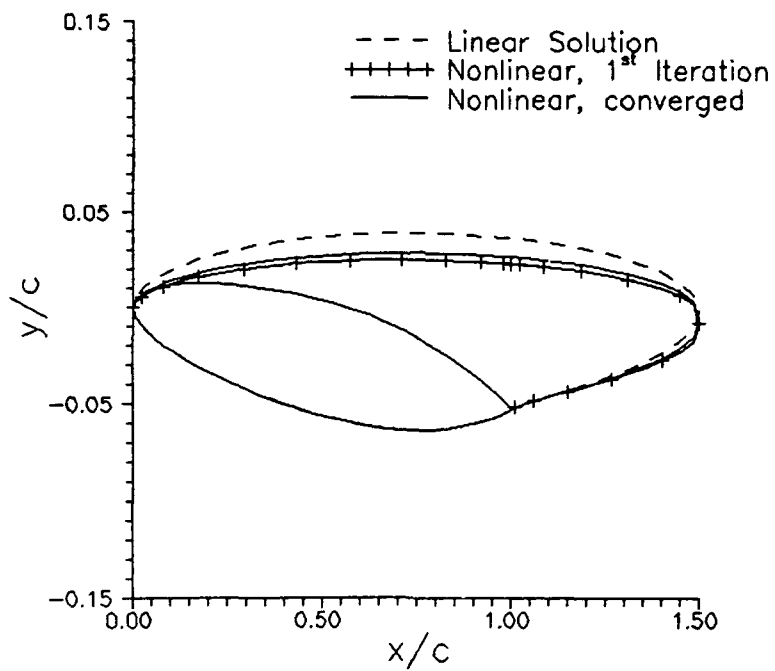


Figure B-5: Convergence of cavity shapes with number of iterations for the same foil and conditions as the previous figure, except that $\frac{h}{c} = 0.0$. In the blow up of the leading edge, it is clear that the nonlinear solutions cut the foil, while the linear solution does not.

N	$\frac{l}{c}$	Volume/ c^2	δ_{final}
60	0.3852	0.00366	4.0×10^{-5}
80	0.3944	0.00403	7.9×10^{-5}
100	0.3915	0.00392	8.3×10^{-5}
120	0.4004	0.00409	5.8×10^{-5}
140	0.3954	0.00400	-1.9×10^{-5}

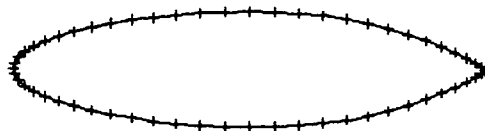


Table B.3: Convergence with number of panels of the partial cavitation fixed- σ solution for a NACA16006 symmetric foil at $\alpha = 4^\circ$, $\sigma = 0.7$ and $\frac{l}{c} = 0.024$. The termination model parameters are: $\frac{\lambda}{\Gamma} = 0.1$, $A = 0.3$, and $\nu = 1.0$. The panels are arranged with cosine spacing, as shown above for $N=60$.

locally with increased number of panels. Thus a (very) slightly different problem is being solved every time, making the convergence appear slow or nonuniform. Second, the solution is found to within a tolerance on δ , and the final tolerance may vary from one solution to the next. Invariably, the coarser the grid, the larger the tolerance must be in order to arrive at a solution. Despite these handicaps, Table B.3 shows that the method gives the same cavity length and volume ($\pm 2.5\%$) for all N greater than or equal to 80. The error caused by the split panel method has been discussed in section 4.1.1.

Another important test for the fixed- σ solution is to vary the initial guess and check that the final cavity lengths are close to one another. This test is a gauge of the error introduced by split panel method. Table B.4 shows such a test for the same foil tested in Table B.3. Shown also is the correct cavity length (which is independent of initial guess), found by treating the split panel as two panels.

Figure B-6 shows the first and last iterations in convergence to the fully nonlinear solution (see section B.2.3 for details). Also shown is the corresponding pressure validation from each solution. This figure shows that the first iteration cavity solution is very close to the converged nonlinear result.

Figure B-7 shows a comparison between the results of linear theory, linear theory with leading edge corrections, the present method (first iteration) and the fully nonlinear solution. Shown are cavity shapes from each solution, superimposed on one-another. The linear theory is seen to overpredict the cavity extent and volume

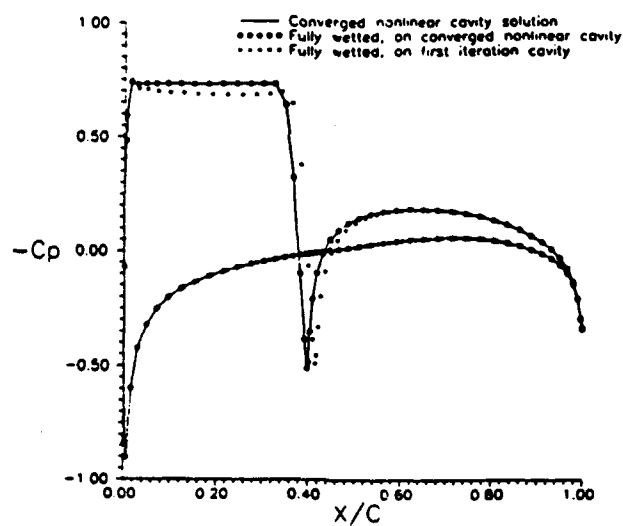
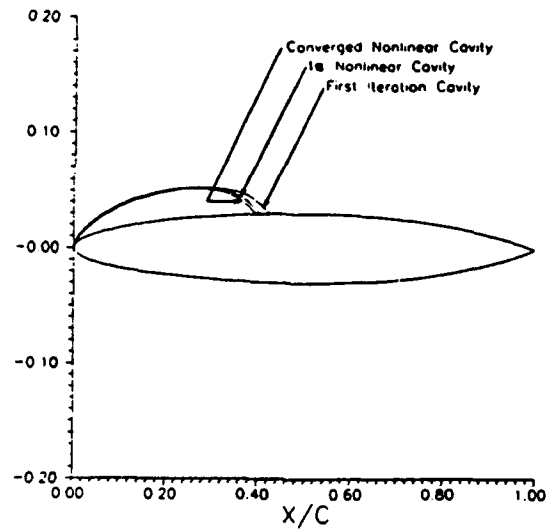


Figure B-6: Partially cavitating NACA16006 foil at $\alpha = 3^\circ$, $\lambda = 0.1$, $\nu = 1.0$, $A = 0.5$, $\sigma = .731$. The top plot shows the first and last iterations in the nonlinear fixed- σ solution. The last iteration corresponds to a σ -tolerance of 1%. Also shown is the converged nonlinear fixed- l solution. The bottom plot shows pressure validation for the first iteration and the fully nonlinear solutions.

$\frac{l}{c}_{initial}$	$\frac{l}{c}_{final}$	δ_{final}
0.1	0.3943	9.1×10^{-5}
0.2	0.3944	7.9×10^{-5}
0.3	0.3944	7.9×10^{-5}
0.4	0.3944	7.9×10^{-5}
0.5	0.3964	-9.9×10^{-5}
0.6	0.3959	-5.5×10^{-5}
0.7	0.3959	-5.5×10^{-5}
0.8	0.3963	-8.3×10^{-5}
0.9	0.3965	-1.0×10^{-4}
correct	0.3951	1.1×10^{-6}

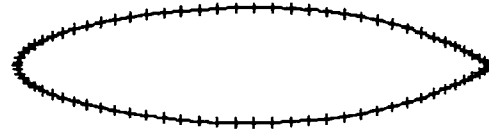


Table B.4: Varying the initial guess for the same foil and conditions as in the Table A.3. The number of panels is $N=80$, and the panel arrangement is shown above.

for each operating condition. The linear theory with leading edge corrections predicts the cavity extent well, but overpredicts the volume for high angles of attack and small thicknesses. On the other hand, the first iteration nonlinear shapes are very close to the converged nonlinear shapes for each angle of attack and each foil thickness.

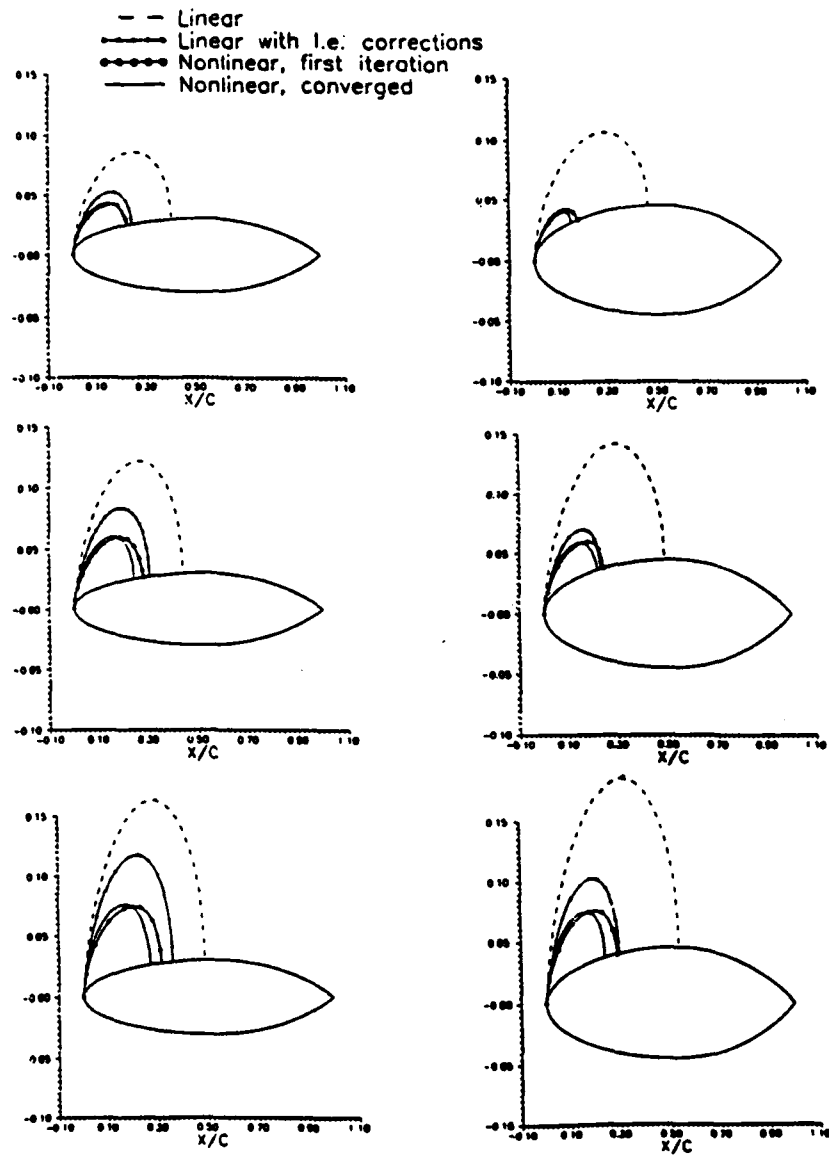


Figure B-7: Comparison of cavity shapes predicted from different methods for a NACA16 foil at $\alpha = 4^\circ$ (top), 6° (middle), and 8° (bottom), and $\frac{t}{c} = .06$ (left) and $.09$ (right). The ratio $\frac{a}{c}$ is kept fixed at $.055$. The cavity detaches at the leading edge in all cases.

B.2.2 Supercavitation

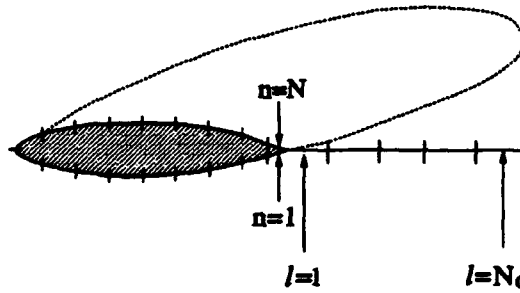
The fixed- σ supercavitating hydrofoil problem has been solved only for the first iteration, where Green's formula is satisfied on the foil surface and on the portion of the wake which is overlapped by the supercavity. Finding the fully nonlinear solution in this case was deemed unnecessary because nothing would be learned about the method that could not be inferred from the partial cavitation fixed- σ or the supercavitating fixed-length solutions.

Table B.5 displays convergence with number of panels for a supercavitating symmetric NACA16006 foil at $\alpha = 6^\circ$. There are N panels distributed in the usual cosine-spacing on the foil and N_C constant-spaced panels in the wake. The wake is re-panelled after each guess of the cavity planform, so that the cavity always ends at a panel boundary (*e.g.*, there is no split panel).

Figure B-8 shows a comparison of cavity solutions from linear theory, the present method first iteration and the present method converged nonlinear. Here the converged nonlinear shape is found from the fixed-length solution, and the other solutions are found for the σ which resulted from the fixed- l nonlinear solution. Cavity shapes are shown for a NACA16006 foil at $\alpha = 4^\circ, 6^\circ$, and 8° .

B.2.3 Partial Cavitation Fully Nonlinear Solution

It is not immediately clear how to proceed from the first iteration cavity length to a converged nonlinear cavity length for the fixed- σ solution. If we "build on" the first iteration cavity by moving the panels which represent the cavity from the foil surface to the newly computed cavity surface and apply Green's formula there for the given cavitation number, then the result will be a cavity which does not close. In fact, since we know from experience with the fixed-length solution that the nonlinear σ is always *less than* the first iteration σ , we can predict that the first iteration cavity is too long. Therefore, building on the first iteration cavity usually results in a cavity for which $\delta < 0$. By trimming off the end of the cavity which lies inside the foil, the cavity length may be shortened and another iteration may be built on the resulting



N	N_C	$\frac{l}{c}$	Volume/ c^2	δ_{final}
60	10	1.6348	0.1401	4.3×10^{-5}
60	20	1.6285	0.1408	3.8×10^{-5}
60	40	1.6262	0.1391	3.3×10^{-5}
80	10	1.6410	0.1415	4.6×10^{-5}
80	20	1.6320	0.1408	3.5×10^{-5}
80	40	1.6320	0.1404	3.5×10^{-5}
100	10	1.6415	0.1415	4.7×10^{-5}
100	20	1.6348	0.1407	3.8×10^{-5}
100	40	1.6323	0.1403	3.4×10^{-5}
120	10	1.6410	0.1412	4.7×10^{-5}
120	20	1.6343	0.1404	3.8×10^{-5}
120	40	1.6317	0.1401	3.5×10^{-5}
120	60	1.6310	0.1400	3.4×10^{-5}

Table B.5: Convergence with number of panels for a NACA16006 symmetric foil at $\alpha = 6^\circ$, $\sigma = 0.2$ and $\frac{l_h}{c} = 0.0$.

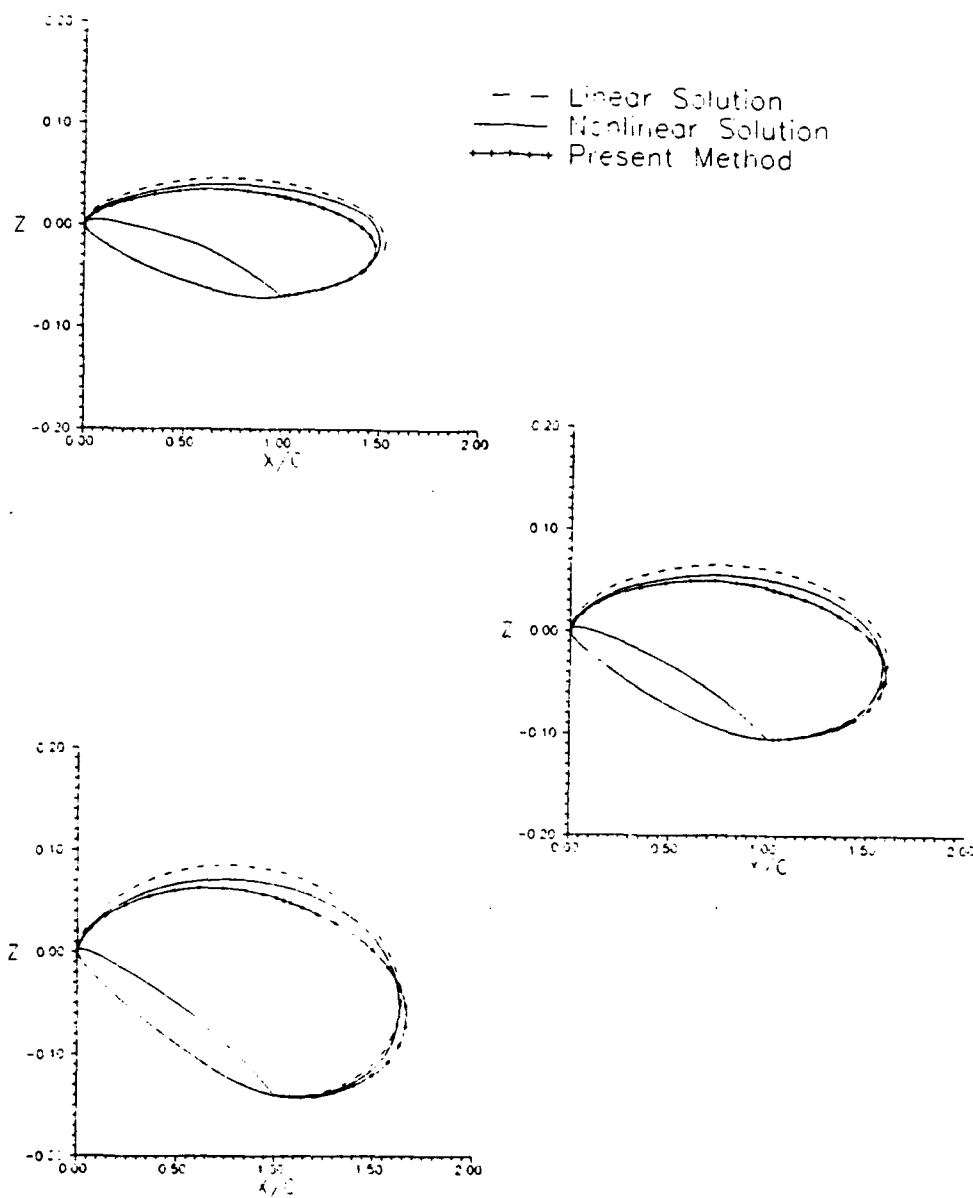


Figure B-8: Comparison of supercavity shapes predicted from linear theory, the present method, and nonlinear theory for a NACA16004 foil at $\alpha = 4^\circ$ (top), $\alpha = 6^\circ$ (middle), and $\alpha = 8^\circ$ (bottom). The ratio $\frac{a}{c}$ is kept fixed at 0.440. In each case, the cavity detaches at the leading edge.

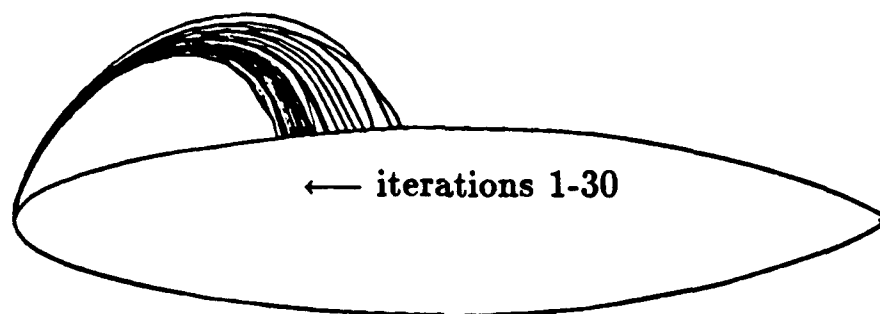


Figure B-9: An example of the original method for finding the nonlinear fixed- σ solution. The convergence is seen here to be very slow.

cavity shape. Repeating this procedure will eventually lead to the nonlinear cavity shape. Unfortunately, I found that the convergence of this scheme was very slow, as is evident in Figure B-9.

An accelerated scheme has been developed which takes advantage of the fact that the difference between the cavitation numbers from the first and the converged iterations with fixed cavity length, $\frac{l}{c}$, behaves smoothly with $\frac{l}{c}$. With σ being the given cavitation number, the proposed algorithm is as follows:

1. Solve the cavity problem (first iteration) with fixed cavitation number $\sigma_0 = \sigma$ to find the corresponding cavity length l_0 .
2. Solve the cavity problem with fixed cavity length l_0 for K iterations (i.e. regridding) and find the converged value of the cavitation number, σ'_0 .
3. Define a new cavitation number, $\sigma_1 = \sigma_0 + (\sigma_0 - \sigma'_0)$.
4. Solve the cavity problem (first iteration) with fixed cavitation number σ_n and find the correct cavity length l_n ($n \geq 1$).
5. Solve the cavity problem with fixed cavity length l_n for K iterations, and find the converged value of the cavitation number, σ'_n ($n \geq 1$).
6. Apply a Newton-Raphson (secant) iterative solution for $\sigma'_n - \sigma = 0$, and find a new cavitation number, σ_{n+1} .

7. Repeat steps 4, 5, and 6 until $\sigma'_n = \sigma$ to within a preset tolerance.

For the results shown in Figure B-6 the last iteration was found for a tolerance of $\frac{\sigma'_n - \sigma}{\sigma} \leq .01$. Convergence to this tolerance took only one Newton-Raphson iteration. Since the nonlinear cavitation number at each cavity length was found by iterating twice ($K = 2$), the total number of regriddings for this case was equal to 4. Included in Figure B-6 is the converged nonlinear cavity (known, since $\sigma = 0.731$ was chosen to correspond to the converged cavity solution with fixed length $l = 0.4$). Also shown in Figure B-6 is the pressure distribution on the foil and cavity from the converged nonlinear solution (plotted with a solid curve). Superimposed on this curve are two pressure distributions which resulted from the fully wetted analysis of the foil and cavity from the first iteration (plotted with asterisks) and the last iteration (plotted with open circles). Note that the pressure distribution on the cavity from the last iteration satisfies the imposed dynamic boundary condition, and even the pressure distribution on the cavity from the first iteration comes very close to satisfying the condition.

B.3 Effect of the detachment point

It was mentioned in Chapter 1 that the point at which the cavity detaches depends on the nature of the viscous boundary layer. Since we don't include viscosity in the present method, the point of detachment is considered as an independent variable in the solution. In this section, the effect of the detachment point will be investigated for two dimensional flows.

Figure B-10 shows the first iteration solution for a partially cavitating NACA16006 foil at $\alpha = 3^\circ$ with several points of detachment for fixed cavitation number $\sigma = 0.7$. Here it is seen that the detachment point has a dramatic effect on the cavity extent, with the cavity length diminishing as the detachment point moves aft.

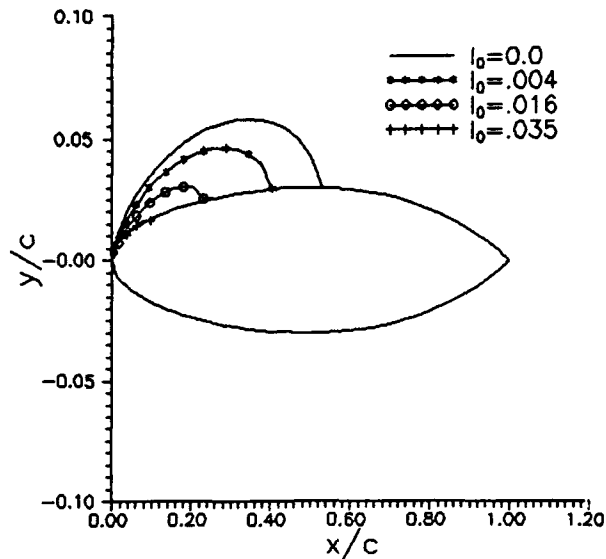


Figure B-10: The effect of detachment point on the partial cavitation solution. Shown are four solutions corresponding to detachment points $\frac{l_0}{c} = 0, .004, .016$ and $.035$. The foil is NACA16006 at $\alpha = 3^\circ$ and $\sigma = 0.7$. The termination model parameter λ is zero.

B.4 Conclusions from 2-D Survey

The following conclusions may be drawn from my survey of the present method for 2-D flows:

1. The nonlinear cavity shapes from the first and converged iterations are very close to one another for a wide range of conditions. This suggests that only a small amount of error is introduced by satisfying the boundary conditions on the approximate flow boundary. The cavity shapes predicted by linear theory with leading edge corrections are also close to the nonlinear shapes for small angles of attack and large thicknesses, but they diverge from the nonlinear shapes as the angle of attack increases and the thickness decreases.
2. Typically the number of panels required for 3-digit convergence of σ is $N = 80$.
3. An additional requirement for convergence with number of panels is the incorporation of an accurate definition of the potential at the leading edge of the cavity, ϕ_0 .

Appendix C

Termination Models

The need for a termination model arises from the inconsistency inherent in forcing a constant-velocity streamline to end at a stagnation point. This need has long been recognized. As mentioned in Chapter 1, excellent reviews of existing models may be found in [75] and [63]. The termination models investigated for this thesis are described in this appendix.

Many termination models are designed first and foremost for mathematical expediency. Accurate modelling of the physics tends to be a secondary priority, mainly because it is impossible to simulate the physical nature of multiphase turbulent flow using a potential flow model. Velocity measurements made behind a partial cavity on a two-dimensional foil in steady flow showed the existence of a rather thick wake trailing the cavity [11]. Measurements on the cavity also showed a slight velocity attenuation near the cavity trailing edge. These experiments suggest that an open wake model may be the most physically realistic termination model.

In this thesis, several models were tried. These fall into two categories:

1. The end-plate model. This model is similar to the Riabouchinsky end-plate model, as applied by Uhlman [69], except that the end-plate is allowed to have curvature. The source strength or, alternatively, the cavity height, near the end of the cavity is specified by an algebraic law.
2. The pressure model. In this model, first suggested by Lemonnier and Rowe [20], the pressure on the cavity is allowed to vary in a region near the end

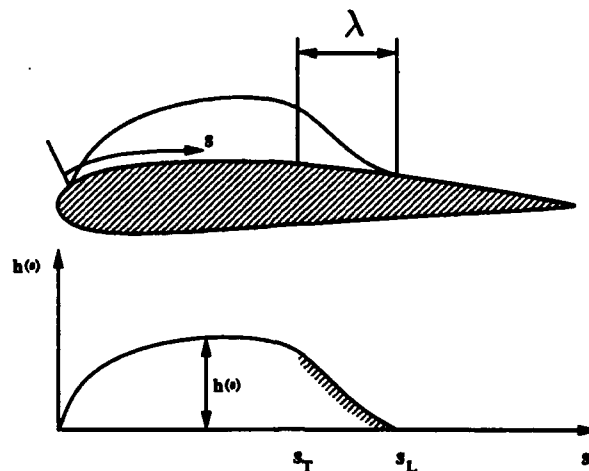


Figure C-1: A depiction of the cavity height law for partial cavitation.

of the cavity from its constant value upstream to some fraction of that value at the cavity trailing edge. This model also allows for the cavity to be open and seems to be a more physically realistic simulation.

At the time these were developed for 2-D flows, the motivation was to find a model which allowed for smooth and quick convergence to the fully nonlinear solution. Some details and results of the investigation will be given in the following sections.

C.1 Partial Cavitation

C.1.1 Cavity Height Law

In this model, the cavity is split into two zones: one zone near the trailing edge of the cavity (called the *transition zone*) with horizontal projected length λ, with the other zone being the upstream remainder (see Figure C-1). Within the transition zone, the source strength is *specified* and given by the algebraic expression

$$\frac{\partial \phi}{\partial n}(s) = \frac{\partial \phi}{\partial n}(s_T) \left[\frac{s_L - s}{s_L - s_T} \right]^\nu \quad s_T \leq s \leq s_L \quad (\text{C.1})$$

Here, s is the arclength of the foil beneath the cavity, measured from the cavity leading edge along the foil surface, s_L is the value of s at the trailing edge of the cavity, and s_T is the value of s at the beginning of the transition zone. The streamwise extent of

the transition zone is defined by the parameter $\lambda = (s_L - s_T)/s_L$. The parameters λ and ν ($\nu > 0$) are arbitrary constants.

An example of a computation made with this termination model is shown in Figure C-2. Shown is the first iteration cavity for a NACA16006 foil at $\alpha = 4^\circ$ with a cavity length of $\frac{l}{c} = 0.4$. The length of the transition zone is $\frac{\lambda}{c} = 0.15$. Although the cavity looks smooth and reasonable, the method suffered from poor convergence to the fully nonlinear cavity (which is why I only show the first iteration). One possible explanation for this is the slope discontinuity of the cavity at $s = s_T$. A slope continuity condition could have been incorporated. However, a natural way to ensure slope continuity is to use a model which governs the cavity pressure rather than the cavity height. The height model was then abandoned in favor of a pressure model, which will be described next.

C.1.2 Pressure Law

The pressure law termination model was developed in order to ensure slope continuity of the cavity surface, as mentioned above. It was also our intention to simulate the real attenuation of pressure which has been measured in steady flow 2-D experiments at MIT [24]. The cavity is again broken into two zones, with a transition zone of length λ (see Figure C-3). The model requires the total velocity on the cavity to satisfy

$$\frac{\partial \Phi}{\partial s} = q_c [1 - f(s)] \quad (\text{C.2})$$

where

$$f(s) = \begin{cases} 0 & \text{if } s < s_T \\ A \left[\frac{s - s_T}{s_L - s_T} \right]^\nu & \text{if } s_T \leq s \leq s_L \end{cases} \quad (\text{C.3})$$

The parameters are defined in section C.1.2, with the exception of A , which is an arbitrary constant between zero and one. A , λ and ν are inputs.

The convergence of the scheme to the fully nonlinear solution, with the pressure law termination model implemented, is excellent. This has already been shown in Chapter 1 and in Appendix B (see, for example, Figure B-1).

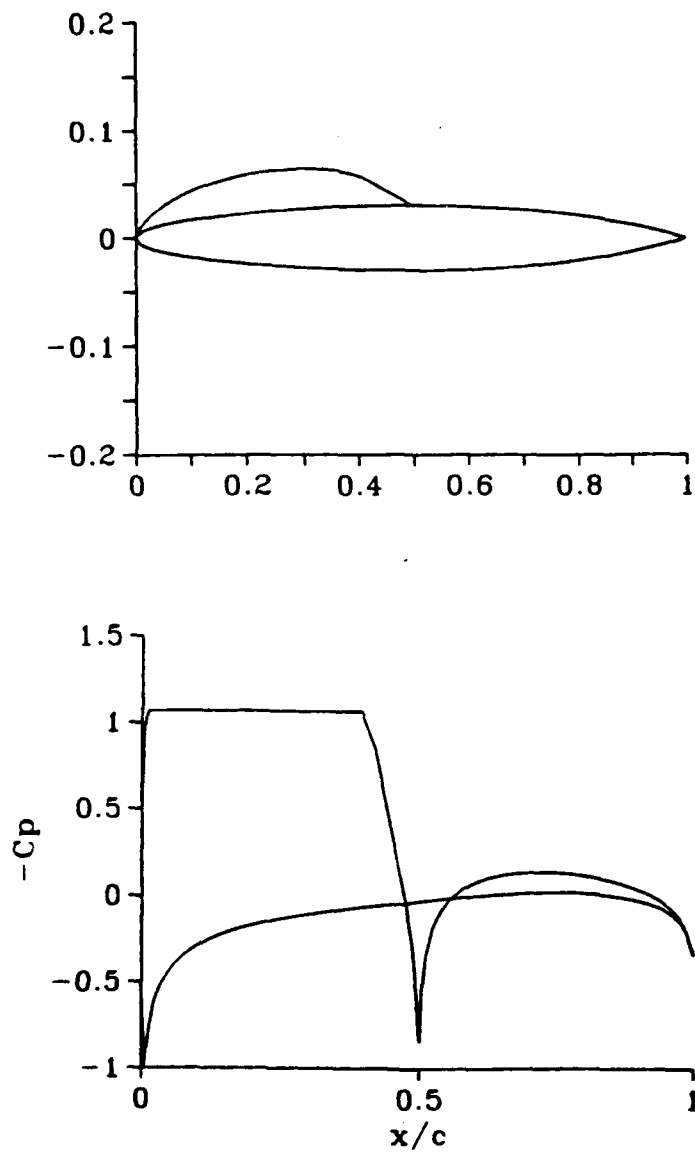


Figure C-2: An example of a partial cavity solution using the height law termination model. Shown are the cavity shape and pressure distribution for a NACA16006 foil at $\alpha = 4^\circ$ with a cavity length of $\frac{l}{c} = 0.4$. The length of the transition zone is $\frac{\lambda}{c} = 0.15$.

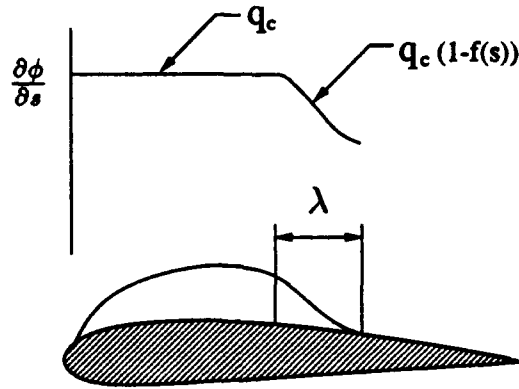


Figure C-3: A depiction of the pressure law for partial cavitation.

Figure C-4 shows the effect of varying the length of the transition zone, λ , on the converged nonlinear cavity shape. Varying λ from .06 to .24, with all other parameters frozen, decreased the volume by 12%. However, for the same perturbation of λ , the cavitation number increased by only 3%. The parameter ν was also varied in a numerical experiment, which showed the dependence to be relatively minor, as is also evident in Figure C-4.

Figure C-5 shows the dependence of the solution on the parameter A . Here, it is seen that the solution depends strongly on A . If A is too large for the given λ , then the cavity surface intersects the foil surface. For $\lambda \sim 0.15$, $A = .5$ usually produces good results.

C.2 Supercavitation

C.2.1 Curved End-Plate Model

Several end plate models were examined in the course of the investigation. First, a modified Riabouchinsky end plate model was tried, similar to the one used by Uhlman [71]. In this model, the end of the cavity is replaced by a vertical flat plate on which the kinematic boundary condition is satisfied. The height of the plate comes out of the solution. While the x location of the plate was fixed, it was unconstrained in the vertical plane. Since there was no closure condition in this model, an additional

λ	ν	σ	V/c^2
.06	.50	0.90113	0.015894
.12	.50	0.91333	0.014948
.24	.50	0.92780	0.013980
.12	.75	0.91027	0.015184
.12	1.00	0.90788	0.015370

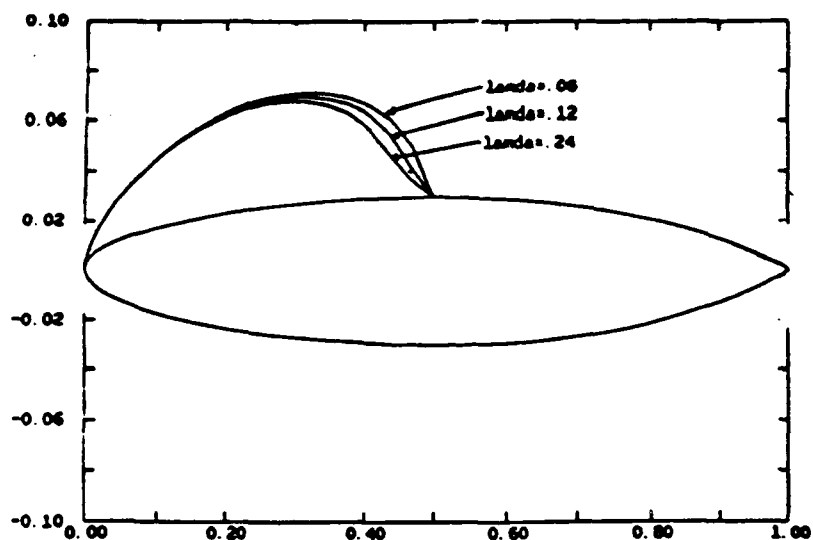


Figure C-4: Cavity shapes, cavitation numbers and cavity volumes for different values of the parameters λ and ν .

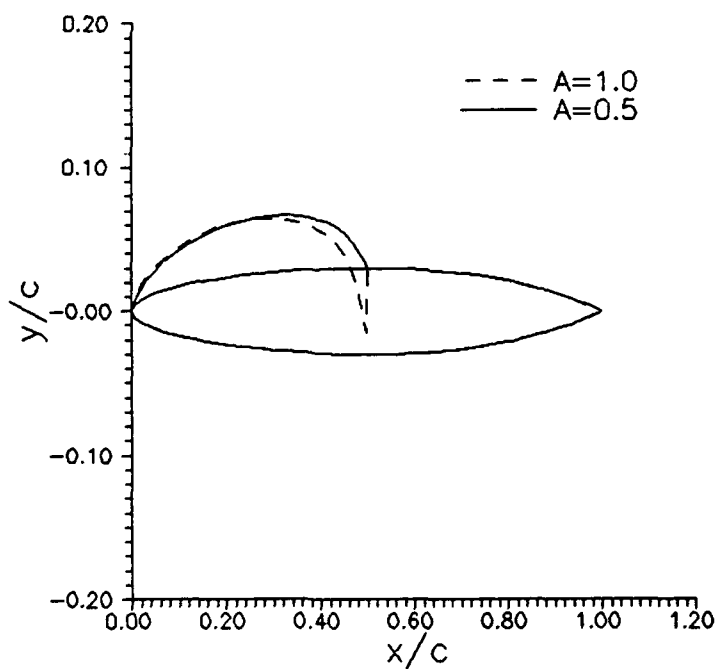


Figure C-5: Cavity shapes for different values of the parameter A . NACA16006 foil with $\alpha = 4^\circ$ and $\frac{l}{c} = 0.5$.

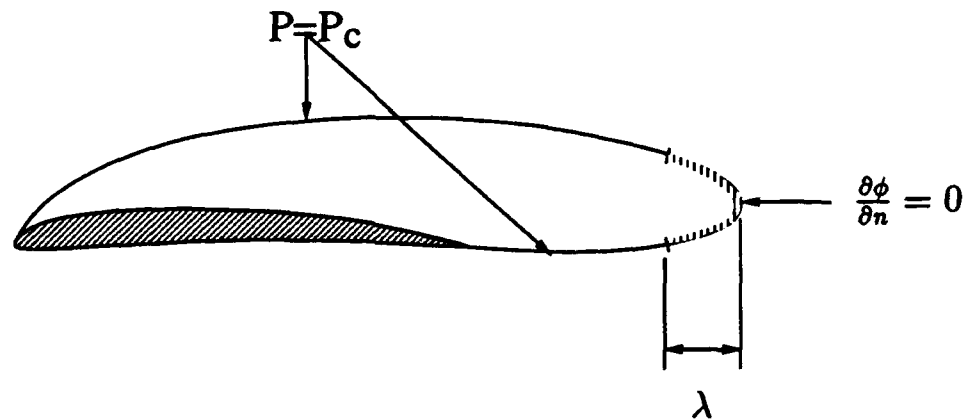


Figure C-6: A sketch of the end-parabola model for supercavitation.

equation was needed to round out the system of equations. For this reason, a matching slope condition was applied at the trailing edge of the foil (matching the pressure side foil slope to the slope of the cavity). Unfortunately, this turned out to be an ill posed problem. The slope matching condition was unnecessary because linear theory, which was used as the first iteration, satisfies a Kutta condition at the foil trailing edge which resulted in continuous slopes. Thus the problem was over-constrained and the resulting cavity shapes were unrealistic. This prompted us to change to a model which used a different kind of end-plate model, one which utilized a form of the cavity closure condition. In this model, the end plate model was allowed to have curvature, and we refer to it as the *curved end plate model*.

The curved end plate model (shown in Figure C-6) is similar to the cavity height model for partial cavitation. This model uses an algebraically defined curved end plate on which the kinematic boundary condition is applied. The end plate has horizontal extent defined by the parameter λ , as shown in Figure C-6. In this case a cavity closure condition is applied which constrains the end plate to move vertically. Specifically, the closure condition requires the upper and lower halves of the end plate to move in unison. In an early version, the curved end plate was simply a parabola which maintained its shape throughout all iterations; it simply moved up or down according to the solution. This model was very successful in obtaining the converged nonlinear solution in relatively few iterations. This model, however, suffered due to

the lack of a requirement that the slope of the cavity be continuous at the juncture of the end parabola and the upstream part of the cavity. The resulting discontinuity in slope was not strong enough to corrupt the iterative convergence; however, it did result in strange looking cavities at high angles of attack. Results for a supercavitating NACA16006 foil are shown in Figure C-7. In this figure, the solution is shown from linear theory and nonlinear theory (using the end parabola model) at two angles of attack (10° and 18°). At the higher angle of attack, the discontinuity is clear.

The next modification was to include matching slope conditions to ensure slope continuity at the cavity-parabola juncture. Rather than apply the conditions as two additional equations, which would have rendered the problem over-constrained, we chose to satisfy the conditions in an iterative sense. The end plate is considered as two curves, an upper curve and a lower curve. The curves are no longer defined as halves of a parabola; instead, they are defined as polynomials which must match points and slopes at either end. The expression for the cavity surface $y(\bar{x})$ is

$$y(\bar{x}) = a\bar{x} + b\sqrt{\lambda - \bar{x}} + c \quad (\text{C.4})$$

where the coefficients a, b, c are found from the conditions

$$\begin{aligned} y(0) &= y_T \\ y'(0) &= y'_T \\ y(\lambda) &= y_L. \end{aligned}$$

y_T and y'_T are the y -position and slope of the cavity at the juncture with the end plate, as shown in Figure C-9. y_L is the y -position at the cavity trailing edge. Notice that equation C.4 forces $y(\bar{x})$ to have infinite slope at $\bar{x} = \lambda$.

At this point, it was also recognized that the extent of the upper and lower curves need not be the same. There are therefore two defining parameters, λ_l and λ_u (see Figure C-8). At the end of every iteration, a new cavity shape is found by integrating the source strength forward from the leading edge on the suction side and from the

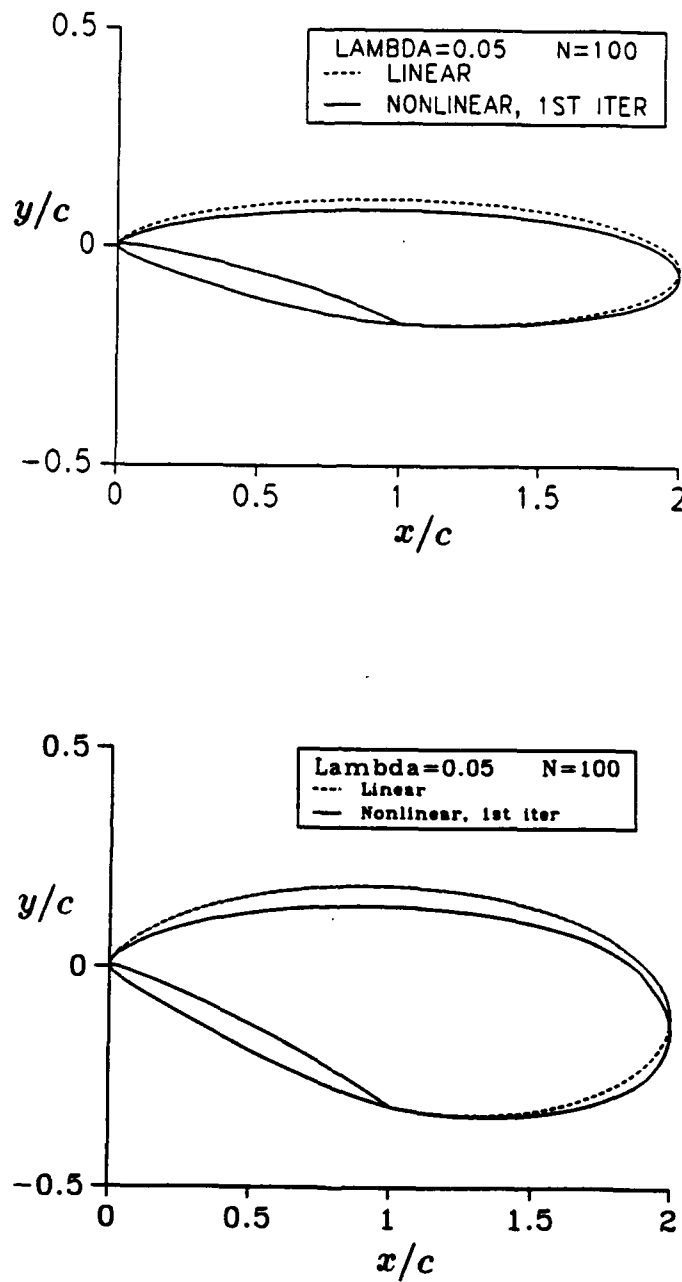


Figure C-7: Results of linear theory and nonlinear theory using the end parabola model. NACA16006 foil at $\alpha = 10^\circ$ and $\alpha = 18^\circ$. The cavity length is $\frac{l}{c} = 2.0$; the cavity detaches at the leading edge. The length of the transition zone is $\lambda = .05$

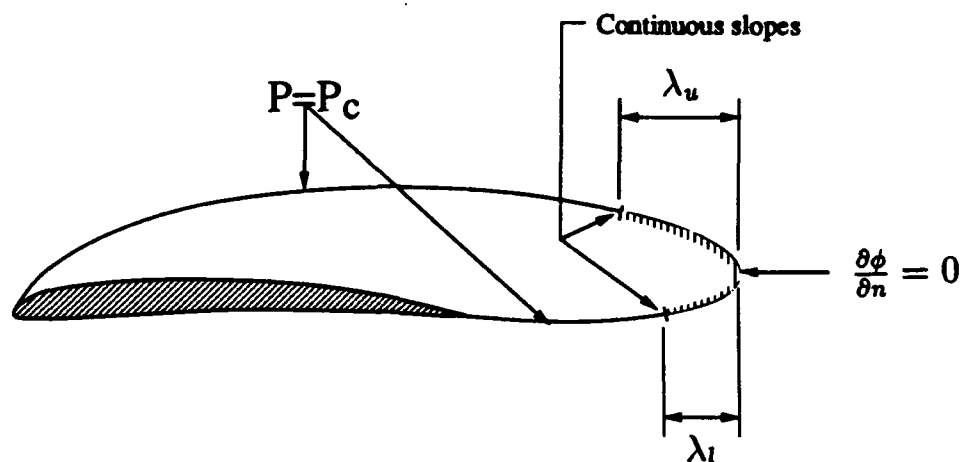


Figure C-8: A sketch of the curved end-plate model for supercavitation.

trailing edge on the pressure side. The shift of the cavity surface is taken along its normal everywhere except in the transition zone, where we allow only the vertical component of the shift. The cavity closure condition requires that the vertical shifts Δ of the upper and lower halves of the end plate be equal (as shown in Figure C-9). In this way, a new cavity shape has been found and is ready for the next iteration. However, at this point we *regenerate* the end plate using equation C.4. In other words, we force the surface to be continuous with the *current* iteration. This is repeated until the nonlinear solution converges.

The curved end plate model is the most robust model I tried (i.e., it allowed smooth convergence at very high angles of attack). In a sense, this model is a more appropriate "Riabouchinsky-analogue" than the flat end plate model, because it allows the upper half of the plate to be longer than the lower half. It turns out that this is necessary in order to obtain smooth (continuous slope) pressure distributions (corresponding to continuous cavity curvature) at the cavity/end-plate juncture. This is shown in Figure C-10, where computations are shown for a flat plate hydrofoil at $\alpha = 30^\circ$ with two choices of λ_l and λ_u . In the first computation, $(\lambda_l, \lambda_u) = (.22, .33)$ and the resulting pressures are shown to overshoot the cavity pressure in the transition zone. In the second computation, $(\lambda_l, \lambda_u) = (.13, .23)$ and the resulting pressures are slope-continuous at the juncture and everywhere greater than the cavity pressure.

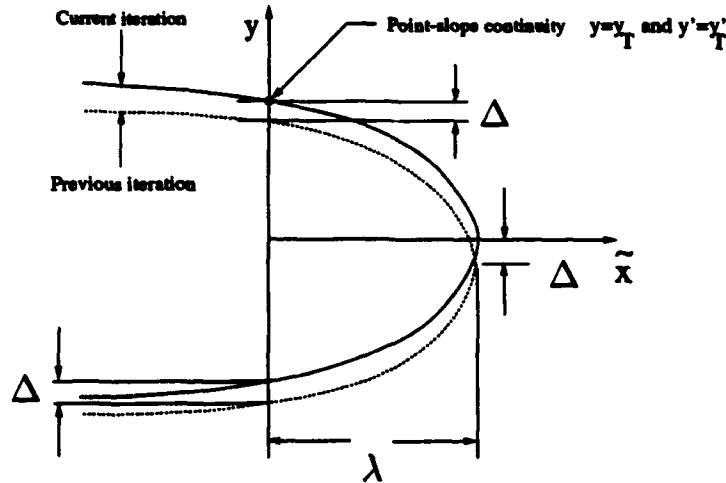


Figure C-9: A blow-up of the transition zone, showing how the cavity is updated between iterations with the curved end plate termination model.

C.2.2 Pressure Law

A pressure model, similar to the one used for partial cavitation, was also implemented for supercavitation. This model is characterized by three parameters, λ_1 , λ_2 and δ^* , as shown in Figure C-11. λ_1 and λ_2 are two adjacent zones (unlike the end plate model, they do not differ from top to bottom). One zone extends upstream a distance λ_1 from the original cavity "trailing edge" (corresponding to the cavity length assumed for the linear solution). The other zone extends downstream a distance λ_2 . The cavity is assumed to be open and the openness is specified to be δ^* . The cavity closure condition is equivalent to the one used for the curved end plate model, requiring that the upper and lower cavity coordinates at the upstream end of the transition zone have the same vertical translation from one iteration to the next. The wake is assumed to be open and the openness extends to downstream infinity.

The effect of the pressure law parameters on the cavitation number, cavity volume and lift and drag coefficients is shown in Table C.1. Notice that the length of the transition zones λ_1, λ_2 have a fairly large effect on σ and V , while the forces are relatively independent of the parameters.

A direct comparison between the curved end plate model and the pressure law

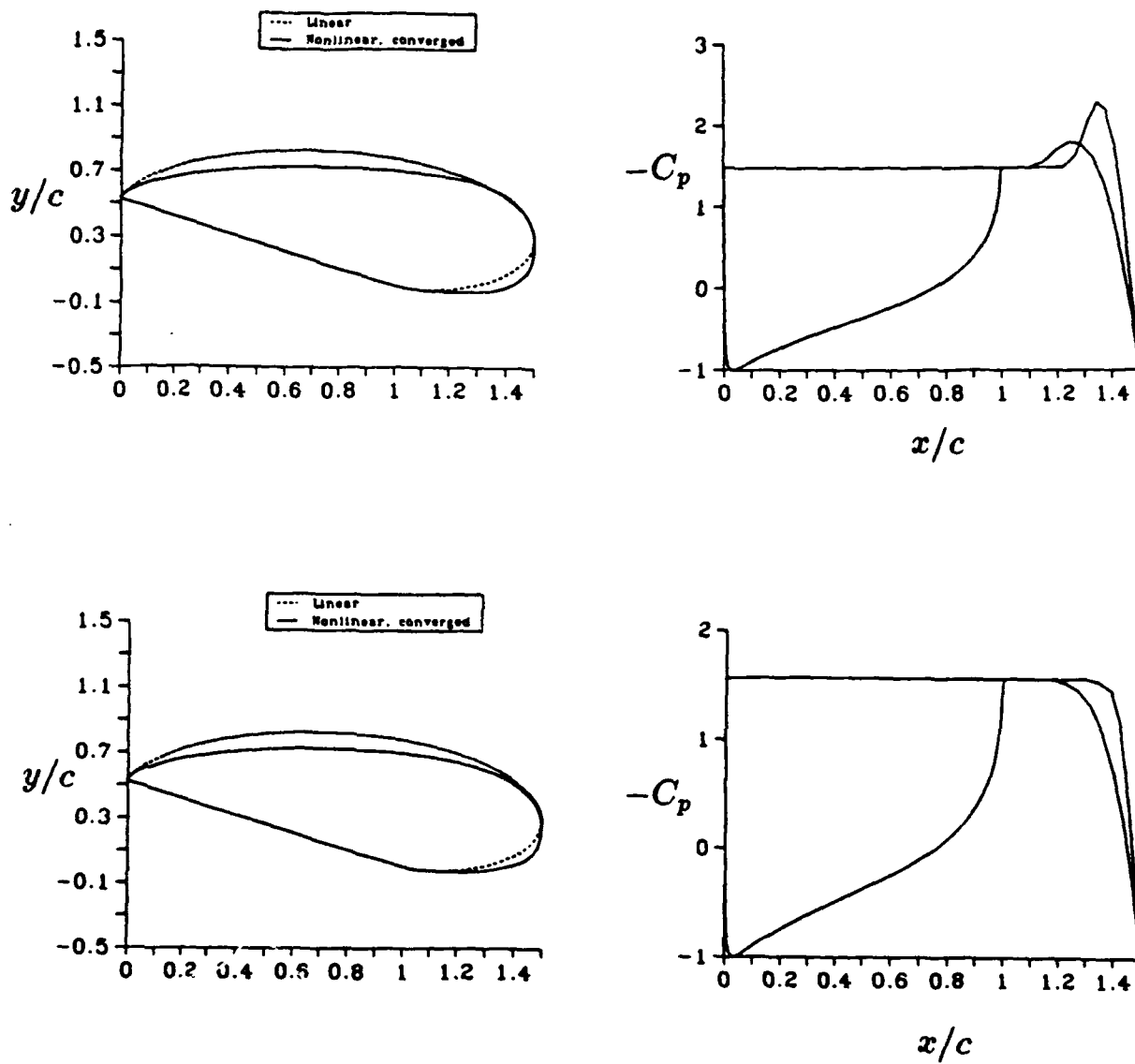


Figure C-10: Cavity shapes (from linear theory and nonlinear theory) and pressure distributions (from nonlinear theory) for a flat plate hydrofoil at $\alpha = 30^\circ$. The slope continuity of the pressure distribution is shown to depend on the parameters λ_l and λ_u .

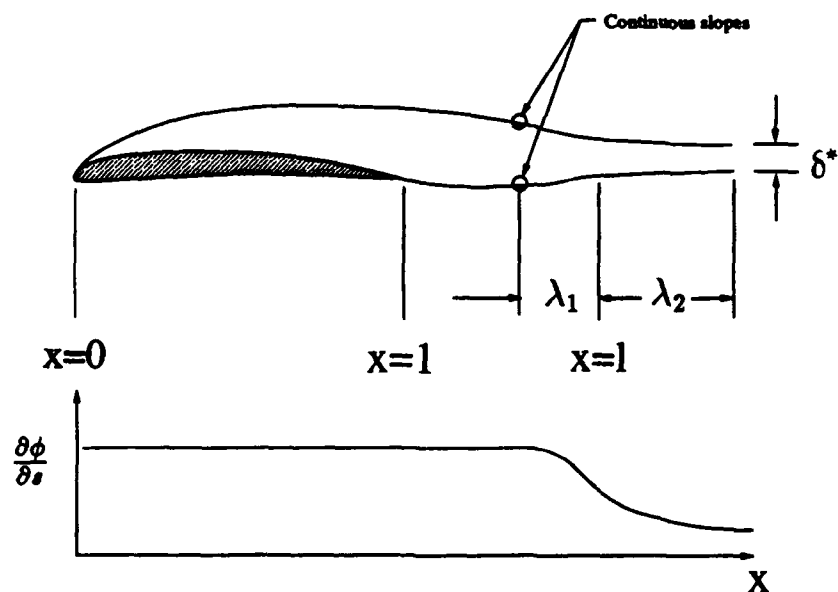
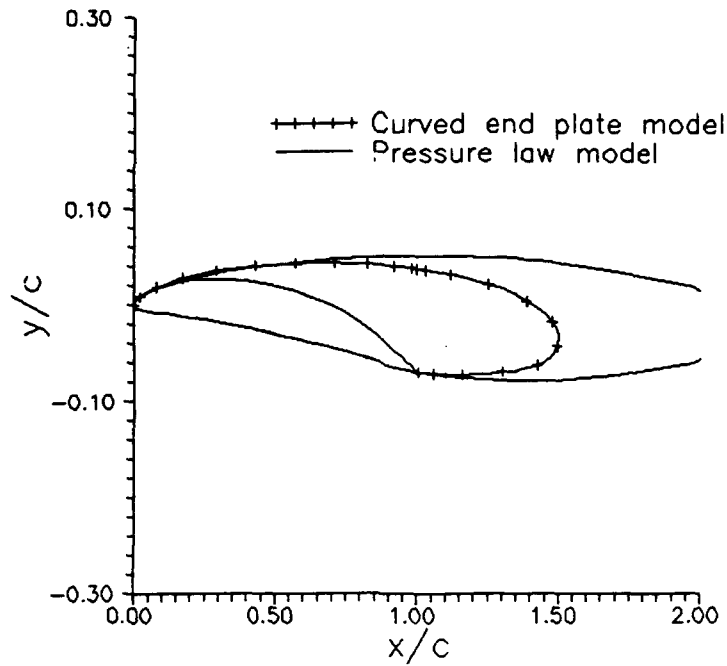


Figure C-11: A depiction of the pressure law for supercavitation.

λ_1	λ_2	δ^*	σ	Volume/ c^2	C_L	C_D
0.1	0.5	0.10	0.104	0.146	0.250	0.022
0.1	0.5	0.07	0.122	0.143	0.246	0.022
0.1	0.3	0.07	0.130	0.133	0.246	0.022
0.2	0.2	0.07	0.138	0.126	0.247	0.022

Table C.1: The effect of parameters on the cavity solution using the pressure law termination model. Computations are for a NACA16005 thickness form with a NACAa.8 camber profile with a maximum camber of .03. $\alpha = 4^\circ$, $\frac{l}{c} = 1.5$, $\frac{l_a}{c} = 0.01$ and $A = 0.1$.



Model	σ	Volume/ c^2	C_L	C_D
Curved End Plate	0.205	0.111	0.230	0.021
Pressure Law	0.130	0.133	0.246	0.022

Table C.2: The difference between the curved end plate model and the pressure law model for the same flow geometry as in the previous table. The pressure law termination model parameters are: $\lambda_1 = 0.1$, $\lambda_2 = 0.3$, $\delta^* = 0.1$, and $A = 0.1$. The end plate termination model parameters are: $\lambda_l = 0.11$ and $\lambda_u = 0.15$.

model is shown in Table C.2 for the same flow configuration treated in Table C.1. Shown also with the table are the computed cavity shapes, showing the difference termination models.